

Evaluation of Structure and Material Properties of RF Magnetron Sputter-Deposited
Yttria-Stabilized Zirconia Thin Films

Jeffrey Robert Piascik

A dissertation submitted to the faculty of the University of North Carolina at Chapel Hill
in partial fulfillment of the requirements for the degree of Doctor of Philosophy in the
Curriculum in Applied and Materials Sciences.

Chapel Hill
2007

Approved by

Advisor: Dr. Jeffrey Thompson

Reader: Dr. Brian Stoner

Reader: Dr. Christopher Bower

Reader: Dr. Nalin Parikh

Reader: Dr. Otto Zhou

ABSTRACT

Jeffrey Robert Piascik: Evaluation of Structure and Material Properties of RF Magnetron Sputter-Deposited Yttria-Stabilized Zirconia Thin Films
(Under the direction of Dr. Jeffrey Y. Thompson and Dr. Brian R. Stoner)

Over the past several decades, research has focused on utilizing ceramic materials in new technological applications. Their uses have been primarily in applications that involve high temperatures or corrosive environments. Unfortunately, ceramic materials have been limited especially since they can be brittle, failing in a sudden and catastrophic manner. A strong emphasis on understanding mechanical properties of ceramics and ways to improving their strength and toughness, has led to many new technologies.

The present work is part of a larger research initiative that is aimed at using RF magnetron sputter deposition of yttria-stabilized zirconia to improve the fracture toughness of brittle substrates (more specifically dental ceramics). Partially-stabilized zirconia (PSZ) has been studied extensively, due to its high temperature stability and stress-induced tetragonal to monoclinic ($T \Rightarrow M$) martensitic phase transformation. RF magnetron sputtering was chosen as the deposition method because of its versatility, especially the ability to deposit oxides at low temperatures.

Initial investigations focused on the development of process-structure-properties of YSZ sputtered deposited thin films. The YSZ thin films were deposited over a range of temperatures (22 - 300°C), pressures (5 – 25 mTorr), and gas compositions (Ar:O₂ ratio). Initial studies characterized a select set of properties in relation to deposition

parameters including: refractive index, structure, and film stress. X-ray Diffraction (XRD) showed that the films are comprised of mainly monoclinic and tetragonal crystal phases. The film refractive index determined by prism coupling, depends strongly on deposition conditions and ranged from 1.959 to 2.223. Wafer bow measurements indicate that the sputtered YSZ films can have initial stress ranging from 86 MPa tensile to 192 MPa compressive, depending on the deposition parameters. Exposure to ambient conditions (25°C, 75 % relative humidity) led to large increase (~ 100 MPa) in the compressive stress of the films. Environmental aging suggests the change in compressive stress was related to water vapor absorption. These effects were then evaluated for films formed under different deposition parameters with varying density (calculated packing density) and crystal structure (XRD).

Based on the above results, it was determined to evaluate stress as a function of substrate bias. It was shown that increasing substrate bias power disrupted columnar grain growth and reduced the percent change in compressive stress when exposed to ambient environments. TEM confirmed a reduction in inter-granular porosity for substrate bias depositions, but an increase in lateral defects. It was hypothesized that substrate bias would increase the film's density, but after inspection of SEM and TEM micrographs, it appeared that as bias was increased the density decreased.

This T \Rightarrow M phase transformation has been well documented for bulk PSZ, but limited data exists for PSZ thin films. Data is presented that supports a stress-induced T \Rightarrow M transformation mechanism that occurs during sputter-deposition in the presence of a substrate bias. Substrate bias (0 – 50W) was originally applied to increase film density, modify microstructure, and vary film stress. The films were deposited using rf

magnetron sputtering from a sintered yttria-stabilized zirconia (YSZ) target and subsequently characterized using scanning (SEM) and transmission electron microscopy (TEM), x-ray diffraction (XRD), and wafer bow measurement (for stress analysis). With no substrate bias the films exhibited a columnar grain structure consistent with sputter-deposited films, with a majority tetragonal phase as determined by XRD. Under higher substrate bias, wafer bow measurements indicated a steady increase in compressive stress as substrate bias increased (max. 310MPa at 50W bias), while XRD indicated a corresponding increase in the percentage of monoclinic phase. Both SEM and TEM analyses revealed a shift from a defect-free columnar structure to one consisting of lateral intra-columnar or trans-granular defects for films deposited under substrate bias conditions. It is believed that these defects form as a result of stress-relief in the growing film via the transformation from tetragonal to monoclinic phase due to bias-induced compressive stress. FEA modeling is used to confirm stress contours and defect generation within the films.

The structure developed under substrate bias deposition is hypothesized to provide beneficial strengthening mechanisms, similar to microcrack toughening, when deposited on brittle substrates. This manuscript concludes with an analysis of YSZ thin films deposited on an alternative substrate (soda-lime glass) that replicates a bio-inert material.

ACKNOWLEDGEMENTS

The long journey finally reaches an end... During this time I have been fortunate enough to meet a lot of great people who have in some way or another lent a hand in this endeavor. I would first like to express my appreciation to all the people at RTI who have been absolutely great in helping me in any way needed. From sputtering to SEM analysis to literature searches, I always had someone to lean on. To all my committee members who have taken time-out of their schedules to make themselves available. To Chris Bower for all the discussions on the whiteboard and for the occasional fly-fishing stories that kept me sane. This of course would not have been possible if not for the opportunity given to me by Jeff Thompson and Brian Stoner. I cannot express the gratitude I have for helping me through this – both have been extremely patient and have made me a better researcher.

Next I would like to thank all my friends for everything – I have truly been blessed with wonderful friends. To my family, especially my parents who not only taught me not quit, but if you put your mind to it - anything is possible. I truly have great admiration for what both have achieved and I could not have done this without their help and guidance. And I would be remiss if I did not thank Anne, she unfortunately took the brunt of my mood-swings, constant working, and scientific dribble. Thank you all! Time to go fishin'

TABLE OF CONTENTS

ABSTRACT.....	ii
LIST OF TABLES.....	ix
LIST OF FIGURES.....	x
LIST OF ABBREVIATIONS.....	xv
LIST OF SYMBOL.....	xvi

Chapter	Page
1. Introduction	1
1.1 Statement of Purpose.....	4
1.2 References.....	6
2. Literature Review and Fundamentals.....	7
2.1 Sputter Deposition.....	7
2.2 Stress in Sputter Deposited Thin Film.....	14
2.2.1 Thermal Stresses.....	15
2.2.2 Intrinsic Stresses.....	16
2.3 Zirconia as a Material.....	19
2.3.1 Phase Stabilization.....	21
2.3.2 Phase Transformation ($T \Rightarrow M$).....	21
2.3.3 Deposition of Zirconia.....	23
2.4 References.....	27
3. Experimental Procedures.....	31
3.1 Substrate Materials.....	31
3.2 Sputter Deposition Equipment/Parameters.....	32
3.2.1 Deposition System.....	32

3.2.2	Power.....	34
3.2.3	Substrate Bias.....	34
3.2.4	Deposition Pressure (working).....	35
3.2.5	Substrate Temperature.....	35
3.2.6	Oxygen (sputtering gas).....	36
3.2.7	Sputtering Target.....	36
3.3	Physical Characterization.....	37
3.3.1	Wafer Bow Measurement (WBM).....	38
3.3.2	X-Ray Diffraction (XRD).....	38
3.3.3	Prism Coupler.....	39
3.3.4	Scanning Electron Microscopy (SEM).....	40
3.3.5	Transmission Electron Microscopy (TEM).....	41
3.3.6	Finite Element Analysis (FEA).....	42
3.4	Experimental Summary.....	43
3.5	References.....	44
4.	Processing-Structure-Property Relationships: Sputter-deposited 3mol% YSZ Thin Films.....	46
4.1	Deposition of YSZ Thin Films.....	47
4.2	Physical Characterization.....	48
4.2.1	Film Stress.....	48
4.2.2	Structural Analysis.....	55
4.2.3	Crystal Structure Analysis.....	66
4.2.4	Index of Refraction.....	69
4.3	Summary – Process-Structure-Properties.....	71
4.4	References.....	74
5.	Stress Evolution as a Function of Substrate Bias.....	76
5.1	Deposition of YSZ Thin Films	77
5.2	Physical Characterization.....	79
5.2.1	Film Stress.....	79
4.2.2	Structural Characterization.....	81
5.3	Summary – Substrate Bias Deposition.....	88

5.4 References.....	90
6. Stress-induce Phase Transformation in YSZ Thin Films.....	91
6.1 Deposition of YSZ Thin Films.....	93
6.2 Physical Characterization.....	93
6.2.1 Crystal Structure Analysis.....	93
6.2.2 Structural Analysis.....	95
6.2.3 Finite Element Analysis (FEA).....	103
6.3 Summary – TEM and FEA Modeling of Phase Transformation.....	111
6.4 References.....	113
7. Deposition of YSZ Thin Films on Soda-lime Glass Wafers.....	115
7.1 Deposition of YSZ Thin Films.....	116
7.2 Physical Characterization.....	116
7.2.1 Crystal Structure Analysis.....	116
7.2.2 Film Stress.....	117
7.2.3 Film Structure.....	119
7.3 Summary – YSZ Depositions on Soda-lime Glass.....	119
7.4 References.....	124
8. Conclusion	125
8.1 Suggested Future Work.....	127
8.2 References.....	130
Bibliography.....	131

LIST OF TABLES

Table 3.1	Specific material properties for substrates used in this study	32
Table 4.1:	Wafer bow measurements and calculated film stress for the deposition parameter space: (-) designates compressive stress. Calculated values for intrinsic stresses and volume % monoclinic are also shown	50
Table 4.2:	Index of refraction measurements for parameter space (measurements taken upon removal from vacuum chamber and 720 hr after aging in ambient environments). Color designates optical appearance of each film	71
Table 5.1:	Absolute stress values at post deposition times of 0 and 30 days	80
Table 7.1:	Reported film stress values, calculated intrinsic stress, and volume percentage of monoclinic phase for deposited YSZ thin films	117

LIST OF FIGURES

Figure 1.1:	Brittle materials contain various types of strength controlling flaws	2
Figure 2.1:	Representation of sputtering technique. The impact of an atom or ion on a surface produces sputtering from the surface as a result of the momentum transfer from the in-coming particle	9
Figure 2.2:	Representation of the influence of substrate temperature and argon pressure on the microstructure of sputter-deposited thin films	11
Figure 2.3:	Diagram describing (a) residual tensile stress and (b) residual compressive stress in thin films	15
Figure 2.4:	Schematic representation of thermal and intrinsic stress contributions	17
Figure 2.5:	Process of “ion-peening”: (a) an ion approaches the surface of a film with in-grown voids, (b) the ion impacts the film, transferring energy to the film atoms, (c) causing atoms to rearrange, filling in part of the defect, resulting in a denser film	18
Figure 2.6:	Representation of the process responsible for producing compressive stresses and entrapped working gas in sputter-deposited thin films	19
Figure 2.7:	ZrO ₂ rich sections of the phase diagrams for ZrO ₂ -Y ₂ O ₃	20
Figure 2.8:	Representation of stress-induce phase transformation (T⇒M) toughening process. The energy of the advancing crack is dissipated in phase transformation and in overcoming the matrix constraint by transforming grains	22
Figure 3.1:	Representative schematic of sputter deposition system	33
Figure 3.2	X-Ray diffraction pattern of sputter deposited 8mol% yttria-stabilized zirconia thin film	37
Figure 4.1:	Process cube describing deposition parameters (function of substrate temperature, working pressure, and background oxygen). Center of process cube was performed three separate depositions	48

Figure 4.2:	Contour plots of the relationship of film stress and deposition parameters	52
Figure 4.3:	Calculated stress measurement for YSZ film deposited without an applied bias	53
Figure 4.4:	Percent change in measured stress values as a function of several thermal treatments. Stress was measured at set time intervals immediately after deposition and thermal treatments (12 hr / 100° C / 5×10^{-6} torr)	53
Figure 4.5:	Calculated stress measurements for first 2hr of exposure to ambient conditions (25°C, 75% relative humidity)	54
Figure 4.6:	SEM micrographs for YSZ thin film with deposition parameters: working pressure - 5mT, substrate temperature 300°C, and only Argon sputtering gas	57
Figure 4.7:	SEM micrographs for YSZ thin film with deposition parameters: working pressure - 15mT, substrate temperature 150°C, and Ar:O ₂ ratio of 15:1	58
Figure 4.8:	SEM micrographs for YSZ thin film with deposition parameters: working pressure - 25mT, substrate temperature 300°C, and Ar:O ₂ ratio of 30:1	59
Figure 4.9:	SEM micrographs for YSZ thin film with deposition parameters: working pressure - 25mT, substrate temperature 25°C, and Ar:O ₂ ratio of 30:1	60
Figure 4.10:	SEM micrographs for YSZ thin film with deposition parameters: working pressure - 5mT, substrate temperature 150°C, and Ar:O ₂ ratio of 15:1	61
Figure 4.11:	SEM micrographs for YSZ thin film with deposition parameters: working pressure - 15mT, substrate temperature 150°C, and only Argon sputtering gas	62
Figure 4.12:	SEM micrographs for YSZ thin film with deposition parameters: working pressure - 25mT, substrate temperature 150°C, and Ar:O ₂ ratio of 15:1	63
Figure 4.13:	SEM micrographs for YSZ thin film with deposition parameters: working pressure - 15mT, substrate temperature 25°C, and only Argon sputtering gas	64

Figure 4.14:	SEM micrographs for YSZ thin film with deposition parameters: working pressure - 5mT, substrate temperature 300°C, and Ar:O ₂ ratio of 15:1	65
Figure 4.15:	Effect of deposition parameters on the percentage of monoclinic phase formed. Depositions with no oxygen produced films ~100% tetragonal phase as oxygen flow increases, monoclinic phase becomes more prevalent with higher percentages produced at low working pressures	66
Figure 4.16:	Representative XRD scans for YSZ thin films displaying a predominant <111> texture (deposition parameters are noted on the graph)	68
Figure 4.17:	Representative XRD scans for YSZ thin films displaying a predominant <200> texture (deposition parameters are noted on the graph).....	68
Figure 4.18:	Packing density calculation (utilizing measured index of refraction)	70
Figure 5.1:	Representation of water vapor absorption into inter-columnar porosity of deposited YSZ thin films. Resulting interactions (dipole-dipole) induce compressive film stress	78
Figure 5.2:	Compressive film stress measured for varying substrate bias YSZ films upon removal from vacuum and post 30 days exposure to ambient conditions	81
Figure 5.3:	Percentage change in measured film stress for a series of films deposited with differing substrate bias power levels. Stress was measured incrementally for the first 2hr of exposure to an ambient environment upon removal from vacuum	82
Figure 5.4:	Representative SEM micrographs of YSZ sputter-deposited thin films: a). film deposited without substrate bias and b). film deposited with 50W power substrate bias	82
Figure 5.5:	Representative cross-sectional TEM micrographs of YSZ sputter-deposited thin films: (a). film deposited without substrate bias exhibits columnar grain structure with inter-columnar porosity (arrows indicate inter-columnar porosity)	84

Figure 5.5: (cont.)	Representative cross-sectional TEM micrographs of YSZ sputter-deposited thin films: (b) . film deposited with a 25W power substrate bias exhibits columnar grain structure with inter-columnar porosity and presence of lateral defects (arrows indicate inter-columnar porosity and lateral defects).....	85
Figure 5.5 (cont.)	Representative cross-sectional TEM micrographs of YSZ sputter-deposited thin films: (c) . film deposited with 50W power substrate bias shows signs of equiaxed grain structure with limited inter-columnar porosity (arrows indicate lateral defects) ...	86
Figure 5.6:	Volume % monoclinic phase versus differing bias powers. Graph represents an increase in monoclinic as bias power increases	87
Figure 6.1:	Graph displays the relative amount of monoclinic phase present for YSZ films deposited at 0W, 25W, and 50W substrate bias	94
Figure 6.2:	XRD patterns for non-bias, 25W, and 50W bias sputtered films showing a decrease in tetragonal phase and increase in monoclinic phase with increased bias power	95
Figure 6.3:	Representative SEM images for films deposited (a) without substrate bias and (b) with substrate bias of 50W	96
Figure 6.4:	Schematic drawing of a constrained T-YSZ cylindrical grain transforming in the presence of an applied film stress: (a) shows constrained columnar grains under an applied stress and subsequent transformed grain at a 9° shift, (b) depicts the transformed grain with lateral defects (or microcracks), and (c) is a low magnification TEM image showing a columnar grain structure from a bias-assisted YSZ sputter deposited film	98
Figure 6.5:	(a) . Low magnification of 50W substrate bias deposited YSZ thin film. (b) . High resolution TEM of boxed area shown in (a). FFT diffractograms confirm T⇒M transformation area	99
Figure 6.6:	(a) . Low magnification TEM of 50w substrate bias YSZ film showing lower portion of the cross-sectional wedge - interface between film and substrate. (b) . High resolution TEM of transformation area	101
Figure 6.7:	(a) . Low magnification of 50W substrate bias deposited YSZ thin film. (b) . High resolution TEM of boxed area shown in (a). FFT diffractograms confirm M transformation area around the edges of large u-shaped defect	102

Figure 6.8:	Representation of the 3-D model using in evaluating stress in columnar grains	105
Figure 6.9:	FEA analysis of 300 MPa film stress (Von Mises) on columnar grain	106
Figure 6.10:	Plot representing increase in film stress versus thickness. Stress reaches a threshold (σ_T) designating phase transformation, spikes upward, and then relaxes	107
Figure 6.11:	(a). Representation of volumetric change due to Poisson's effect (where V_o is the original volume and V_I is the post transformation volume). (b). Dimensions of u-shaped defect bound by transformation events	108
Figure 6.12:	Schematic of defect generation as a function of intrinsic stress and transformation events	109
Figure 6.13:	Representation of XY shear stress within a columnar grain subjected to a 300 MPa uniform bi-axial stress	111
Figure 7.1:	Representative XRD patterns for varying substrate bias YSZ deposited thin films on soda-lime glass wafers	118
Figure 7.2:	Representative SEM of film deposited without substrate bias on soda-lime glass wafer (Deposition conditions 350W, 150°C, and 30:1 Ar:O ₂)	120
Figure 7.3:	Representative SEM of 50W substrate bias film deposited on soda-lime glass wafer (Deposition conditions 350W, 150°C, and 30:1 Ar:O ₂)	121
Figure 7.4:	Representative SEM of 75W substrate bias film deposited on soda-lime glass wafer (Deposition conditions 350W, 150°C, and 30:1 Ar:O ₂)	122
Figure 7.5:	Representative SEM of 100W substrate bias film deposited on soda-lime glass wafer (Deposition conditions 350W, 150°C, and 30:1 Ar:O ₂)	123

LIST OF ABBREVIATIONS

EDS	Energy Dispersive X-Ray Spectroscopy
FFT	Fast Fourier Transform
FEA	Finite Element Analysis
FE-SEM	Field Emission Scanning Electron Microscopy
FIB	Focused Ion Beam
GIF	Gatan Energy Filter
HIP	Hot-Isostatically Pressed
<i>m</i> -ZrO ₂	Monoclinic Zirconia
PSZ	Partially Stabilized Zirconia
PID	Proportional, Integral, Derivative (loop temperature controls)
PVD	Plasma Vapor Deposition
RF	Radio Frequency
SEM	Scanning Electron Microscopy
T⇒M	Tetragonal-to-Monoclinic Phase Transformation
TEM	Transmission Electron Microscopy
<i>t</i> -ZrO ₂	Tetragonal Zirconia
WBM	Wafer Bow Measurement
XRD	X-Ray Diffraction
YSZ	Yttria Stabilized Zirconia
ZrO ₂	Zirconia

LIST OF SYMBOLS

α	Coefficient of Thermal Expansion
$^{\circ}\text{C}$	Celsius
d_{hkl}	Spacing between the hkl plane of the crystalline phase
E	Elastic modulus
ΔF	Change in Free Energy
$I_{\text{M}(111)}$	Integrated intensities of the (111) monoclinic peak
$I_{\text{T}(111)}$	Integrated intensities of the (111) tetragonal peak
P_t	Transition pressure
R_a	Average Roughness
σ	Stress
ν	Poisson's Ratio
T	Temperature
T_M	Melting Temperature
V_m	Volume monoclinic phase

Chapter 1

Introduction

Over the past several decades, research has focused on utilizing ceramic materials in new technological applications. Their uses have been primarily in applications that involve high temperatures or corrosive environments. Unfortunately, ceramic materials have been limited especially since they can be brittle, failing in a sudden and catastrophic manner. A strong emphasis on understanding mechanical properties of ceramics and ways to improving their strength and toughness, has led to many new technologies [1].

Ceramics, whether crystalline or non-crystalline, typically fail under mechanical loading from structural defects. These defects include internal porosity, inclusions, and surface flaws (or cracks) (Figure 1.1). These act as crack nucleation sites and once a crack begins to propagate, there are no energy absorbing mechanisms to help prevent further propagation. There are two classifications of brittle fracture in polycrystalline materials: (1) trans-granular fracture and (2) inter-granular fracture [2]. In trans-granular fracture, the crack travels through individual grains (or crystals) of the material. The crack may change directions from grain to grain, depending on differing lattice orientations of atoms in each grain. This mode of fracture only occurs in crystalline or partially crystalline ceramics. Inter-granular fracture describes a crack that travels along the grain boundaries and not through the actual grains. This is typical of a material when the phase located in the grain boundaries is weak and brittle [1-2]. Ceramics with low

crystalline volume fractions (glass-ceramics, porcelains) or completely amorphous structures (glasses) are characterized by this mode of fracture.

For brittle materials, cracks are generally assumed to form by the cleavage of atomic bonds in highly stressed regions. These stresses may be due to stress concentrations or residual stress and they will be particularly effective in producing cracks if weak interfaces are present. It has been stated that the presence of high stresses is associated with the heterogeneous nature of the material at the microstructural level or inelastic deformation at localized contacts. It is known that cracks can form at contact events, voids produced during processing, and stresses formed due to temperature changes. It is extremely useful to identify sources of high stress within the microstructure. Areas of microstructural misfits or phase transformations can lead to local regions of stress, which in turn lead to crack formation. Once a crack nucleates, it may undergo further growth, especially if there is a localized stress field associated with the nucleation process or if the growth is impeded by microstructural obstacles. In

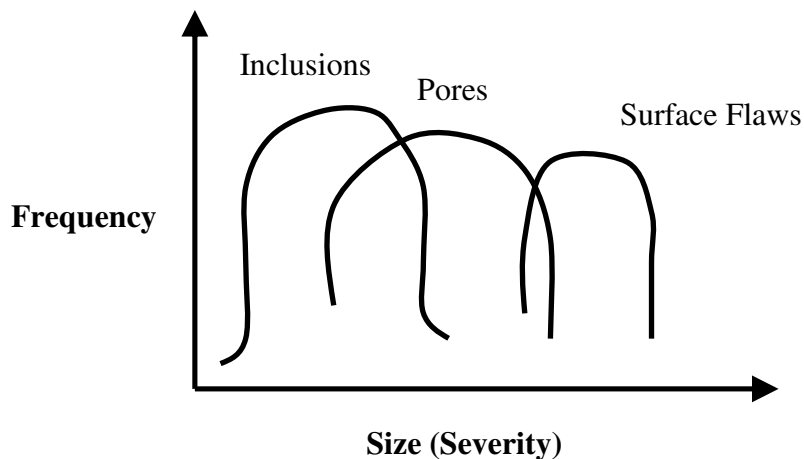


Figure 1.1: Brittle materials contain various types of strength controlling flaws [1].

addition to having a variety of flaw populations that compete for crack initiation, the size of cracks within a population will form a distribution. Therefore, the fracture stress of brittle materials is considered a distribution rather than a finite value. Several types of flaws can compete simultaneously making failure sources quite complex. This is why failure has led to empirical statistical approaches in describing strength distributions [1].

Several techniques have been developed to decrease the likelihood of brittle failure in ceramics ranging from annealing (removal of internal stresses and stress gradients, or development of surface compression) to applying surface coatings [1]. One such technique to applying a surface coating is to sputter a thin film on the surface of the material. The modifying film can potentially passivate surface flaws, generate compressive surface stresses, or act as an energy absorbing layer. Depending on the composition and thickness, the thin film can provide a beneficial strengthening mechanism.

One particular study showed a strengthening of up to 45% of borosilicate glass by sputter depositing thin films of alumina and silicon carbide [3]. Another study investigated the strengthening effects of sputtered gold, aluminum, and aluminum-nitride thin films on dental porcelain [4]. It was determined that the metal films yielded a significant increase in flexural strength, but the aluminum-nitride film had no effect. One material of interest for generating a strengthening thin film is partially-stabilized zirconia (PSZ). Ruddell *et al.* hypothesized that utilizing the transformation toughening effect within yttria-stabilized zirconia (YSZ) would provide improvement in the mechanical properties of a substrate. This transformation effect was not seen primarily due to the columnar grain morphology [5]. It has been reported that for transformation

toughening to occur, the material must be several grains thick [6]. YSZ did show an improvement in fracture strength in the modified substrates. These strengthening mechanisms of the deposited films have been attributed to either bridging the flaws or blunting the flaws, thereby decreasing their sharpness and susceptibility of crack propagation, or generation of surface compressive stresses.

1.1 Statement of Purpose

The present work is part of a larger research initiative that is aimed at using RF magnetron sputter deposition of yttria-stabilized zirconia to improve the fracture toughness of brittle substrates (more specifically dental ceramics). Thompson *et al.* reported that dental restorations typically fail due to critical flaws on the surface that is cemented to the tooth and placed under tension during function. These surface flaws, generated from manufacturing or handling preparation, are the primary reason of failure. A proposed method to eliminate or passivate such flaws is to apply a thin film on the surface. Teixeira *et al.* investigated the strengthening of dental porcelain as a function of YSZ thin film thickness. The results showed that the strength of porcelain significantly increased with deposition of a 3 μ m YSZ coating. A non-linear relationship was observed between film thickness and strength. It was presumed that strengthening is due to modification of surface flaws and/or surface residual stress by the applied thin film [7].

Mechanistically, several hypothesizes of strengthening have been addressed, but other important parameters also need to be considered. Other parameters to consider when fabricating an ideal thin film include; grain structure, film stress, crystal structure, adhesion to the substrate, and optical properties (for certain applications). Film stress

becomes important when discussing what type of stress is desired to provide optimum strength. Whether it is tensile or compressive, its effects on the substrate need to be evaluated and understood. When investigating phase transformation and subsequent strengthening affects, it is important to deposit specific crystal structures in varying percentages. Optical properties are dictated by end application, for dental esthetics, a clear, transparent coating would be beneficial.

The purpose of this manuscript is to develop a process-structure-property relationship of sputter-deposited 3mol% YSZ thin films. To utilize this material as a strengthening layer for brittle substrates, YSZ thin film material properties must be evaluated and tailored to obtain optimal strengthening. Other significant properties, such as exposure to ambient environments, are investigated to thoroughly understand any detrimental effects that could cause film degradation. Unlike bulk YSZ, the thin film counterpart differs structurally, thus it has differing mechanical properties. As opposed to micron sized grains, deposited films display nanometer sized grains. The uniqueness of YSZ is the diffusionless phase transformation from tetragonal to monoclinic phase. Currently, research has focused on the transformation in bulk and not within a thin film construct. One focus of this work is to investigate possible phase transformation within the nanometer grain sized film and subsequent effects on film properties. The mechanics of deformation are not well understood in nanometer sized polycrystalline materials. By creating specific film structures and understanding film properties, it should be possible to create a thin film that will be able to maximize the strength, toughness, and fatigue resistance of brittle substrates.

1.2 References

1. Green D.J, *An Introduction to the Mechanical Properties of Ceramics*, (Cambridge University Press, London, 1998).
2. Askland, D.R., *The Science and Engineering of Materials*, (PWS-Kent, Boston, MA, 1984).
3. Hoshide T., Nebu A., and Hayashi K., “Bending Strength of Borosilicate Glass Coated With Alumina and Silicon Carbide by RF Magnetron Sputtering”, *JSME International Journal Series , A* **41**, 332-337 (1998).
4. Ruddell D.E., Thompson J.Y., and Stoner B.R., “Mechanical properties of dental ceramic coated by RF magnetron sputtering”, *J. Biomed. Mater. Res.*, **51**, 316-320 (1999).
5. Ruddell D.E., Stoner B.R., and Thompson J.Y., “The effect of deposition parameters on the properties of yttria-stabilized zirconia thin films”, *Thin Solid Films* **445**, 14-19 (2003).
6. Butler E.P., “Transformation-toughened zirconia ceramics”, *Mater. Sci. Technol*, **1**, 417-431 (1985).
7. Teixeira E.C.N, Piascik J.R., Stoner B.R., and Thompson J.Y., “Effect of YSZ thin film coating thickness on the strength of a ceramic substrate”, *J. Mat. Sci. in Med.*, *in press* (2006).

Chapter 2

Literature Review and Fundamentals

This section will briefly detail the sputtering process, including how deposition parameters can affect the microstructure of thin films. In addition, there is a discussion on stresses within sputtered thin films and specific effects. Finally, there is a brief discussion of the properties of zirconia (bulk) and a review of sputter deposition of zirconia thin films.

2.1 Sputter Deposition

Early investigations of low pressure cathode ray tubes and plasmas revealed that cathodes within tubes can react or disintegrate during operation [1, 2]. In 1877, Wright was the first to report using this effect as a mechanism to deposit thin coatings to platinize glass [3]. Later in 1891, Crookes described this effect for several different metals [4]. It wasn't until Thompson's discovery of the electron, that this effect, what is now termed sputtering, could accurately be explained based on atomic structure [5, 6]. Thus, the mechanisms of momentum transfer from plasma ions causes target material (cathode) to be ejected into the gas phase and deposited on a nearby substrate (anode). Since this time, much has been accomplished in the science of sputter-deposition of various materials, ranging from metals to oxides, onto numerous substrates [7, 8]. The

following discussion will detail the process of plasma vapor deposition (PVD) and more specifically, radio frequency (RF) magnetron sputtering.

The versatility of sputtering processes often allows one to tailor film properties in ways not viable through other deposition techniques. This versatility arises from the many possible permutations and combinations of deposition process parameters. Several authors have reviewed the technique of sputtering, where they have detailed target kinetics, gas discharge phenomena, and sputtering equipment [8-11]. RF sputtering is widely used in a variety of applications ranging from aerospace to semiconductor industries. DC and RF-plasma techniques are the two most common forms of sputtering. DC is relegated to deposition of metals; where RF sputtering can be performed on all types of materials. One primary benefit of RF is the ability to deposit high melting point oxides at relatively low substrate temperatures.

Sputtering process occurs by bombarding the surface of a sputtering target with gaseous ions under high voltage acceleration. As the ions collide with the target, atoms or occasionally entire target material molecules are ejected and thrust towards the substrate where they coalesce and grow into a film (Figure 2-1). A typical plasma discharge will use argon (or some other noble gas) as a gas source, which results in a mixture of argon ions, electrons, and free neutral atoms. When a surface is bombarded by energetic ions, there are numerous effects that occur [12]:

- Emission of neutral (sputtered) particles
- Emission of secondary electrons
- Emission of positive and/ or negative ions
- Reflection of incident particles

- Desorption of gases
- Implantation of incident particles
- Heating
- Chemical dissociation
- Bulk diffusion
- Crystallographic changes
- Reflection of emitted species back to the target surface

This simple process allows for complex chemical compositions to be deposited on a wide variety of shapes, sizes, and materials.

The manner in which sputtered atoms migrate, interact and nucleate on the substrate surface is a function of many deposition process parameters; such as, substrate temperature, sputtering power, sputtering gas, and background pressure. Petrov *et al.* noted that film synthesis generally takes place far from thermodynamic equilibrium [13]. Film microstructure during deposition evolves in a competitive fashion and kinetic

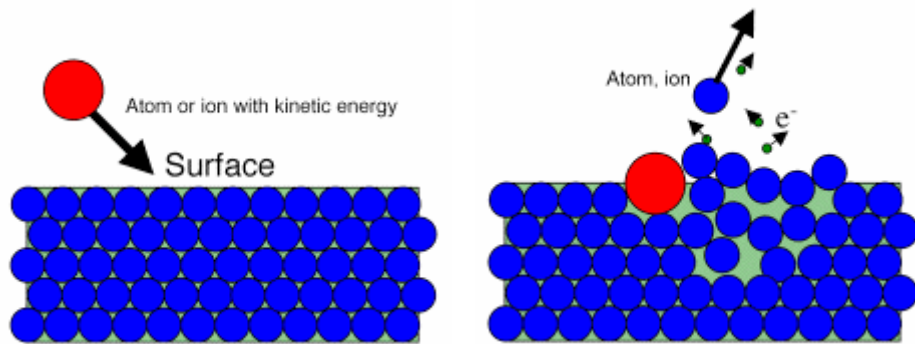


Figure 2.1: Representation of sputtering technique. The impact of an atom or ion on a surface produces sputtering from the surface as a result of the momentum transfer from the in-coming particle.

limitations (at low temperatures) allow for controlled growth. Two determinant factors in the evolution of film growth during deposition are surface and bulk diffusion. These processes, along with substrate temperature, are affected by the energetic particle bombardment, which control adatom mobilities and nucleation rates. Essentially, adatoms will diffuse around the substrate at a rate that depends on the energy at which atoms arrive, interactions with substrate atoms, and temperature of the substrate. Defects or surface permutations will act as energy sites for arriving atoms as they migrate across a surface. Therefore, due to surface diffusion and nucleation processes, sputtering can be used to preferentially coat or alter surfaces. In the absence of surface defects, the atoms will diffuse randomly across the substrate surface until a stable cluster is formed. This cluster acts as a nucleation site and subsequent grain growth occurs. Continual adatom addition leads to the texture evolution of grain growth and final film growth structures.

Thornton detailed film-atom condensation as a three step process. First, incident atoms transfer kinetic energy to the lattice and become loosely bonded adatoms. Secondly, the adatoms diffuse over the surface and due to energy transfer, eventually are desorbed or trapped at low-energy lattice sites. Thirdly, the incorporated atoms achieve final positioning within the lattice via bulk diffusion. This process of atomic layering can be broken down into four basic processes: (1) shadowing (interaction between surface roughness and angle of incident of arriving atoms), (2) surface diffusion, (3) bulk diffusion, and (4) desorption. These four processes can be expected to dominate over a range of temperatures (T/T_M), which dictates the structure of deposited thin film.

These interactions led to the development of the Thornton Diagram, which describes film structure as a function of temperature (T/T_M) and pressure (Figure 2-2).

The T/T_M dependence results because the surface and bulk diffusion processes dictate recovery and recrystallization. Here, pressure is a function of the collisions between the sputtered atoms and the gas atoms at elevated pressures causing sputtered atoms to arrive at the substrate at random directions, promoting self-shadowing. The following describes each zone shown in Figure 2-2:

- Zone 1 is characterized by a structure of tapered, columnar crystallites separated by open, voided grain boundaries. This structure is formed due to shadowing caused by substrate surface roughness / angle of incidence, where the peaks on the substrate surface will receive a higher flux of sputtered atoms than the valleys.

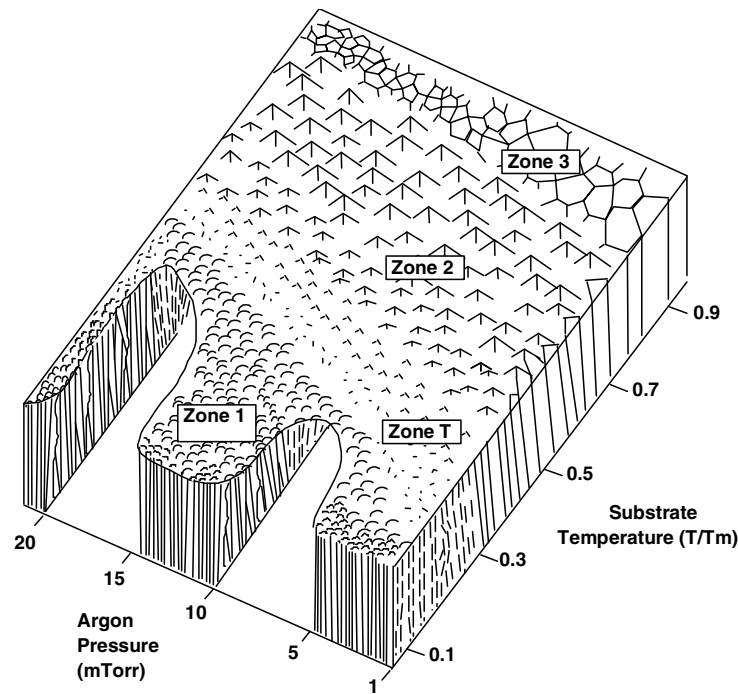


Figure 2.2: Representation of the influence of substrate temperature and argon pressure on the microstructure of sputter-deposited thin films [12].

- Zone T regions have a dense, fibrous structure with smooth, highly reflective surfaces. Generally, smooth films are grown at low T/T_M with the flux normal to the substrate surface so the shadowing effects are limited. It should be noted that films deposited within this zone typically display high intrinsic stresses.
- Zone 2 is characterized as columnar grains that are separated by dense, inter-crystalline boundaries and approaches a more equiaxed grain structure. The evolutionary growth of this structure, where $T/T_M > 0.30$, is due to adatom diffusion.
- Zone 3 structure is differentiated by bulk diffusion at $T/T_M > 0.50$, where recrystallization and grain growth dominate. Grain shape tends to be more equiaxed than columnar and is not influenced by substrate roughness.

Another important issue in thin film structure is the thickness dependence of microstructure and especially the transition from the nucleation region to the fully developed columnar grain structure. Thin film structure based on deposition parameters was discussed above, but there are three commonly observed nucleation and growth types that are related to the structure diagram reported by Thornton [8].

1. A three-dimensional island formation growth model, better known as the Volmer-Weber model, where nucleation is heterogeneous and associated with substrate defects and texture. Growth of the nuclei leads to island formation and coalescence into a continuous film with either columnar or isotropic microstructure (this is dependent on the deposition conditions previously mentioned in the structure zone models).

2. Frank-Van der Merwe growth model, where nucleation is homogeneous. The arriving adatoms stick virtually anywhere on a uniform crystalline substrate. The following adatoms complete the monolayer rather than clustering to form islands. This type of growth leads to epitaxy.
3. Stranski-Krastanov growth, describes a higher advanced intermediate model with continuous layers forming before island formation.

As described above, typical sputtered thin films, unless deposited at high temperature ($T/T_M > 0.50$) or annealed, are columnar in nature. It has been reported that bombarding the growing film with energetic particles (ions or neutrals), a more equiaxed grain structure can be obtained at low deposition temperatures. One of the simplest means of doing this in an RF-sputter system is to apply a negative substrate bias. This will result in bombardment by ions from the plasma to create a highly dense, adherent film.

Substrate biasing has been used to modify a broad range of film properties, including film adhesion during initial stages of film growth, film density, film hardness, film residual stress state (either tensile or compression), and film morphology [14]. Hakansson *et al.* examined the effect of bias voltage on the microstructure of TiAlN thin films [15]. As mentioned earlier, a film deposited without a substrate bias displayed a columnar grain structure with a high number of voids. As a bias is applied there is a gradual densification of the film due to ion impacts, known as ion-peening. At higher bias voltages, the columnar grain structure becomes disrupted and the microstructure can be termed more equiaxed. This is thought to be due to secondary nucleation within the growing film caused by the high-energy particle bombardment. Petrov *et al.* reported

that TiN films deposited at low temperatures and without substrate biasing were found to be under-dense with voids at the grain boundaries as well as within the grains [13]. Increasing the bias voltage, led to a decrease in void fraction in the films and with a 200V bias, a fully dense microstructure was evident. There have been many other reports on the densification of films due to substrate biasing that detail similar results.

2.2 Stress in Sputter-Deposited Thin Films

Internal, or residual, stresses have been extensively studied over the years within evaporated and sputtered thin films. Most of the current understanding in this area is based on analysis of the deposition of metallic films. It is accepted that essentially all metallic and inorganic thin films are in a state of stress. The internal stress is comprised of two factors: thermal (σ_{th}) and intrinsic (σ_i) components [8]:

$$\sigma_f = \sigma_{th} + \sigma_i \quad [\text{Eqn. 2.1}]$$

The thermal stress is due to the difference in thermal coefficients of expansion between the substrate and deposited film. The intrinsic stress is due to the accumulation of crystallographic flaws that develop during film growth.

This stress behavior, shown in Figure 2.3, can be quantified by using the Stoney equation that equates bow or bend to internal stress magnitude. Figure 1(a) describes a behavior where the growing film initially shrinks relative to the substrate. There can be a multitude of reasons for this to happen, for example surface tension forces or lattice mismatch during epitaxial growth. However, based on the constraints of the system, it requires that the film and substrate have the same dimensions. Therefore, the film will

stretch and substrate contract to accommodate the constraints. Here the tensile forces within the film are balanced by the compressive forces in the substrate, which in an

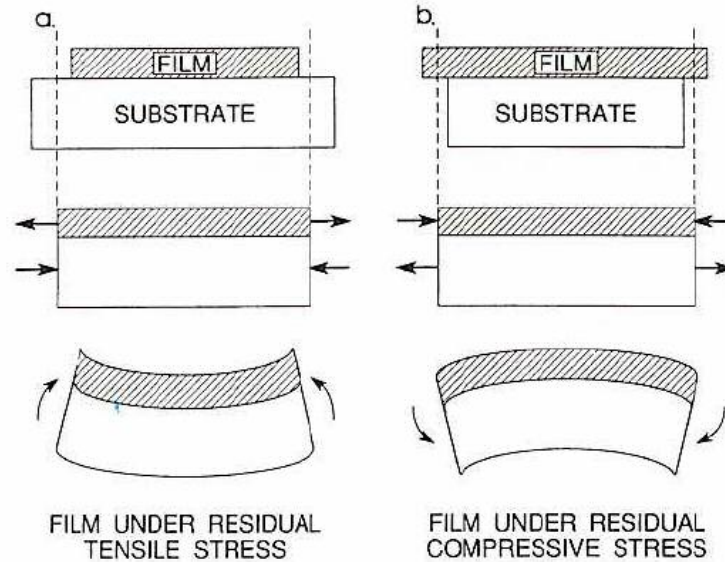


Figure 2.3: Diagram describing (a) residual tensile stress and (b) residual compressive stress in thin films [8].

unconstrained system would elastically bend to compensate the unbalanced moments. Similarly residual compressive stress, where the film wants to be larger than the substrate, would elastically bend the substrate, but in the opposite direction. The forces created by films stresses can be sufficient enough to destroy the film-substrate composite. For example, a tensile stress could cause the film to crack and/or fracture and compressive stress could cause spalling and/or lose of adhesion. The following sections will take a further look into thermal and intrinsic stresses with sputtered thin films.

2.2.1 Thermal Stresses

When applied to a film that has been deposited at elevated temperature and then cooled, the film will be thermally stressed, especially if the substrate and film have large

differences in coefficient of thermal expansions (CTE). For example, for a film deposited at elevated temperatures where the CTE of the substrate is larger than the CTE of the film, the film will be residually compressed. This stress can be described by the following formula:

$$\sigma_{th} = (E_f / (1 - \nu_f)) (\alpha_f - \alpha_s) (T_s - T_a) \quad [\text{Eqn. 2.2}]$$

where E_f is Young's modulus, ν_f is Poisson's ratio, α_f and α_s are the coefficients of thermal expansion for the film and substrate, T_s is substrate temperature during deposition and T_a is substrate temperature during measurement. At low T/T_M , it is intrinsic stress generally dominates over the thermal stress (Figure 2-4).

2.2.2 Intrinsic Stresses

It has been well documented that intrinsic stresses are indeed found within sputtered thin films and the magnitude and direction (compressive or tensile) are dependent on a deposition parameters. The parameters that are expected to influence film stress are: (1) substrate temperature, (2) working gas species and pressure, (3) deposition power, (4) angle of incidence, (5) apparatus geometry, (6) distance between cathode and substrate, and (7) substrate bias. The production, energy, and path length of neutralized gas atoms as a function of deposition parameters are important in the generation of stresses [11, 16-21].

Pressure, or observed pressure (P_t), is an important deposition parameter where there is a crossover from tensile to compressive stress [22, 23]. It is noted that at elevated pressures, gas scattering of the sputtered material will approach the substrate in oblique directions promoting a more open structure that yield a tensile stress. Below a system

specific transition pressure, films are in compression, due to high reflectance and low resistivities, and often contain trapped working gas.

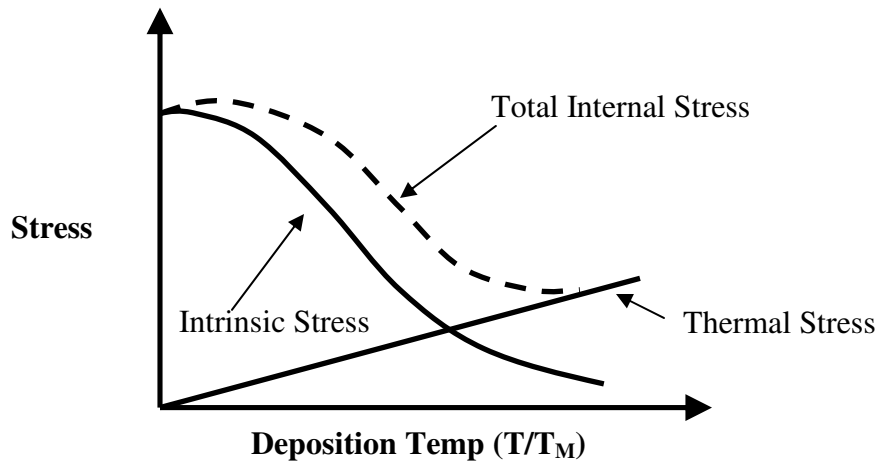


Figure 2.4: Schematic representation of thermal and intrinsic stress contributions [16].

Deposition conditions of deposited films are critical variables when discussing a film's microstructure and subsequent intrinsic stress. Figure 2-2 is a representation of how a film's microstructure (surface topography and cross-sectional grain structure) is directly related to substrate temperature and working gas pressure. Many have reported that sputter-deposition involves atoms that depend on arrival directions and surface roughness promoting self-shadowing, and then diffusing over the surface until satisfying low energy sites and becoming incorporated into the growing film. The dependence of substrate temperature and pressure can be generalized by the following: T/T_M effects are believed to be due to the surface diffusion processes, and pressure results in collisions between sputtered atoms and working gas atoms at higher pressures creating a randomized arrival that supports self-shadowing.

The mass of both the target species and sputtering gas used can result in varying effects on film stress. It has been reported that the higher the atomic mass of the target

material, then the higher the energy of the backscattered atoms [23]. High mass target atoms have been reported to increase the transition pressure between tensile and compressive stresses. Also, the mass of the gas species used can affect this transition pressure. Although argon is the most commonly used gas, a lighter gas (i.e. Neon) produces a higher transition pressure, while a heavier/larger gas (i.e. Xeon) lowers the transition pressure.

Recovery has been reported as a mechanism where stresses in the film actually house energy that acts as a thermodynamic driving force which can relax the stresses. This is accomplished by vacancy, interstitial, or dislocation movement if the temperature is such the T/T_M is between 0-0.3. Another phenomenon, know as recrystallization, is reported to take place at higher temperatures (T/T_M 0.3-0.5), where stresses are relaxed from the recrystallization of strained grains into new strain-free grains. Therefore, for depositions at substrate temperatures greater than 0.2 T/T_M , recovery and recrystallization will relax intrinsic stresses within the film and also reduce the buildup of stresses during growth.

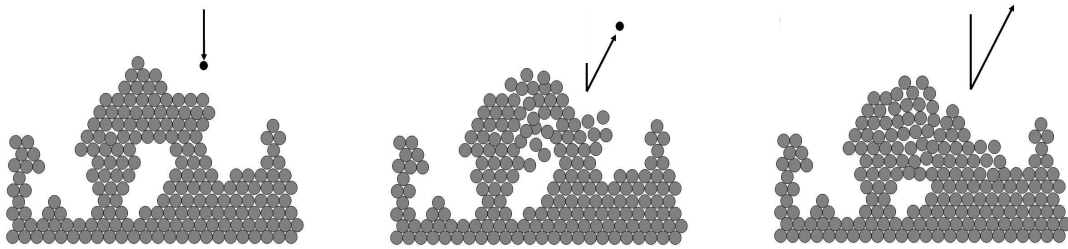


Figure 2.5: Process of ion-peening: (a) an ion approaches the surface of a film with in-grown voids, (b) the ion impacts the film, transferring energy to the film atoms, (c) causing atoms to rearrange, filling in part of the defect, resulting in a denser film. [24].

The use of a substrate bias during deposition can make a drastic impact on the stresses within a film. Ion energy bombardment during sputter deposition is commonly used to increase film density. This bombardment would essentially tamp the growing film, collapsing voids and producing re-coil implantation. Figure 2-5 is a representation of the ion-peening process that describes the ion impact energy which transfers its energy to growing film atoms, causing atomic rearrangement resulting in a denser film [24]. Thornton and Hoffman described what is termed re-coil implantation, which at higher bias voltages will increase the energy reflected atomic species and ions passing to the substrate (Figure 2-6). The impact at the substrate can cause re-coil implantation of a surface atom and implantation of the working gas atom [23, 25].

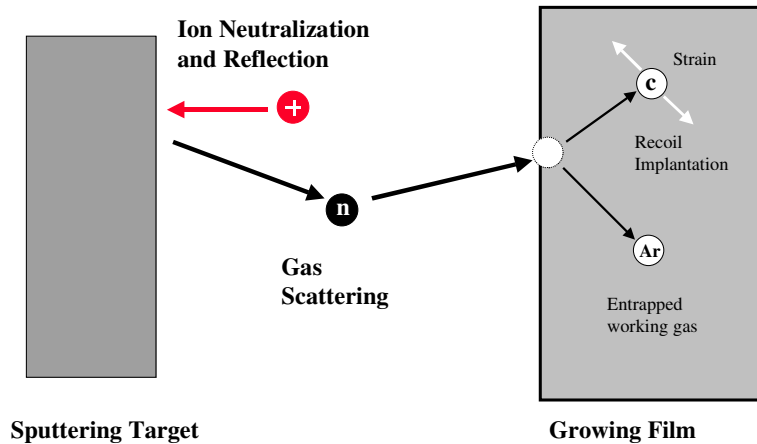


Figure 2.6: Representation of the process responsible for producing compressive stresses and entrapped working gas in sputter-deposited thin films [23].

2.3 Zirconia as a Material

Zirconia (ZrO_2) and yttria-stabilized zirconia (YSZ) thin films, due to the unique properties of the material, have long been investigated for everything from biomedical applications [26] to sensor technologies [27] to thermal barriers [28]. Zirconia is a well studied polymorph that at atmospheric pressure can exist in three distinct crystal

structures: monoclinic (M) the low temperature phase and two high temperature phases, tetragonal (T) and cubic (C). Figure 2-7 is the phase diagram for yttria-stabilized zirconia [29]. A $T \Rightarrow M$ transformation occurs when PSZ is cooled below a temperature of approximately 1100°C. This phase transformation is associated with a volume expansion

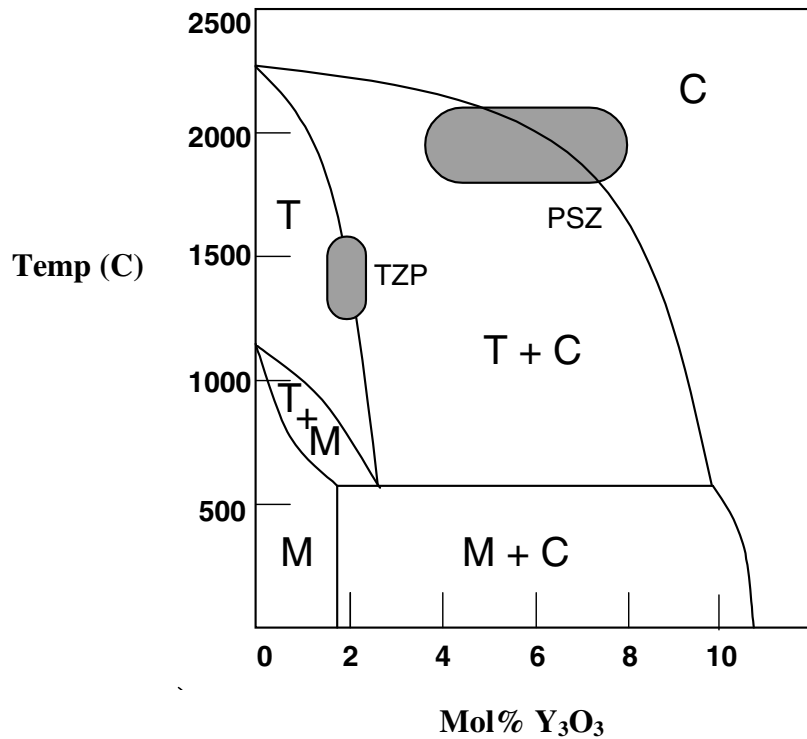


Figure 2.7: ZrO₂ rich sections of the phase diagrams for ZrO₂-Y₂O₃ [29].

of approximately 3-4% within the material structure. Stresses generated by the expansion originate cracks in pure zirconia ceramics and may cause catastrophic failure when this material is heated to elevated temperatures.

For the purposes of this thesis, the tetragonal and monoclinic phase structures are of interest. The tetragonal phase is thermodynamically stable in bulk zirconia at temperatures ranging from 2380° to 1100°C. Two aspects differentiate it from the other structures: (1) there is a distortion in the lattice, due to an elongation along the c-axis and

(2) there is a displacement of columns of oxygen atoms along the c-axis leading to each zirconium atom maintaining its 8-fold coordination of oxygen [30]. It is described by the space group of the body-centered with a primitive unit cell of $P4_2/nmc$ [31]. The monoclinic phase is thermodynamically stable in bulk zirconia at temperatures below 1100°C. It can be described as a distorted cubic cell, and unlike the other phases each zirconium atom is coordinated by 7 oxygen atoms. This structure is indexed with the space group $P2_1/c$ [32].

2.3.1 Phase Stabilization

It is well known that with the addition of stabilizing dopants' such as CaO, MgO, CeO₂, Y₂O₃, will alter the stability of the above mentioned phases [30, 33-35]. This allows for the transformation temperatures to be lowered and the tetragonal or cubic phases may become metastable at room temperatures. The mechanism of stabilization is generally associated with the presence of oxygen vacancies in the lattice [30]. These are created for charge neutrality, balancing of the di- or trivalent cations which are substituted in the Zr⁺⁴ sites. Other critical factors include the size of the stabilizing cation and crystal structure of the dopant oxide [30, 33, 36]. All these mechanisms have been investigated and reviewed extensively in the references cited.

2.3.2 Phase transformation (T⇒M)

Zirconia that is partially-stabilized (PSZ) contains a mixture of phases and has been studied as an engineering material with high toughness [34]. This toughness has been attributed to the metastable tetragonal phase transforming to a stable monoclinic phase [30, 37]. Garvie *et al.* showed how to best utilize this transformation as a toughening mechanism as an engineered material [38]. Experimental observation (Figure

2.8) showed that finely dispersed tetragonal precipitates within a cubic matrix were transformed to monoclinic phase when the constraint exerted on them by the matrix was relieved by an advancing crack [37, 39]. This rapid transformation is also accompanied by a 3-4% volumetric expansion, which can apply an opposing force on advancing cracks

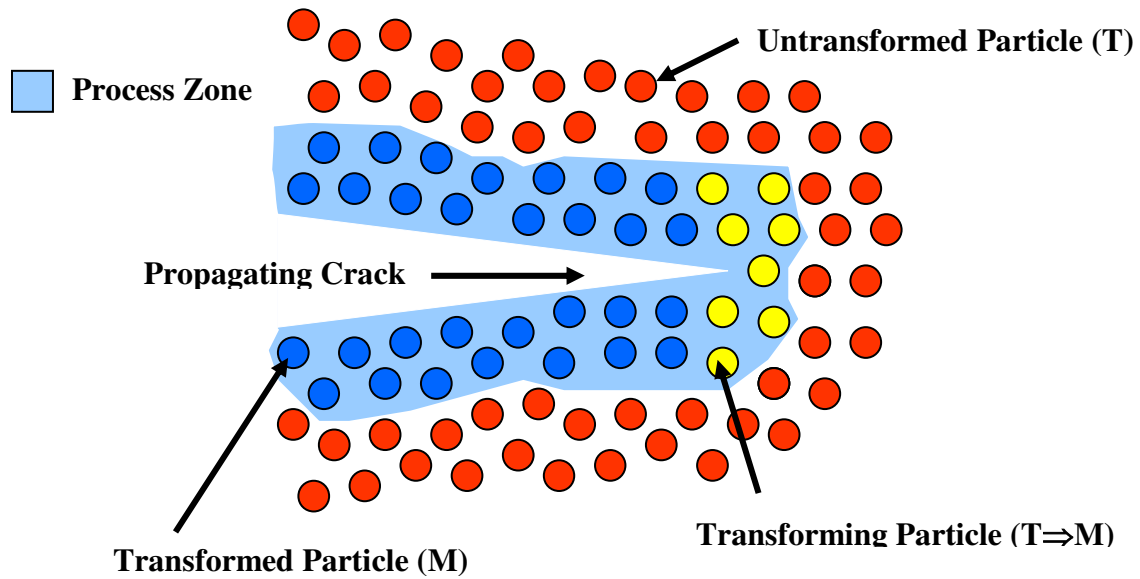


Figure 2.8: Representation of stress-induce phase transformation ($T \Rightarrow M$) toughening process. The energy of the advancing crack is dissipated in phase transformation and in overcoming the matrix constraint by transforming grains [37, 39].

and/or cause considerable cracking in the dense matrix. The nature of $T \Rightarrow M$ transformation is dominated by two factors: (1) a sharp change in volume and (2) martensitic character. The change in volume essentially reduces the density which allows stress to affect each phase's thermodynamic stability. A compressive stress will ultimately decrease the thermodynamic transformation temperature [30]. Secondly, the rapid and displacive nature of the martensitic transformation means that the kinetics are dominated by nucleation, which is also strongly affected by stress [34].

2.3.3 Deposition of Zirconia

Multiple techniques of depositing YSZ thin films have been investigated; such as, sol-gel processing [40], electron beam physical vapor deposition [41, 42], plasma spray [27], and RF magnetron sputtering [43-49]. The focus of this research is the deposition via RF magnetron sputtering. Amor *et al.* detailed a comprehensive investigation into the properties of RF-magnetron sputtered zirconia thin films deposited from a pure (99.6%) zirconia target. The authors studied the effect of sputtering parameters (RF power, oxygen partial pressure, and total pressure) on the microstructure, optical properties of the films, composition, and film stress.

Initial investigations described film growth rate as a function of deposition parameters. Here, it is reported that deposition rate is dependent on RF power. As power increases, the self-polarization potential increases, which leads to an increase in energy for argon ions and electrons. This ultimately increases the ion density around the cathode (target) and the sputtering yield increases. As a result, the deposition rate increases. It was also noted that induction of oxygen into the sputtering gas decreases the rate. As oxygen partial pressure increases, the average energy of the species bombarding the target decreases, so the deposition rate is reduced. At high pressures, the mean free path of the sputtered species is decreased, which also leads to a lower rate. When pressure is lower, the ion density decreases and so does the amount of sputtered material.

Index of refraction data yielded an important relationship between film optical and microstructural properties. By using the Bragg-Pippard model, a qualitative analysis of packing density for each film was calculated which can be correlated to the film's

porosity [8]. A more defective film will have a lower refractive index, since voids (dry or water filled) have a much lower index of refraction than fully dense zirconia.

All films were reported to display a compressive film stress, which originates from the thermal and intrinsic components. A variation in magnitude was shown to increase compressively with coating thickness. It was also noted that at low pressures, due to the sputtered species and backscattered neutrals having sufficient energy to reach the substrate with normal incident angle causing re-coil implantation, films displayed high compressive stresses. Increasing pressure reduced the atomic bombardment resulting in structural reorganization, decreasing the magnitude of compressive stresses.

Structural studies have investigated phase content as it is related to specific parameters. Depositing with pure argon as the sputtering gas, the films crystallized in the cubic phase. Since the cubic phase is stable at high temperature and deposition did not exceed 140°C, the authors attributed the stabilization of cubic phase to the substoichiometric nature of the film. Reports have confirmed that cubic phase can be stabilized by an increase in oxygen vacancies [30]. There was also a strong dependency on pressure and crystallinity. At low sputtering pressures, films display a <200> texture and as pressure is increased, a <111> texture. It was finally shown that at the highest pressure the film became amorphous.

Ruddell *et al.* and Wang *et al.* studied phase structure characteristics of RF sputtered zirconia thin films doped with Y₂O₃ [44, 45]. XRD revealed that varying percentages of monoclinic to tetragonal phase films could be deposited. Depositions without oxygen produced films with high amounts of tetragonal phase due to the substoichiometric nature. Adding oxygen to the sputtering gas allowed for the

monoclinic phase to be stabilized. Increasing the oxygen content decreases the film growth rate, which allows the film more time to achieve the thermodynamically stable configuration. Both studies used a simple method of evaluating the ratio of the volume fraction of the monoclinic and tetragonal phases. This was done by comparing the intensities of the $M_{(111)}$ and $T_{(111)}$ peaks according to the following equation [45]:

$$V_M = 2.379 I_{M(111)} / (I_{M(111)} + I_{T(111)}) \quad [\text{Eqn. 2.3}]$$

Where $I_{M(111)}$ and $I_{T(111)}$ are the integrated intensities of the (111) monoclinic and (111) tetragonal peaks, respectively, and 2.379 is a correction coefficient. This provides a fitting way to calculate the percentages of each phase present.

Utilizing a substrate bias has been a technique that can alter the crystal structure and microstructure of sputter-deposited YSZ thin films. *Knoll et al.* reported on sputter-deposited zirconia films with varying percentage of yttria (3 to 15 mol%) with differing powers of substrate bias [51]. It was shown that biasing did not affect crystal structure, although film microstructure, stress, and crystallographic texture changed as bias voltage increased. For the biased films, the grains were more densely packed and appeared more strained in the TEM analysis. Although stress was not quantified, noticeable bowing was reported on substrates with biased film. Another study by the same authors, reported as negative bias increased, that film morphology changed from porous and columnar to dense and deformed looking in correspondence to the increase in compressive stress in the YSZ film [52]. In the low bias films, porosity ranged in scale from large inter-columnar cracks to small inter-granular voids. Lattice defects produced by the ion bombardment were thought to be the likely cause of higher compressive stress in the biased YSZ films.

As mentioned in the introduction (Chapter 1), research has started to investigate developing transformation-toughened ceramic films. For a film to be of practical use, not only must it contain a significant amount of tetragonal phase ($t\text{-ZrO}_2$), but this phase must also transform locally to the monoclinic phase ($m\text{-ZrO}_2$) in response to an applied stress. In bulk zirconia, with a dopant stabilizing the tetragonal phase, the $T \Rightarrow M$ transition can be auto-catalytic, resulting in widespread transformation of the parent phase [50]. One group has reported on a transformation $T \Rightarrow M$ in zirconia-alumina nanolaminates grown by reactive sputter deposition. The authors did not incorporate any stress effects on the transformation, but did note, unlike bulk zirconia, the martensitic transformation was localized to nanosized regions [53-57].

This literature review is to provide some insight into the sputter-deposition technique, zirconia as an engineering material, and a review of previously reported studies on sputter-deposition of YSZ. Noted references provide more detailed information into all the above mentioned topics. The following chapters will take a further look into RF magnetron sputter-deposition of 3mol% YSZ and subsequent material properties.

2.4 References

1. Plücker J., *Annalen der Physik und Chemie*, **59**, 67-86 (1858).
2. Grove W.R., “On the electro-chemical polarity of gases”, *Trans. Roy. Soc. Lon.*, **142**, 87-101 (1852).
3. Wright D., *Amer. J. of Sci. & Arts*, **12**, 49-62 (1887).
4. Crookes W., “On electrical evaporation”, *Proc. Roy. Soc. Lond.*, **50**, 88-105 (1891).
5. Smith G.E., “J.J. Thomson and the electron: 1897-1899 An Introduction”, *Chem. Educ.*, **2**(6), 1-47 (1997).
6. Thomson J.J., “A theory of the connexion between cathode and Rontgen rays” *Philosophical Magazine*, **46**, 528 (1898).
7. Bunshah R.F., *Handbook of deposition technologies for films and coatings: science, technology, and applications*, (Noyes, NJ (1994)).
8. Ohring M., *The Materials Science of Thin Films*, (Academic Press, London, 1992).
9. Chopra K.L., *Thin Film Phenomena*, (McGraw-Hill, NY, 1969).
10. Wehner G.K. and Anderson G.S., *Handbook of Thin Film Technology*, edited by L.I. Maissel and R. Glang (McGraw-Hill, NY, 1970).
11. Vossen J.L., “Control of film properties by rf-sputtering techniques”, *J. Vac. Sci. Technol.*, **8**(5), S12-S30 (1971).
12. Thornton J.A., “Influence of apparatus geometry and deposition conditions on the structure and topography of thick sputtered coatings”, *J. Vac. Sci. Technol.*, **11**(4), 666-670 (1974).
13. Petrov I., Barna P.B., Hultman L., and Greene J.E., “Microstructural evolution during film growth”, *J. Vac. Sci. Technol. A*, **21**(5), S117-S128 (2003).
14. Powell R.A. and Rossmagel S.M., “*PVD for microelectronics: Sputter deposition applied to semiconductor manufacturing*”, (Academic Press, CA, 1994).
15. Hakansson G., Sundgren J.E., McIntyre D., and Greene J., “Microstructure and physical properties of polycrystalline metastable $\text{Ti}_{0.5}\text{Al}_{0.5}\text{N}$ alloys grown by DC magnetron sputter deposition”, *Thin Solid Films* **153**, 55-65 (1987).
16. Thornton J.A. and Hoffman D.W., “Stress-related effects in thin films”, *Thin Solid Films*, **171**, 5-31 (1989).

17. Muller K-H, "Stress and microstructure of sputtered-deposited thin films: Molecular dynamics investigations", J. Appl. Phys., **62**(5), 1796-1799 (1987).
18. Windischmann H., "Intrinsic stress in sputtered thin films", J. Vac. Sci. Technol. A, **9**(4), 2431-2436 (1991).
19. Koch R., "The intrinsic stress of polycrystalline and epitaxial thin metal films", J. Phys.: Condens. Mater., **6**, 9519-9550 (1994).
20. Buckel W., "Internal stress", J. Vac. Sci. Technol., **6**(4), 606-609 (1969).
21. Hoffman R.W., "Stresses in thin films: The relevance of grain boundaries and impurities", Thin Solid Films, **34**, 185-190 (1976).
22. Hoffman R.W., "Perspective on stresses in magnetron-sputtered thin films", J. Vac. Sci. Technol. A, **12**(4), 953-961 (1994).
23. Thornton J.A. and Hoffman R.W., "The influence of discharge current on the intrinsic stress in Mo films deposited using cylindrical and planar magnetron sputtering sources", J. Vac. Sci. Technol. A, **3**(3), 576-579 (1985).
24. Itoh, T., *Ion Beam Assisted Film Growth*, (Elsevier, Amsterdam, 1989).
25. Cuomo J.J. and Gambino R.J., "Incorporation of rare gases in sputtered amorphous metal films", J. Vac. Sci. Technol. **14**(1), 152-157 (1977).
26. Thamaraiselvi T.V. and Rajeswari S., "Biological evaluation of bioceramic materials- A review", Trends Biomater. Artif. Organs, **18**(1), 9-17 (2004).
27. Moseley P.T, Norris J., and Williams D.E., *Techniques and Mechanisms in Gas Sensing*, (Bristol, UK, 1991).
28. Scardi P, Lutterotti L, "Microstructural characterization of plasma-sprayed zirconia thermal barrier coatings by X-Ray-diffraction full pattern-analysis", Surface and Coatings Technology **61**, 52-59 (1993).
29. Hannink R.H.J., Kelly P.M., and Muddle B.C., "Transformation toughening in zirconia-containing ceramics", J. Am. Ceram. Soc., **83**[3], 461-487 (2000).
30. Kisi E.H. and Howard C.J., "Crystal structure of zirconia phases and there inter-relation", Key Eng. Mater., **153-154**, 1-36 (1998).
31. ASTM Joint Committee on Powder Diffraction Standards, 1974, File Nos. 37-1484.
32. ASTM Joint Committee on Powder Diffraction Standards, 1974, File Nos. 17-923.

33. Yoshimura M., "Phase stability of zirconia", Bull. Am. Ceram. Soc., **67**[12], 1950-1955 (1988).
34. Heuer A.H., Chaim R., and Lanteri V., "Review: Phase transformations and microstructural characterization of alloys in the system $\text{Y}_2\text{O}_3\text{-ZrO}_2$ ", Adv. in Ceram., **24**, 3-20 (1988).
35. Garvie R.C., "A personal history of the development of transformation toughened PSZ ceramics", Mater. Sci. Forum, **34-36**, 65-77 (1988).
36. Howard C.J., Hunter B.A. and Kim D-J, "Oxygen position and bond lengths form lattice parameters in tetragonal zirconia", J. Am. Ceram. Soc., **81**[1], 241-243 (1998).
37. Butler E.P., "Transformation-toughened zirconia ceramics", Mater. Sci. Technol, **1**, 417-431 (1985).
38. Garvie R.C., Hannink R.H. and Pascoe R.T., "Ceramic Steel?", Nature, **19**, 703-704 (1975).
39. Piconi C. and Maccauro G., "Zirconia as a ceramic biomaterial", Biomaterials, **20**, 1-25 (1999).
40. Diaz-Parralejo A., Caruso R., Ortiz A.L., and Guiberteau F., "Densification and porosity evaluation of $\text{ZrO}_2\text{-3mol\% Y}_2\text{O}_3$ sol-gel thin films", Thin Solid Films **458**, 92-97 (2004).
41. Kao A.S. and Gorman G.L., "Modification of zirconia film properties by low-energy bombardment during reactive ion-beam deposition", J. Appl. Phys. **67**, 3826-3834 (1990).
42. McKeenenzie D.R., Cockayne D.J. and Netterfield R.P., "Microstructure of zirconia films deposited with ion assistance", J. Mater. Sci. **22**, 3725-3731 (1987).
43. Rivière J.P., Harel S., Guerin P., and Straboni A., "Structure of ZrO_2 optical thin films prepared by dual beam reactive sputter deposition", Surf. Coat. Technol. **84**, 470-475 (1996).
44. Ruddell D.E., Stoner B.R., and Thompson J.Y., "The effect of deposition parameters on the properties of yttria-stabilized zirconia thin films", Thin Solid Films **445**, 14-19 (2003).
45. Wang Y.H. and Li X.P., "Phase-Structure Characteristics of RF Reactively Sputtered Zirconia Thin-Film", Thin Solid Films **250**, 132-134 (1994).

46. Liaw B.Y., Rocheleau R.E., and Gao Q., "Thin Film Yttria-Stabilized Tetragonal Zirconia", *Solid State Ionics* **92**, 85-89 (1996).
47. Gao P., Meng .L.J, dos Santos M.P., Teixeira V., and Andritschky M., "Study of ZrO₂-Y₂O₃ Films Prepared By RF Magnetron Reactive Sputtering", *Thin Solid Films*, **377**, 32-36 (2000).
48. Amor S.B., Rogier B., Baud G., Jacquet M., and Nardin M., "Characterization Of Zirconia Films Deposited By RF Magnetron Sputtering", *Mater. Sci. Eng. B* **57**, 28-39 (1998).
49. Tomaszewski H., Haemers J., Denul J., De Roo N., and De Gryse R., " Yttria-stabilized zirconia thin films grown by reactive r.f. magnetron sputtering", *Thin Solid Films* **287**, 104-109 (1996).
50. Green D.J., Hannink R.H.J., and Swain M.V., *Transformation toughening of ceramics*, (CRC, Boca Raton, FL, 1989).
51. Knoll R.W. and Bradley E.R., "Microstructure and phase composition of sputter-deposited zirconia-yttria films", *Mat. Res. Soc. Symp. Proc.*, **30**, 235-243 (1984).
52. Knoll R.W. and Bradley E.R., "Correlation between the stress and microstructure in bias-sputtered ZrO₂-Y₂O₃ films", *Thin Solid Films*, **117**, 201-210 (1984).
53. Gajdardziska-Josifovska M. and Aita C.R., "The transformation structure of zirconia-alumina nanolaminates studied by high resolution electron microscopy", *J. Appl. Phys.*, **79**(3), 1315-1319 (1996).
54. Schofield M.A., Aita C.R., Rice P.M., and Gajdardziska-Josifovska M., "Transmission electron microscopy study of zirconia-alumina nanolaminates grown by reactive sputter deposition. Part I: zirconia nanocrystallite growth morphology", *Thin Solid Films*, **326**, 106-116 (1998).
55. Schofield M.A., Aita C.R., Rice P.M., and Gajdardziska-Josifovska M., "Transmission electron microscopy study of zirconia-alumina nanolaminates grown by reactive sputter deposition. Part II: transformation behavior of tetragonal zirconia nanocrystallites ", *Thin Solid Films*, **326**, 117-125 (1998).
56. Scanlan C.M., Gajdardziska-Josifovska M., and Aita C.R., "Tetragonal zirconia growth by nanolaminates formation", *Appl. Phys. Lett.*, **64**(26), 3548-3550 (1994).
57. Aita C.R., Wiggins M.D., Whig R., Scanlan C.M., and Gajdardziska-Josifovska M., "Thermodynamics of tetragonal zirconia formation in a nanolaminates film", *J. Appl. Phys.*, **79**(2), 1176-1178 (1996).

Chapter 3

Experimental Procedures

This chapter focuses on the methodology for the synthesis of 3mol% yttria-stabilized zirconia (YSZ) thin films by radio frequency sputter deposition. The sputter system configuration is outlined below, highlighting specific process parameters unique and critical to the study. Methods for film characterization are presented which were used to help develop process-structure-property relationships for the deposited films.

3.1 Substrate Materials

Substrate materials used were single-side polished 4in. (10.2 cm) Silicon (Si) and soda-lime glass wafers. Single crystal (100 orientation) Si substrates (Silicon Quest Int., Santa Clara, CA) were used for initial sputter-process film deposition. Specific substrate properties are shown in Table 3.1. The polished side was used for deposition rate determination, x-ray diffraction (XRD) studies, and index of refraction analysis. Deposition on the un-polished side ($R_a=0.4\mu\text{m}$) was used to enhance film adhesion and simulate end-application surface roughness. Film stress determination, XRD analysis, and structural studies (SEM and TEM) were performed on these samples.

Soda-lime glass wafers (Mark Optics, Santa Ana, CA) were used to simulate a low strength, inert, bio-material. The focus on strengthening brittle substrates extends to

materials such as dental porcelain and due to cost and availability; soda-lime glass wafers supplied the needed material properties to conclude this study. Depositions were performed on the roughened side ($R_a=0.4\mu\text{m}$) for XRD analysis and structural studies (SEM).

Substrate Material	Diameter (mm)	Thickness (μm)	Coefficient of thermal expansion (α , $\times 10^{-6} \text{ C}^{-1}$)	Modulus (GPa)	Dielectric Constant
Silicon	100	400 ± 100	3.0	150	11.9
Soda-Lime	100	400 ± 100	8.6	72	7.15

Table 3.1: Specific material properties for substrates used in this study.

3.2 Sputter Deposition Equipment/Parameters

The theory and flexibility of sputtering materials was discussed earlier, however it is necessary to discuss specific attributes and parameters of the sputter deposition system used in this study. Here, the deposition system and specific deposition parameters will be introduced and discussed.

3.2.1 Deposition System

All YSZ thin film depositions were sputtered using a radio frequency magnetron sputter system (CVC Model SC-400, Rochester, NY). The chamber achieves sufficient vacuum through a roughing pump and a cryogenic high-vacuum pump. The system was designed with four cathode locations, but for all deposition the center location was used. Power was supplied to the cathodes via two RF power supplies and matching networks (Advanced Energy Corp., Fort Collins, CO) with a maximum power output of 600W at a frequency of 13.56MHz. A schematic of the sputter deposition system used for this study is shown in Figure 3.1. For substrate bias depositions, a RF power supply generated the

power to the cathode (positioned in the substrate heater) that was capacitively coupled to the substrate holder. Since the chamber is grounded and the substrate holder (also much smaller) is floating, the RF creates a field that attracts free electrons, and due to charge neutrality and the fact that the gap between the heater and substrate holder acts as a capacitor, an effective DC plasma below the substrate is formed attracting free ions. This

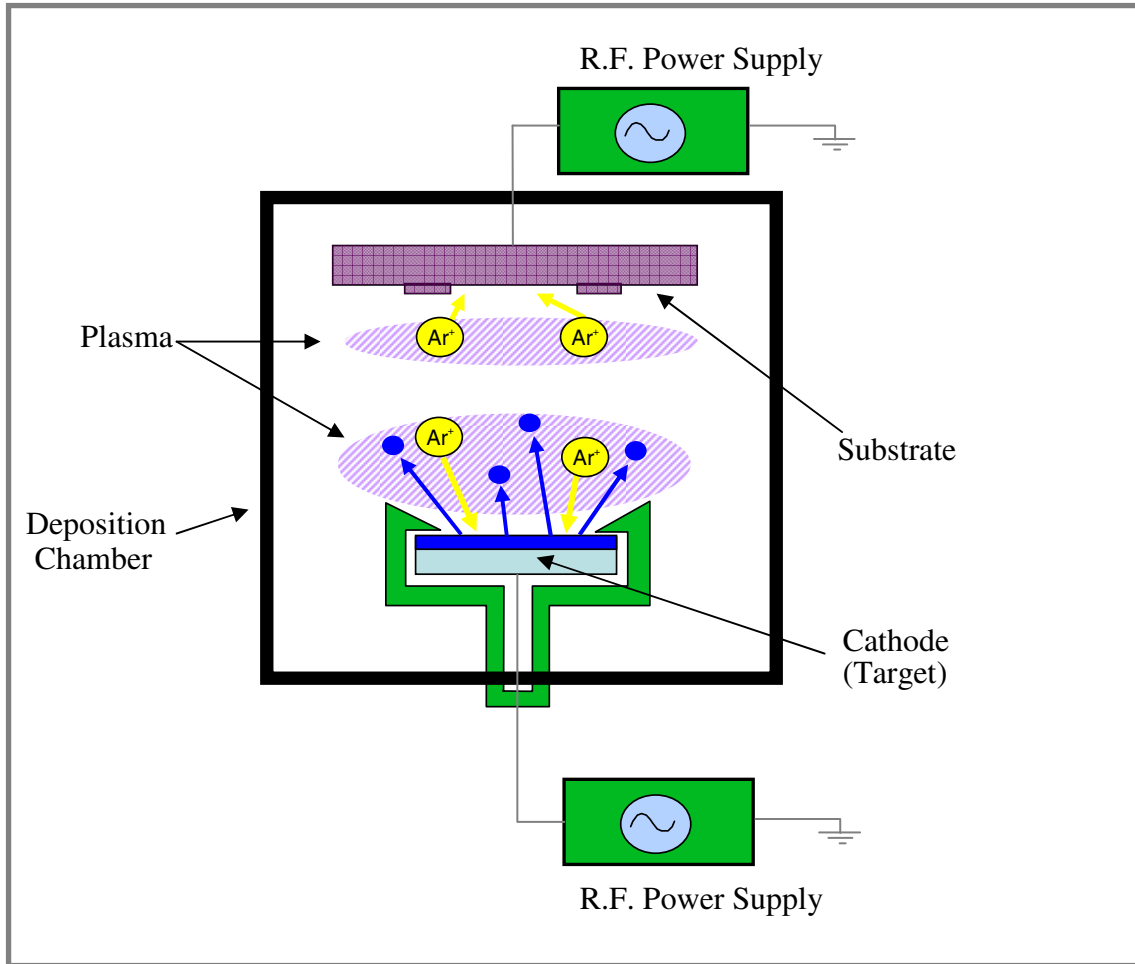


Figure 3.1: Representative schematic of sputter deposition system.

is where the ion-peening effect of substrate biasing occurs, which was described in Chapter 2. Positioned above the substrate holder, was a resistive heater with a maximum temperature of 600°C operated by a temperature (PID-loop) controller (West Corp.,

Gurnee, IL). Argon and oxygen, two sputtering gases used in the study, were independently controlled, and flowed into the chamber via two mass flow controllers (MKS Instruments, Wilmington MA). By altering specific deposition parameters, the likelihood of variation in thin film properties was increased. The next sections will review specific parameters used to study the YSZ films.

3.2.2 Power

A power of 350W was selected based on earlier studies and the target manufacturer's recommendation. When the RF power increases, polarization potential increases, which leads to an increase in electron and argon/oxygen ions kinetic energy. The sputtering gas ion density around the target increases the sputtering yield, consequently increasing the deposition rate. Earlier studies showed that deposition rates did not vary greatly. However, higher power densities were shown to crack the target.

3.2.3 Substrate Bias

The term substrate bias refers to the purposeful bombardment of a growing film by energetic ions. A substrate applied bias results in a sharp transition between low compressive to very high compressive stress as bias is increased [1-4]. Thornton reported that for both cases, the microstructure of a film changes from columnar grains with inter-granular porosity to a more dense, equiaxed grain structure as stress transitions from tensile to compressive [5]. It has been reported that at low energies ($<100\text{eV}$), energetic ions essentially tamp atoms into the growing film [6]. As ion energy increases, the secondary nucleation can take place, resulting in conversion from columnar to an equiaxed grain structure [7]. For this study substrate bias was varied to achieve specific

structures. A maximum power of 50W was used when depositing on silicon and 100W for soda-lime glass.

3.2.4 Deposition Pressure (working)

Pressure is an important parameter that not only affects deposition rate, but has a significant affect on film stress. The production, energy, and path length of sputtered atoms, reflected neutrals, and ions are dependent on pressure. At low working pressures, sputtered atoms and backscattered species will have sufficient energy to arrive with low incident angle. The resulting interactions enhance diffusion of surface atoms and can produce recoil implantation into the growing film, creating a compressive film stress. Higher pressures will increase the scattering of neutrals, decreasing energy of the atoms impacting the surface, effectively reducing the compressive film stress. It has been reported that for sputter deposited thin films there is an observed pressure where there is a sharp transition from tensile to compressive film stress [8, 9]. For the initial study on sputter deposited YSZ thin films, deposition pressure was altered between 5, 15, and 25 mT.

3.2.5 Substrate Temperature

Initial studies examined a substrate temperature range between room temperature (25°C) and 300°C. The temperature range was selected based on previous work and on cooling of substrate materials post-deposition. The importance of deposition at higher temperatures has been correlated to film properties (i.e. film stress, defect structure). Thermal stress and its effects are discussed in Chapter 2. A higher substrate temperature leads to an increase in size of the critical nucleus, which dictates how a film nucleates and grows. As temperature increases, the adatoms arrive at the surface with energy, and

are more likely to attain positions of equilibrium. This would translate into a film with larger, more equiaxed grains. Furthermore, this structure promotes a denser film with fewer defects.

3.2.6 Oxygen (sputtering gas)

When sputtering oxide materials (insulators), the addition of oxygen plays a significant role. One drawback shown in Chapter 4 is the lowering of the deposition rate. Since oxygen is volatile, oxygen species have sticking coefficient less than unity, reducing the deposition rate of the film. Rates were shown (Table 4.1) to dramatically decrease when adding oxygen. Without oxygen the rate was approximately 2.0 $\mu\text{m/hr}$, but when adding oxygen (30:1 and 15:1, Ar:O₂) the rate decrease to 0.30 $\mu\text{m/hr}$. This also leads to oxygen substoichiometry if the deposition is not compensated with oxygen. Additionally, optical properties (color and transparency) of the films could be altered with the incorporation of varying oxygen concentrations.

3.2.7 Sputtering Target

The sputtering target material used in this study was 99.99% pure zirconia doped with 3mol% yttria (SCI Engineering, Columbus, OH). Final form of the target was machined from a sintered/hot iso-statically pressed (HIP) block and machined to a final size of 3in. diameter by 0.125in. thick. The target was then silver-solder bonded to a 3in. diameter copper backing plate with a 1in. magnetic keeper to secure the target to the sputtering gun. Targets were subjected to an initial burn-in for approximately 15-20 hours at 50W in an argon atmosphere. In order to achieve specific crystal structures, the amount of the dopant (yttria in this case) is important. The 3mol% yttria doped target was selected based on its composition, which generates the highest percentage of

tetragonal phase [9]. Based on bulk zirconia properties, a film with a high percentage of tetragonal would benefit from a $T \Rightarrow M$ phase transformation. In order to verify dopant/structure relationships, some films were deposited using a 8mol% yttria doped zirconia target. Figure 3.2 is a representative XRD diffraction pattern where only the stabilized cubic phase is present.

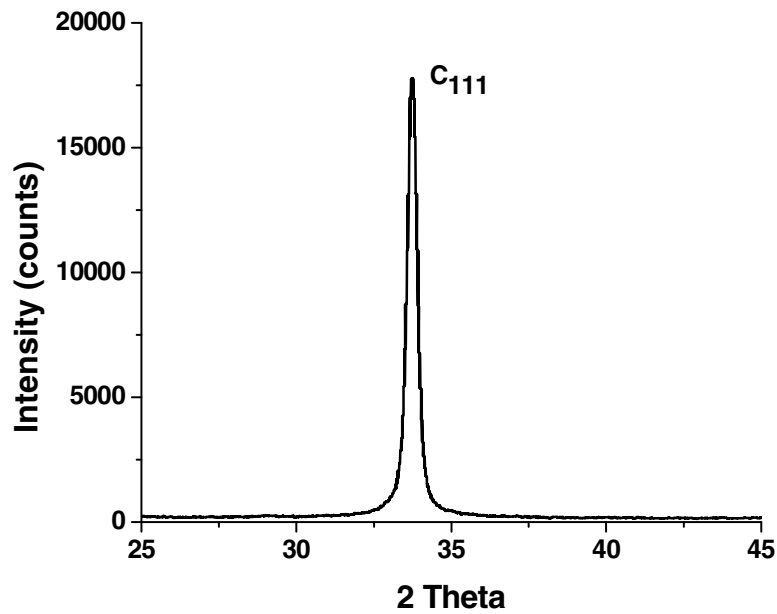


Figure 3.2: X-Ray diffraction pattern of sputter deposited 8mol% yttria-stabilized zirconia thin film.

3.3 Physical Characterization

Deposited thin films were characterized by various complimentary techniques to analyze material properties. Wafer bow measurements (WBM) provide measurement values of overall film stress. X-Ray diffraction (XRD) allows for phase identification and extent of crystallinity. A prism coupler, utilizing advanced optical waveguide techniques, is used to determine index of refraction and film thickness. Scanning

electron microscopy (SEM) offers high magnification image analysis of grain morphology and film/substrate interface. Transmission electron microscopy (TEM) provides direct high resolution imaging of microstructure and electron diffraction data with high spatial resolution.

3.3.1 Wafer Bow Measurement (WBM)

Thin-film stress measurements were performed on a Flexus (Tencor FLX-2320, Milpitas, CA) instrument. It accurately measured the changes in the radius of curvature of the substrate caused by the deposition of a stressed thin film on the substrate. The system contained two solid-state lasers: a Class IIIA laser with 4mW power at 670nm wavelength and a Class IIIB laser with 4mW power at 750nm wavelength. The laser interferometer was used to measure the curvature of a wafer, which is used in the calculation of the stress in the film deposited on the wafer. It is important to note that the sample must have a reflective surface for accurate measurements. A PC for measurements, data acquisition, and result calculations controlled the Flexus. Each sample was measured before deposition (initial bow) and after deposition for thin film stress calculations. The stress in the thin film was calculated from the radius of curvature of the substrate using the Stoney equation [1,10]:

$$\sigma_f = - (E_s \cdot t_s / 6(1 - \nu_s) t_f) \cdot (1 / R_a - 1 / R_b) \quad [\text{Eqn. 3.1}]$$

where $E_s/(1-\nu_s)$ is the biaxial modulus of the substrate (1.8 GPa), t_s and t_f are the thickness of the substrate and deposited film, and R_a and R_b are the substrate radius of curvature measured before and after film deposition.

3.3.2 X-Ray Diffraction (XRD)

XRD data scans were taken using a Bruker D5000 4-circle diffractometer (Bruker AXS, Karlsruhe, Germany). It was fitted with a HighStar area detector and controlled by GADDS v3.330 software. The system used a 0.8mm collimated Cu K α x-ray beam for measurements. The equipment allowed for a 2-D map of collected diffracted intensity, where the horizontal axis is the 2 θ Bragg angle, and the vertical direction is out of plane tilt denoted by χ . By integrating counts over the χ direction, θ -2 θ plots are generated. Analysis of the θ -2 θ plots gives the interplanar spacing, which when compared to compiled powder XRD data allowed for phase identification [11]. The volumetric amount of monoclinic phase to tetragonal phase was calculated using the following equation:

$$V_M = 2.379 I_{M(111)} / (2.379 I_{M(111)} + I_{T(111)}) \quad [\text{Eqn. 3.2}]$$

where $I_{M(111)}$ and $I_{T(111)}$ are the integrated intensities of the M and T (111) peaks in each x-ray pattern [12]. The constant 2.379 is a correction coefficient derived from structure factor calculations of zirconia monoclinic and tetragonal ion positions and pattern fitting to determine theoretical $I_{(hkl)}$ diffraction lines [13].

3.3.3 Prism Coupler

The prism coupler (Model 2010 Prism Coupler, Metricon, Penninton, NJ) utilized advanced optical wave-guiding techniques to rapidly and accurately measure both the thickness and the refractive index/birefringence. For measurement, the sample was brought into contact with the base of a prism (1.80-2.65) via a pneumatically operated coupling head, creating a small air gap between the prism and film. A laser beam was directed towards the base of the prism and is normally totally reflected at the prism base

onto a photo-detector. At specific discrete angles of the incident angle θ , called mode angles, photons can tunnel across the air gap into the film and enter into a guided optical propagation mode, causing a sharp drop in the intensity of light reaching the detector. For a rough approximation, the angular location of the first mode determined film index, while the angular difference between the modes determined the thickness, allowing thickness and index to be measured completely independently. Measurements were made using a computer-driven rotary table that varies the incident angle θ , and locates each of the film propagation modes. As soon as two of the mode angles were found, film thickness and index can be calculated. The entire measurement process was fully automated and requires approximately twenty seconds. The number of modes supported by a film of given index increased with film thickness. For most film/substrate combinations, a thickness of 1000-2000 Å is required to support the first mode, while films in the one-micron range can support as many as four or five modes. If the film is thick enough to support two or more propagation modes (typically 3000- 4800 Å), the Model 2010 calculates thickness and index for each pair of modes, and displays the average and standard deviation of these multiple estimates. Here parameters were selected based on known index of refraction values of zirconia, 1.50 – 2.50. The standard deviation calculation, unique to the prism coupling technique, was an indication of measurement self-consistency and a powerful means of confirming the validity of the measurement.

3.3.4 Scanning Electron Microscopy

In scanning electron microscopy (SEM) an electron beam is focused into a small probe and rastered across the surface of a specimen. Interactions with the sample result

in the emission of electrons or photons as the electrons penetrate the surface. These emitted particles can be collected with the appropriate detector to yield valuable information about the material.

The instrument used in this study was a Hitachi S-4700 field emission SEM (FE-SEM) (Hitachi, Ltd., Tokyo, Japan). The system's electron source was a cold field emission gun with a stated resolution of 1.5 nm at 15 kV, 12 mm working distance and 2.5 nm at 1 kV, 2.5 mm working distance. Magnification ranged from 30X to 500,000X. Sample stage has a tilt capability of 45° at 12 mm working distance. To reduce charging effects when imaging, the samples were pre-coated with a thin layer of gold-palladium (Au-Pd) using a small desktop sputter coater (Desk II, Denton Vacuum, Moorestown, NJ).

The SEM also equipped with Energy Dispersive X-ray Spectroscopy (EDS) and Genesis microanalysis software (EDAX Ametek, Mahwah, NJ). EDS is an analytical method where an electron or photon beam is aimed down into the sample to be characterized. Initially, an atom within the sample contains ground state or unexcited electrons situated in concentric shells around the nucleus. The incident beam excites an electron in an inner shell, prompting its ejection and resulting in the formation of an electron hole within the atom's electronic structure. An electron from an outer, higher-energy shell then fills the hole, and the excess energy of that electron is released in the form of an x-ray. The release of x-rays creates spectral lines that are highly specific to individual elements; thus, the x-ray emission data can be analyzed to characterize the sample in question.

3.3.5 Transmission Electron Microscopy (TEM)

Cross-sectional specimens were made using focus ion beam (FIB) processing. This service was provided by Materials Analytical Services (Material Analytical Services, Inc., Raleigh, NC). The FIB (FEI200, FEI Comp., Hillsboro, OR) produces a beam of gallium (Ga) ions, from a liquid gallium metal ion source, which was accelerated to an energy of 20-30 keV. The beam was then focused onto the sample by electrostatic lenses to a sub-micron spot size (<10 nm). By controlling the location, beam size and current density of the ion beam, material can be selectively removed from sub-micron areas. Once the sample has been thinned to ~ 100 nm membrane of material, the sample was then transferred to a standard (Mo) TEM grid.

TEM samples were imaged by a Topcon 002B 200 kV TEM (Topcon Corp., Tokyo, Japan) and a JEOL JEM 2010F-FastTEM (JEOL LTD., Tokyo, Japan) with a Gatan (Gatan, Inc., Pleasanton, CA) energy filtering digital imaging system (GIF). The Topcon TEM was better suited for imaging and diffraction of microstructures at intermediate magnification. The JEOL TEM had higher resolution (point resolution of 0.23 nm and lattice resolution of 0.10 nm) and the digital imaging allowed for high resolution (HRTEM) of planar spacing and lattice fringes [14]. For in depth analysis of phase transformation and lattice determination, the JEOL TEM was better suited.

HRTEM and ImageJ (v1.37) fast Fourier Transform (FFT) diffractograms were used for lattice determination and planar spacing [15]. This technique was also used in determining areas of phase transformation within specific thin films [16].

3.3.6 Finite Element Analysis (FEA)

The finite element analysis including simple probabilistic studies that allowed for the evaluation of the relative impact of various design parameters such as the thickness of the grains, the grain diameter, and the mechanical properties of the material was carried out using the ANSYS 10.0 finite element analysis package (ANSYS Inc., Canonsburg, PA). The primary advantage of computational modeling was basic visualization of the stress distribution within films, in terms of either continuum layers of film deposited or more locally within individual grains in a film that allowed the prediction of local stress induced changes in phase which in turn affect the mechanical properties and crack retarding effects of the thin film.

3.4 Experimental Summary

The processing methodology of PVD thin films outlined in this chapter allows for YSZ deposition on varying substrates. YSZ thin films are sputter-deposited using specialized deposition equipment and parameters allowing for a wide variance of YSZ thin film material properties. Physical characterization techniques are outlined so that process-structure-property relationships can be developed.

3.5 References

1. Ohring M., *The Materials Science of Thin Films*, (Academic Press, London, 1992).
2. Vossen J.L., "Control of film properties by rf-sputtering techniques", *J. Vac. Sci. Technol.* **8** (5), S12-S30 (1971).
3. Cheng Y.H., Tay B.K., Lau S.P., Shi X., and Tan H.S., "Influence of substrate bias on the microstructure and internal stress in Cu films deposited by filtered cathodic vacuum arc", *J. Vac. Sci. Technol. A* **19**(5), 2102-2108 (2001).
4. Misra A. and Nastasi M., "Limits of residual stress in Cr films sputter deposited on biased substrates", *Appl. Phys. Lett.*, **75** (20), 3123-3125 (1999).
5. Thornton J.A., "Influence of apparatus geometry and deposition conditions on the structure and topography of thick sputtered coating", *J. Vac. Sci. Technol.* **11**, 666-670 (1974).
6. Itoh, T., *Ion Beam Assisted Film Growth*, (Elsevier, Amsterdam, 1989).
7. Hakansson G., Sundgren J.E., McIntyre D., Greene J.E., and Munz W.D., "Microstructure and physical-properties of polycrystalline metastable Ti_{0.5}Al_{0.5}N alloys grown by DC magnetron sputter deposition" *Thin Solid Films* **153**, 55-65 (1987).
8. Thornton J.A. and Hoffman D.W., "The influence of discharge current on the intrinsic stress in Mo films deposited using cylindrical and planar magnetron sputtering sources". *J. Vac. Sci. Technol. A* **3** (3), 576-579 (1985).
9. D.W. Hoffman, "Perspective on stresses in magnetron-sputtered thin films", *J. Vac. Sci. Technol. A* **12**, 953-961 (1994).
10. Stoney G.G., "The tension of metallic films deposited by electrolysis", *Proc. R. Soc.* **9**, 172-179 (1909).
11. Cullity B.D., "Elements of X-Ray Diffraction". Addison-Wesley, Reading, PA (1978).
12. Wang Y.H. and Li X.P., "Phase structure characteristics of r.f. reactively sputtered zirconia thin film", *Thin Solid Films* **250**, 132-134 (1994).
13. R. Fillit, P. Homerin, J. Schafer, H. Bruyas, and F. Thevenot, "Quantative XRD analysis of zirconia-toughened alumina ceramics", *J. Mat. Sci.* **22**, 3566-3570 (1987).
14. Bendersky L.A. and Gayle F.W., "Electron diffraction using transmission electron microscopy. *J. Res. Natl. Inst. Technol.*, **106**, 997-1012 (2001).

15. Rasband, W.S., ImageJ, U. S. National Institutes of Health, Bethesda, Maryland, USA, <http://rsb.info.nih.gov/ij/>, 1997-2006.
16. Edington J.W., *Practical Electron Microscopy in Materials Science*, (MacMillan Philips Technical Library, Eindhoven, 1975).

Chapter 4

Processing-Structure-Property Relationships: Sputter-deposited 3mol% YSZ Thin Films

In order to study specific film structures and properties, it was important to develop a process space of varying deposition parameters to modify such material characteristics. This section will look at specific material properties as a function of deposition parameters.

Several groups have investigated deposition of YSZ thin films using r.f. magnetron sputtering. Research has shown that using a zirconia target doped with 3mol% yttria produces varying percentages of tetragonal and monoclinic phases [1, 2]. Increasing the dopant percentage (from 3 to 8%) of the target has been shown to produce a film with predominately cubic phase [3, 4]. Depending on the percentage of yttria in the target, deposition parameters (pressure, power density, oxygen partial pressure, temperature) will dictate the crystal structure of the film.

Depending on deposition parameters, the elemental composition of sputter-deposited YSZ thin films can be altered. Wang *et al* investigated varying oxygen partial pressure during deposition. It was reported that increasing oxygen flow from 0 to 13% produced variations in the stoichiometry of the films. The O:Zr ratio in the deposited films varied from 1.80 to 2.24 [5]. Another report stated that variation in the O:Zr ratio appeared to be dependent on the amount of oxygen introduced into the sputtering gas [1].

Here it was stated that recombination of atomic oxygen to molecular oxygen in the plasma results in sub-stoichiometric films (oxygen deficient) when only sputtering with argon.

Since sputtered films are generally classified as having a columnar grain structure, there is usually porosity within the films. This characteristic is affected by specific deposition parameters. A film with a high level of porosity is vulnerable to absorption of water vapor [3, 6], especially when exposed to ambient conditions. Water absorption can greatly impact the behavior of the deposited film, often in a deleterious manner (stress corrosion for example) [7]. One interesting phenomenon that has been reported is a dipole-dipole interaction of water molecules that have been absorbed/adsorbed in the porous structure of the film, producing an increase in compressive stress in the deposited film [8].

As previously stated, sputtered thin films have been shown to improve the mechanical behavior of brittle substrates. Coupling this characteristic with the unique properties of YSZ might prove to be beneficial in a broad array of applications. The purpose of this section is to investigate the effects of variation in deposition parameters (working pressure, temperature, and oxygen partial pressure) on film stress, crystal structure, and optical properties of deposited YSZ thin films. In addition, films were subjected to ambient environments to investigate possible film degradation.

4.1 Deposition of YSZ Thin Films

Chapter 3 describes the sputter deposition and radio frequency magnetron system used throughout this entire study. A systematic parameter space was derived for films

deposited of this part of the study using the design of experiments surface method model (DOE PRO XL, Air Academy Assoc. LLC and Digital Computations Inc., Colorado Springs, CO.). This model evaluated variation of three deposition parameters in a cube configuration (Figure 4.1). All parameters defined by the corners and faces of the cube were performed, and the center point was performed three separate times, as a check of repeatability. Deposition parameters altered included; working pressure (5, 15, 25 mTorr), substrate temperature (25, 150, 300°C), and oxygen flow rate (0, 3, 6 sccm). Oxygen input flow rate variation resulted in approximate Ar:O₂ ratios of 100:0, 30:1, and 15:1. Sputtering times varied (1-20 hr) depending on desired thickness and parameter space inputs.

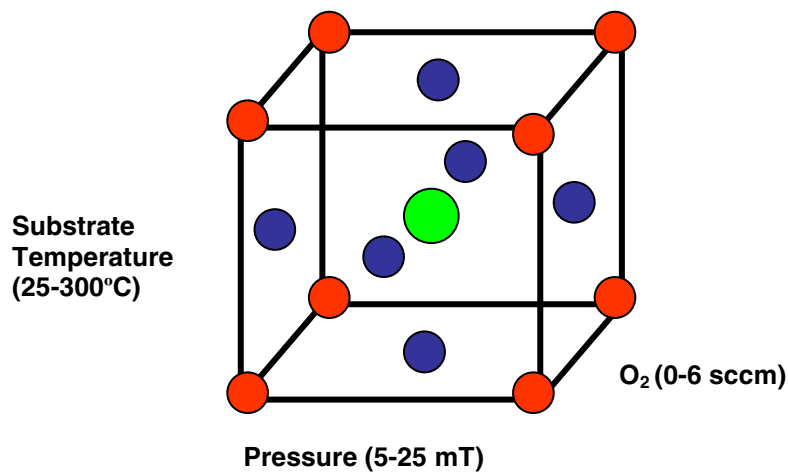


Figure 4.1: Process cube describing deposition parameters (function of substrate temperature, working pressure, and background oxygen). Center of process cube was performed three separate depositions.

4.2 Physical Characterization

4.2.1 Film Stress

Film stresses were measured using a wafer bow measurement system (specific details are covered in section 3.3.1). Each silicon wafer was measured before deposition

and then re-measured immediately upon removal from the vacuum chamber, post deposition. This allowed the measurement system to determine bow offset caused by the deposition of the film. Films that were analyzed had a thickness of approximately 5 μm and were deposited on the roughened side of the silicon wafer ($R_a=0.4\mu\text{m}$) to enhance film adhesion to the substrate and simulate end application surface roughness.

No matter the deposition technique, thin films are generally found to be under a state of stress; these stresses originate from thermal and intrinsic components. Thermal stresses (σ_{th}) result from the mismatch between coefficients of thermal expansion (α) for the substrate and thin film materials. If a mismatch exists, any additional heating or cooling would cause stress states to be altered. The intrinsic stresses (σ_i) are primarily due to incorporation of impurities, flaw accumulation during growth, and structural reorganization [6, 10]. For the YSZ and silicon system, a one-dimensional approximation was used to calculate the thermal stress [9]:

$$\sigma_{\text{th}} = E_f(1 - \nu_f)^{-1}(\alpha_f - \alpha_s)(T_a - T_s) \quad [\text{Eqn. 4.1}]$$

where the subscripts f and s refers respectively to the film and substrate; E, ν , α , and T are Young's modulus, Poisson ratio, coefficient of thermal expansion, and temperature. The coefficient of thermal expansion values for silicon and YSZ were found to be $3.0 \times 10^{-6} \text{ C}^{-1}$ and $10 \times 10^{-6} \text{ C}^{-1}$.

Film stress measurements showed that the majority of deposited YSZ films displayed compressive stress. The magnitude of calculated compressive stresses varied from 27 to 193 MPa (Table 4.1). Sputtered films are typically under a compressive stress, primarily due to incorporation of impurities, flaw accumulation during growth, and structural reorganization [6, 10].

Process Cube			Bow Measurements (μm)			Calculated Stress (MPa)		Intrinsic Stress (MPa)		Volume % Monoclinic	Deposition Rate
Pressure (mTorr)	Temp ($^{\circ}\text{C}$)	BG - O (sccm)	W/out Film	With Film (t=0)	With Film (t=720 hr.)	t=0	t=720 hr.	t=0	t=720 hr.	Post Exposure	$\mu\text{m/hr.}$
5	25	0	0.9	96.3	133.5	-181	-256	-181	-256	0.028	2.04
* 5	25	6	2.7	73.9	80.2	-164	-178	-164	-178	0.720	0.22
* 5	150	3	4.4	74.7	79	-175	-177	-350	-352	0.713	0.46
5	300	0	1.1	91.8	117.2	-148	-198	-533	-583	0.056	2.00
5	300	6	-0.3	54.4	87.1	-119	-196	-504	-571	0.711	0.25
15	25	3	0.9	112.5	141.3	-193	-286	-193	-286	0.571	0.22
15	150	0	0.7	-41.3	-25	86	53	-89	-122	0	2.05
15	150	3	3.1	51.5	96.8	-96	-181	-271	-356	0.564	0.22
15	150	3	-1.8	35.9	70.2	-62	-126	-237	-301	0.574	0.28
15	150	3	-7	43.8	84.7	-71	-155	-246	-330	0.531	0.28
15	150	6	-2.2	45.2	72.5	-87	-142	-262	-317	0.540	0.25
15	300	3	-11	35.3	66	-47	-110	-432	-495	0.506	0.30
25	25	0	-1.2	-18.6	-5.3	38	13	38	13	0	2.60
25	25	6	0.6	73.3	106.6	-130	-193	-130	-193	0.352	0.25
25	150	3	-0.8	25.4	62.2	-42	-116	-217	-291	0.393	0.31
25	300	0	-0.7	-54.5	-40.1	111	86	-274	-299	0	1.82
25	300	6	4	16.1	43.1	-27	-79	-412	-464	0.259	0.27

* Film de-bonded from substrate

Table 4.1: Wafer bow measurements and calculated film stress for the deposition parameter space: (-) designates compressive stress. Calculated values for intrinsic stresses and volume % monoclinic are also shown.

Figure 4.2 displays contour plots of the relationship between film stress and deposition parameters. Each deposition temperature is plotted as a function of working pressure and background oxygen. This data shows that for the presented deposition process space that film stress is tunable. Also, a transition from tensile to compressive film stress is observed at each substrate temperature. Deposition parameters were shown to have a dramatic effect on the magnitude and direction of measured film stress values. At low working pressures, with oxygen incorporated in the sputtering gas, films exhibited compressive stresses varying in magnitude. This is due to sputtering atoms and backscattered species having sufficient energy to reach the surface of the substrate with a low incident angle. The resulting interactions enhance diffusion of surface atoms and can produce recoil implantation into the growing film, causing the film to display compressive stress [6].

With the absence of oxygen in the background and at high total pressures, films were shown to have a tensile stress. Higher working pressures increases the scattering of neutrals within the plasma, increasing the energy of atoms impacting the surface of the growing film, and effectively reducing the magnitude of compressive stress. Also, low oxygen content will increase the volume fraction of vacancies and voids created in the growing film. The formation of voids allows grains within the film to relax, producing a tensile film stress [11].

After 720 hr. exposure to ambient conditions (25°C, 75 % relative humidity), wafer bow measurements were again made. Calculated stress values increased in the compressive direction (Table 4.1). In order to evaluate this phenomenon, stress was measured incrementally on select specimens (1 per Ar/O₂ gas ratio) as shown in Figure

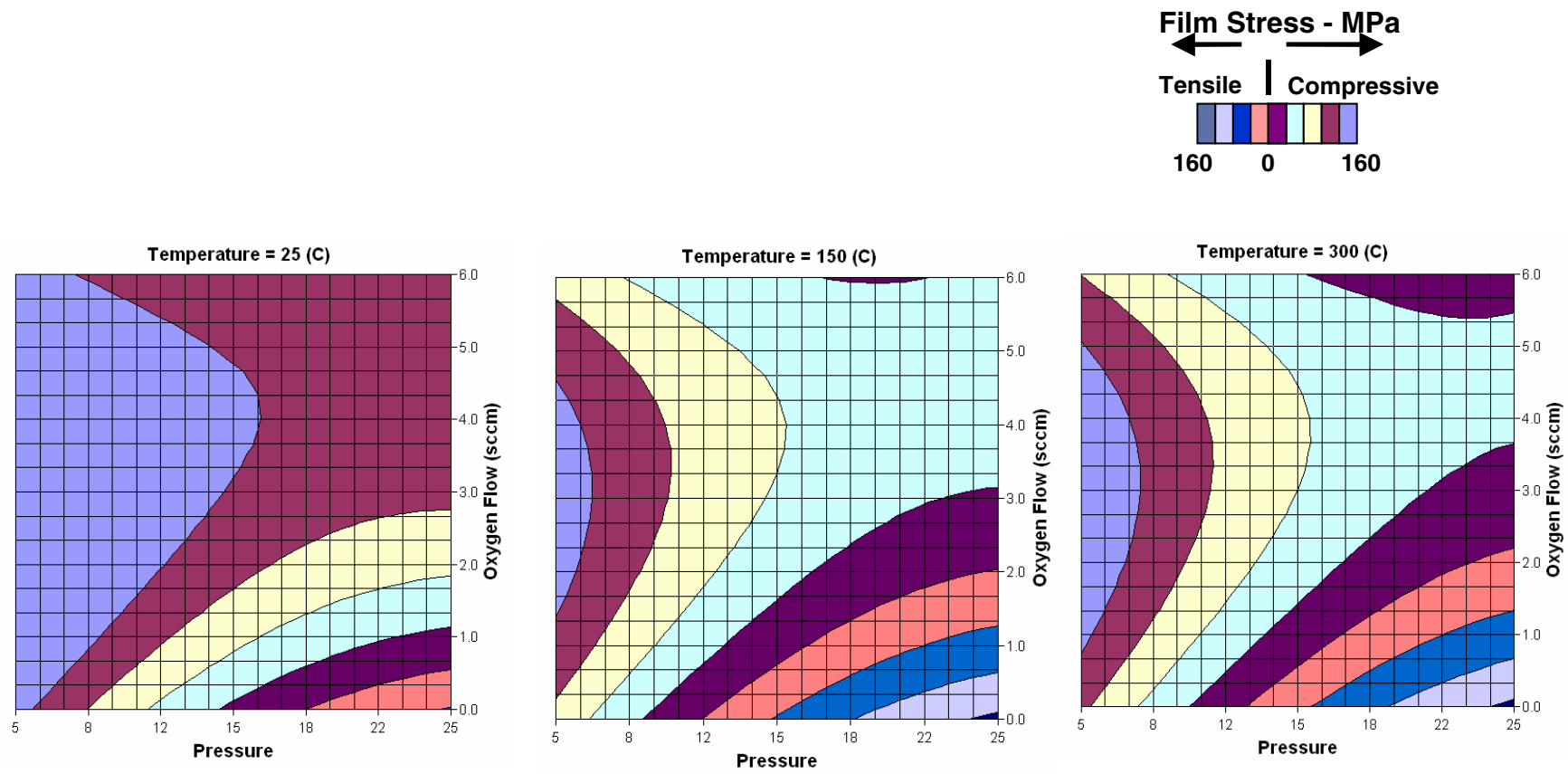


Figure 4.2: Contour plots of the relationship of film stress and deposition parameters.

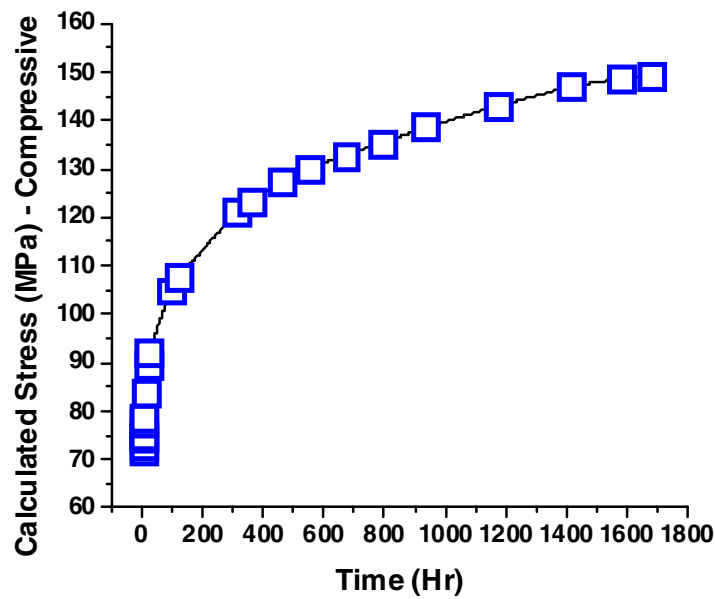


Figure 4.3: Calculated stress measurement for YSZ film deposited without an applied bias.

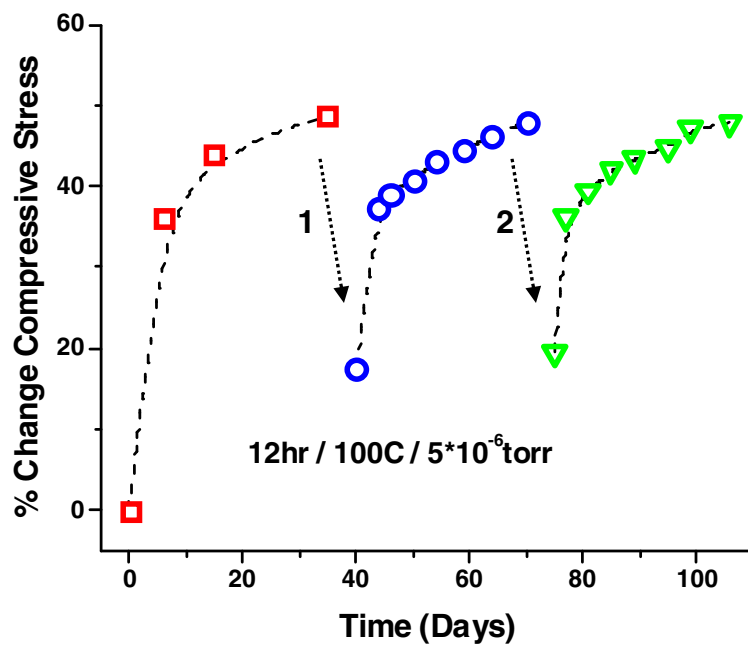


Figure 4.4: Percent change in measured stress values as a function of several thermal treatments. Stress was measured at set time intervals immediately after deposition and thermal treatments (12 hr / 100° C / 5×10^{-6} torr).

4.3. A model of water absorption into the defect structure of films is the proposed mechanism of this increase. It has been reported that water molecules can penetrate the defect structure of films and the resulting dipole-dipole interaction of molecules can produce a compressive stress. To verify this, a random specimen was subjected to a thermal treatment (100°C) under vacuum (5×10^{-6} torr) for a period of 12 hr. As shown in Figure 4.4, the film returns to near its original stress state. This thermal treatment should have removed most absorbed water vapor, but it is thought that some water molecules may have chemisorbed, reacting with exposed surface within the defects. This may be the reason the film stress of the examined specimen did not return to its as-deposited value. As the film is exposed to ambient conditions, compressive stress increases. The most significant increase was seen in the first 24 hr and the highest rate was within the first two hours of exposure (shown in Figure 4.5).

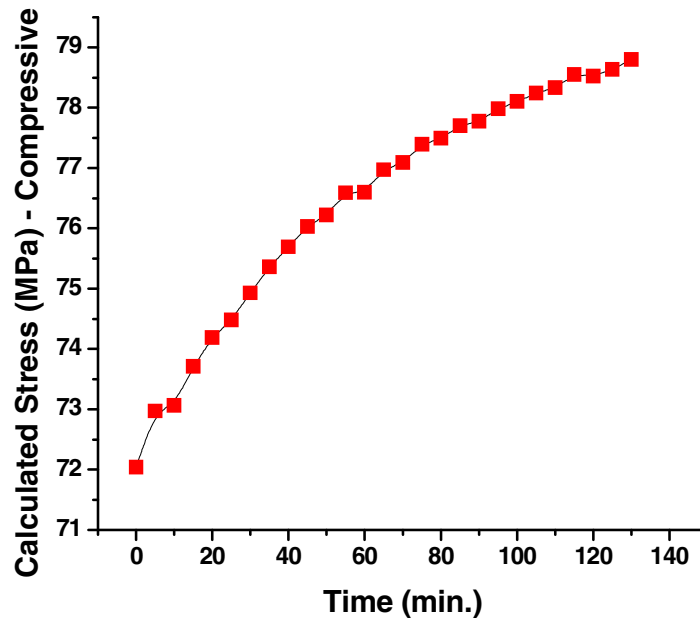


Figure 4.5: Calculated stress measurements for first 2hr of exposure to ambient conditions (25°C, 75% relative humidity).

To further support this model, analysis of the Thornton Diagram led to the conclusion that Zone I and Zone T can describe the films in this study (Figure 2.2) [11]. The lack of grain morphology variation is due to the temperature range examined in this study. The maximum deposition temperature used was 300°C, which is only about 10% of the melting temperature (T_M) of YSZ (~2700°C). Zone I is characterized as a porous structure that consists of tapered crystallites separated by voids, and Zone T is the transition structure of densely packed grains, typically columnar in shape [12]. Both of these structures can lead to absorption of water molecules into inter-granular defects in the film. Gilmer *et al.* confirmed zone variations as a function of temperature and pressure utilizing Monte Carlo simulations of competitive texture evolution [13].

4.2.2 Structural Analysis

SEM allowed for cross-sectional samples of deposited thin films to be visually analyzed and compared to the Thornton Diagram. Figures 4.6 – 4.14 display representative micrographs of 3mol% sputter-deposited YSZ thin films. The films show a columnar grain structure that is expected for the films grown at temperatures which are considerably lower than the YSZ melting temperature. Each figure shows varying magnifications of the films. This is to show the adhesion of the film/substrate construct, the structure of the film, and also a higher magnification to evaluate for inter-columnar porosity. SEM micrograph analysis showed that all films had apparent good adhesion on the polished and roughened side of the silicon wafers. At higher magnification, SEM analysis showed that all films exhibited some level of porosity, which is especially evident in between the columnar grains. Only two films were shown to buckle (spall-off) and delaminate from the substrate. Both were deposited at 5mT with oxygen introduced

into the background and it was determined that the intrinsic stress coupled with the film microstructure caused the film to fail. Figure 4.14 shows SEM micrographs of a film deposited at 5mT, 300°C and a Ar:O₂ ratio of 30:1. The cleaved surface shows an interrupted surface with lateral cracks perpendicular to film growth. The measured intrinsic stress was compressive (571 MPa) which might lead to delamination and/or film cracking. This structure is more than likely due to sputtering atoms and backscattered species having sufficient energy to reach the surface of the substrate with a low incident angle at the low pressures. This structure is similar to substrate bias films shown in Chapters 5 and 6. A subsequent model of *in-situ* stress-induced phase transformation and lateral defect generation is address later within Chapter 6.

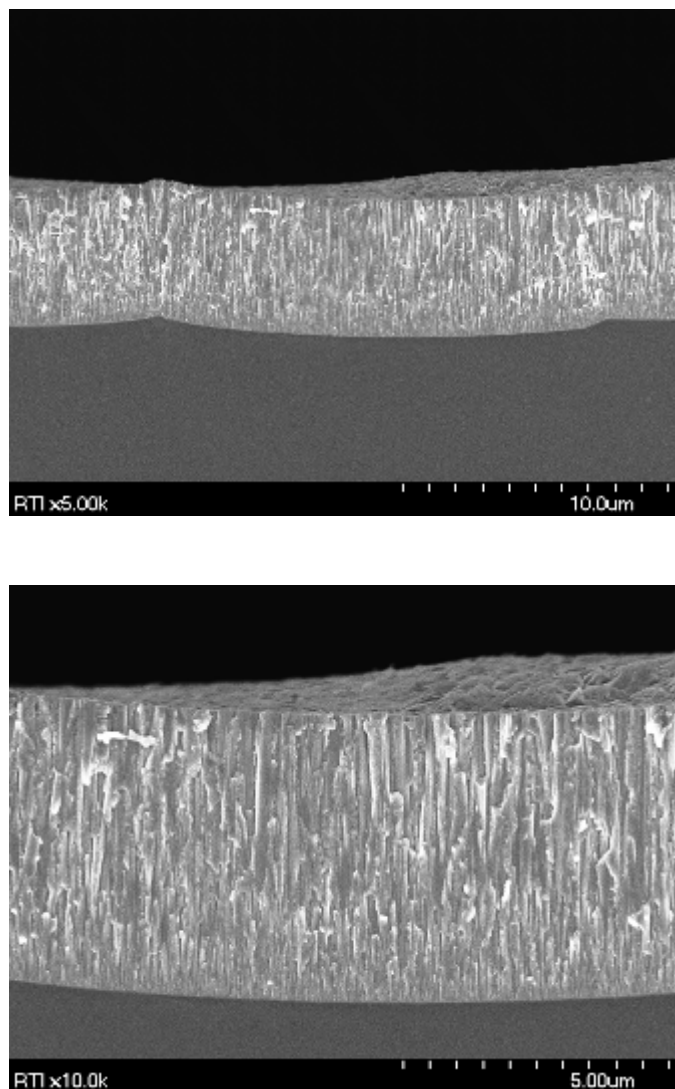


Figure 4.6: SEM micrographs for YSZ thin film with deposition parameters: working pressure - 5mT, substrate temperature 300°C, and only Argon sputtering gas.

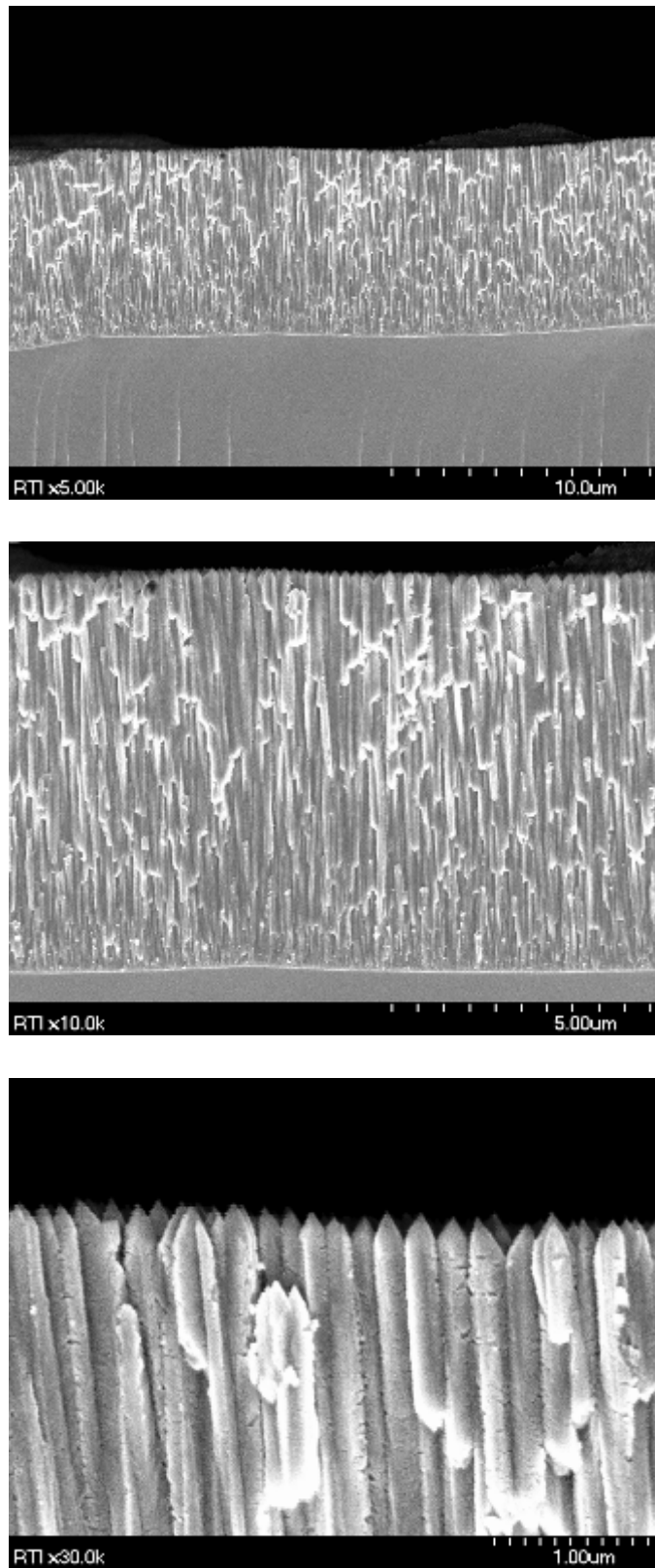


Figure 4.7: SEM micrographs for YSZ thin film with deposition parameters: working pressure - 15mT, substrate temperature 150°C, and Ar:O₂ ratio of 15:1.

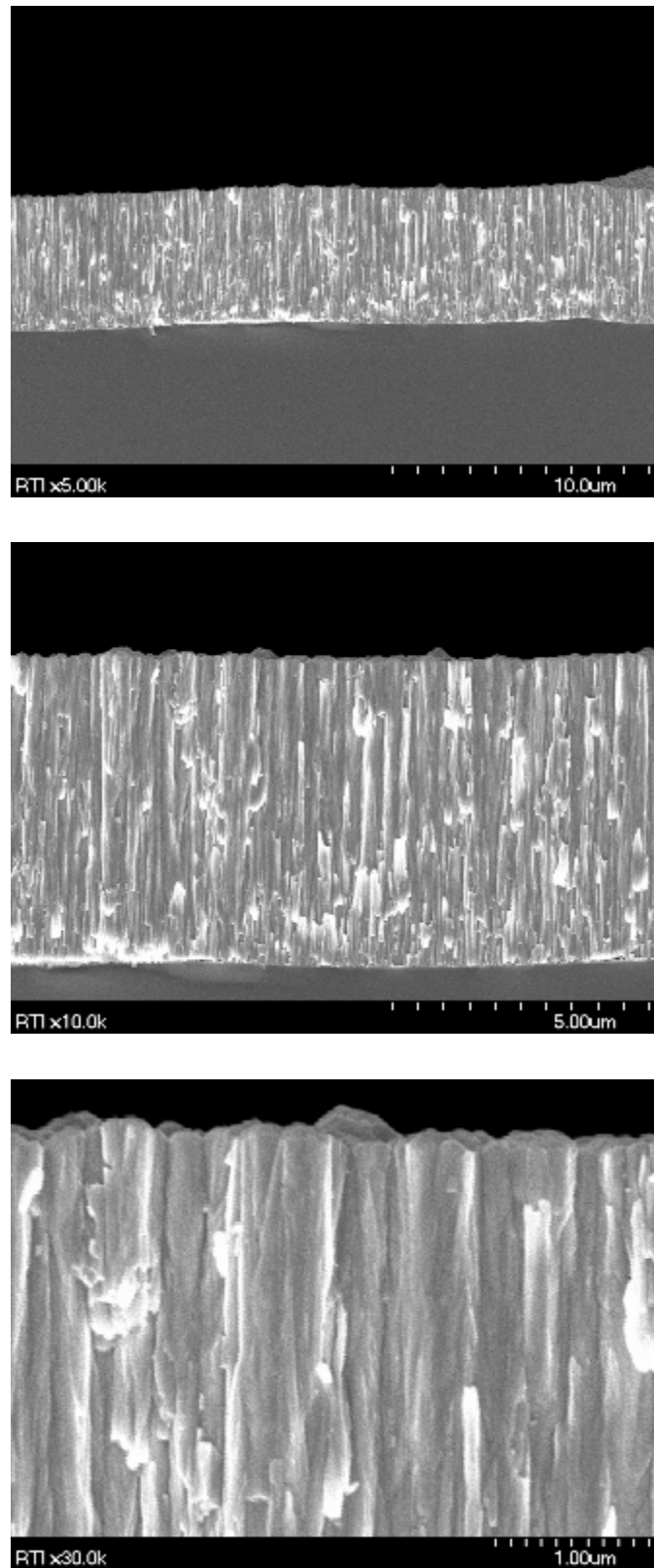


Figure 4.8: SEM micrographs for YSZ thin film with deposition parameters: working pressure - 25mT, substrate temperature 300°C, and Ar:O₂ ratio of 30:1.

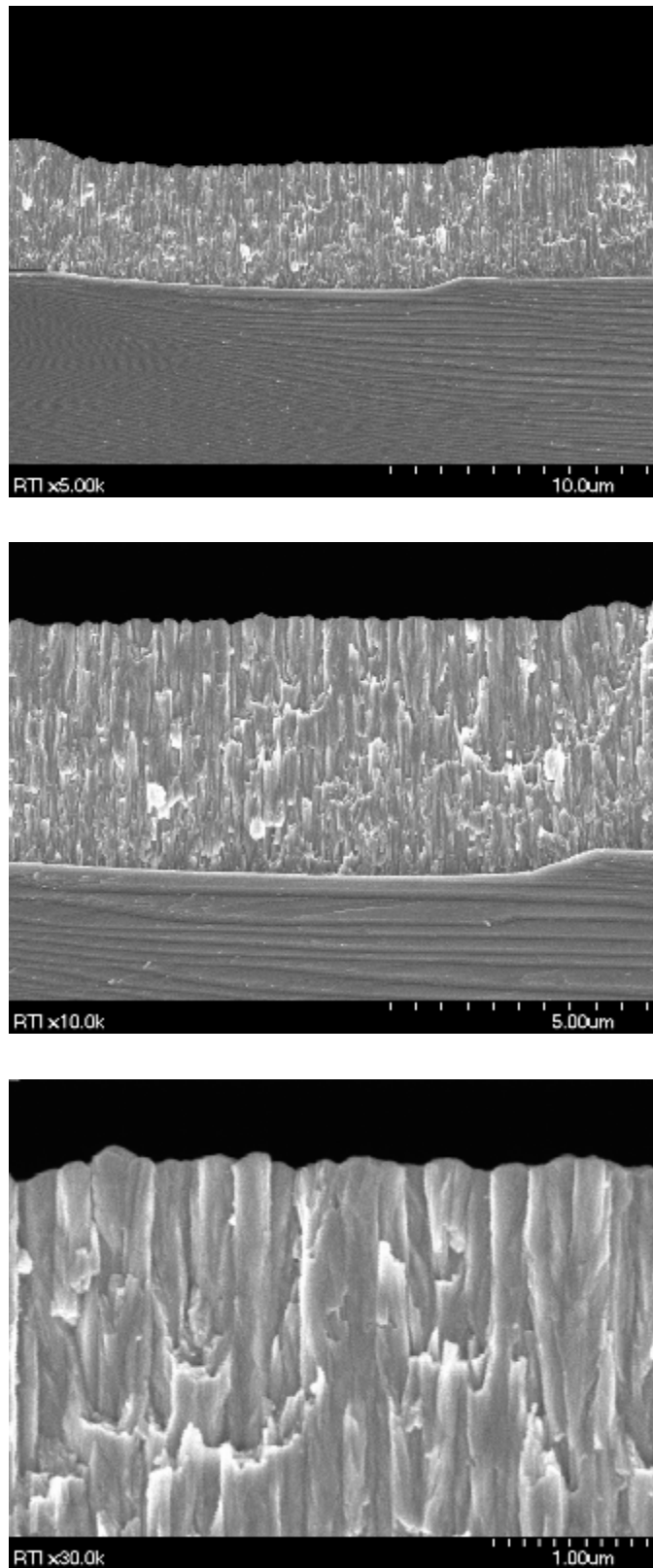


Figure 4.9: SEM micrographs for YSZ thin film with deposition parameters: working pressure - 25mT, substrate temperature 25°C, and Ar:O₂ ratio of 30:1.

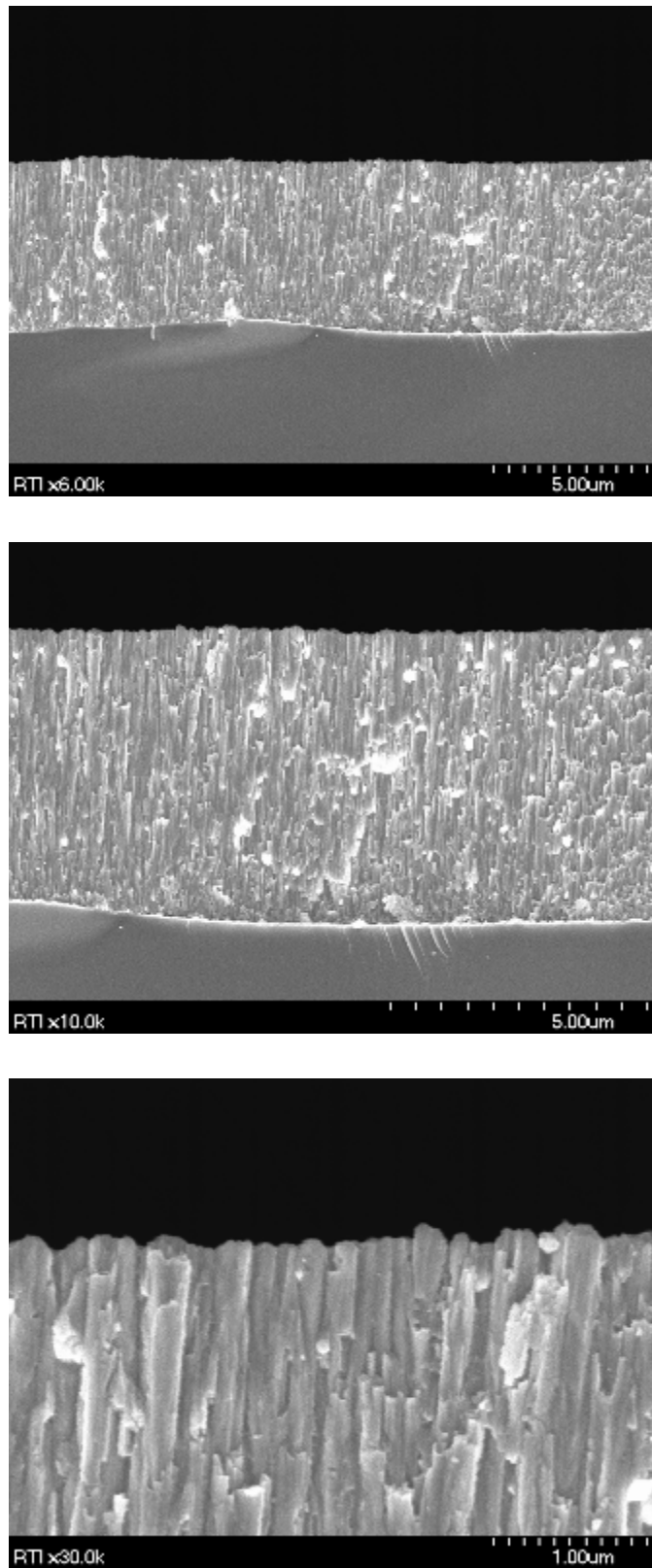


Figure 4.10: SEM micrographs for YSZ thin film with deposition parameters: working pressure - 5mT, substrate temperature 150°C, and Ar:O₂ ratio of 15:1.

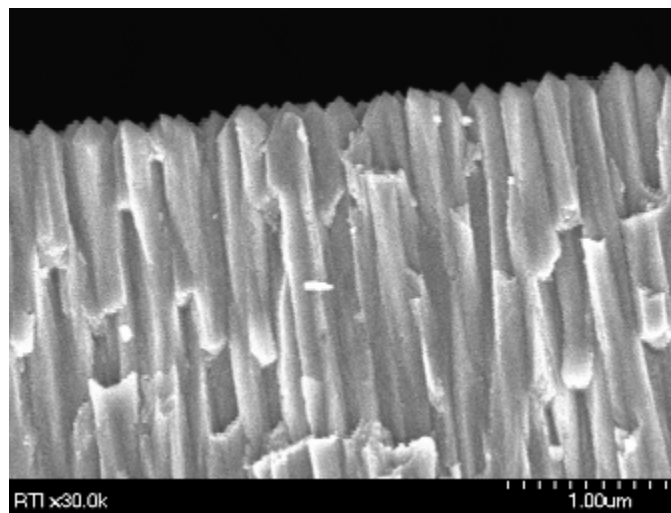
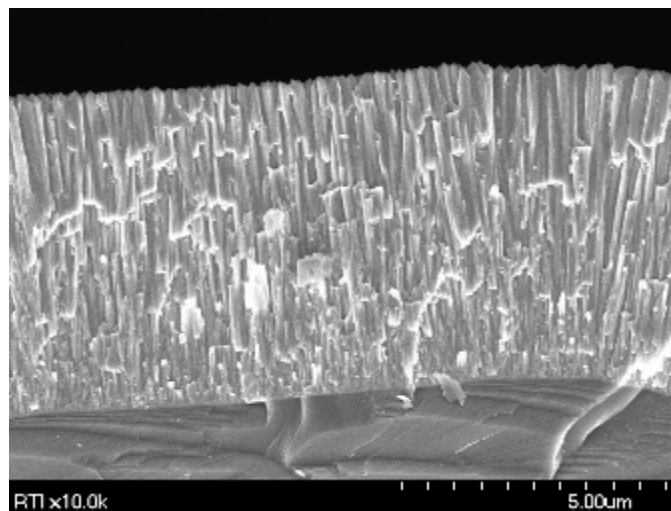
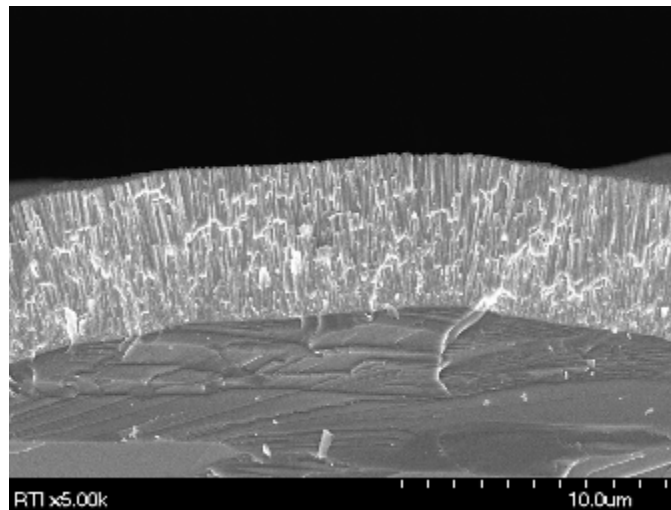


Figure 4.11: SEM micrographs for YSZ thin film with deposition parameters: working pressure - 15mT, substrate temperature 150°C, and only Argon sputtering gas.

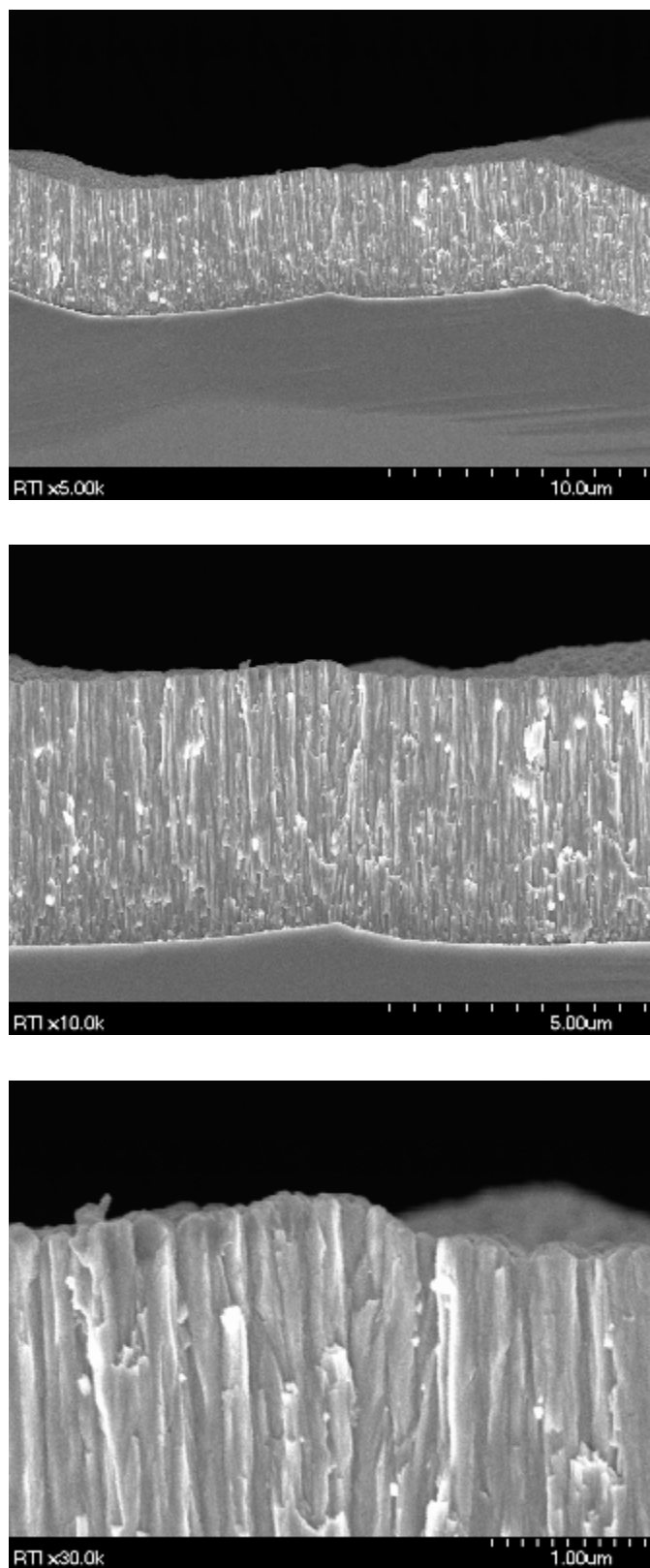


Figure 4.12: SEM micrographs for YSZ thin film with deposition parameters: working pressure - 25mT, substrate temperature 150°C, and Ar:O₂ ratio of 15:1.

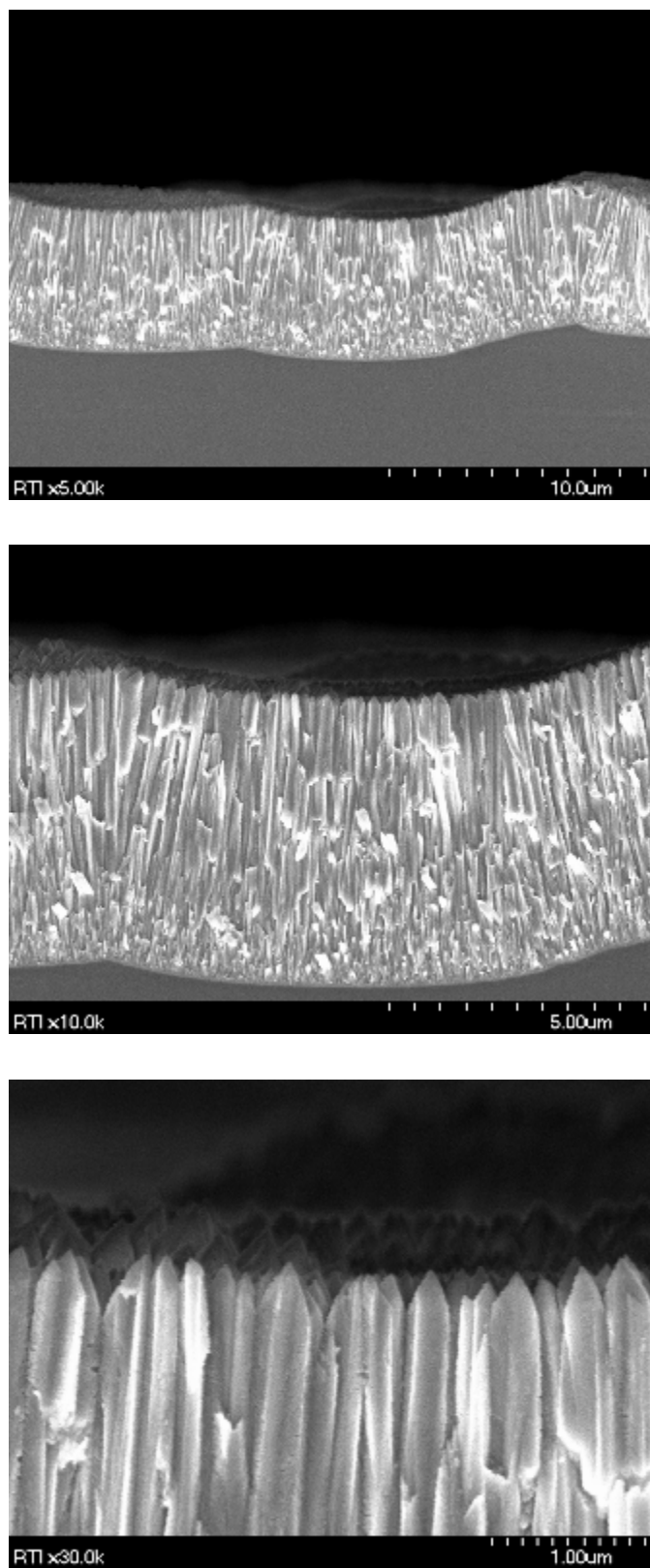


Figure 4.13: SEM micrographs for YSZ thin film with deposition parameters: working pressure - 15mT, substrate temperature 25°C, and only Argon sputtering gas.

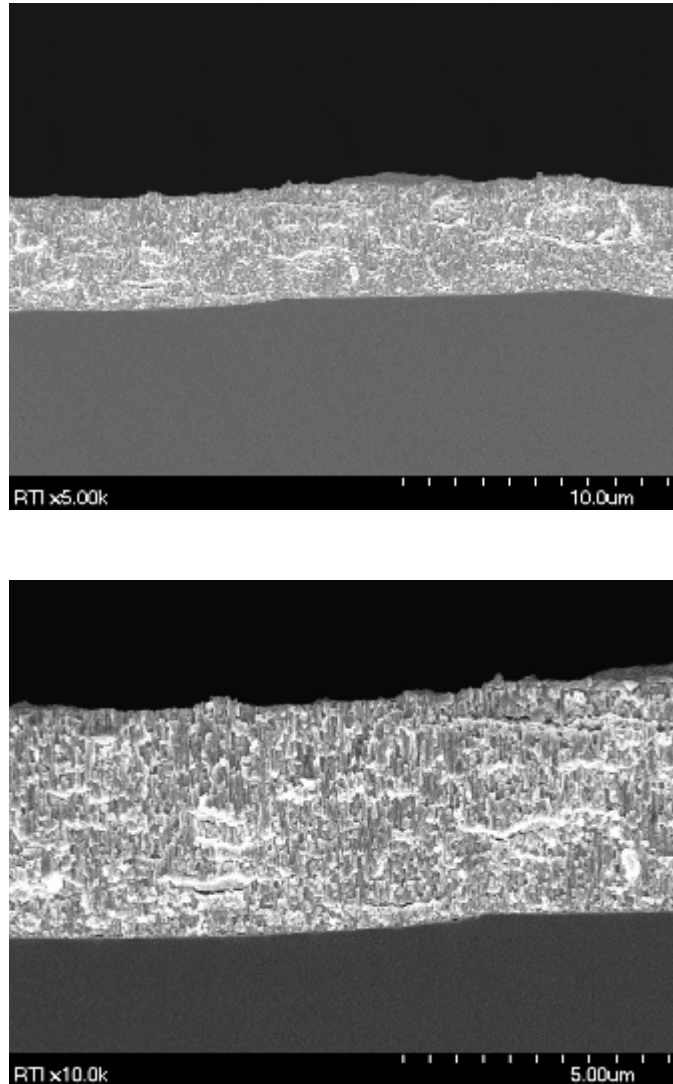


Figure 4.14: SEM micrographs for YSZ thin film with deposition parameters: working pressure - 5mT, substrate temperature 300°C, and Ar:O₂ ratio of 15:1.

4.2.3 Crystal Structure Analysis

XRD patterns identified two distinct groups in regard to phase structure, one with primarily 100% tetragonal phase and another with varying percentages of monoclinic and tetragonal phases (Figure 4.15). Films with no background oxygen were found to be predominantly tetragonal and have a sub-stoichiometric ratio of oxygen to zirconium [1]. Studies have theorized oxygen deficiency and the high number of defects present result in the tetragonal phase being thermodynamically favorable [1,8].

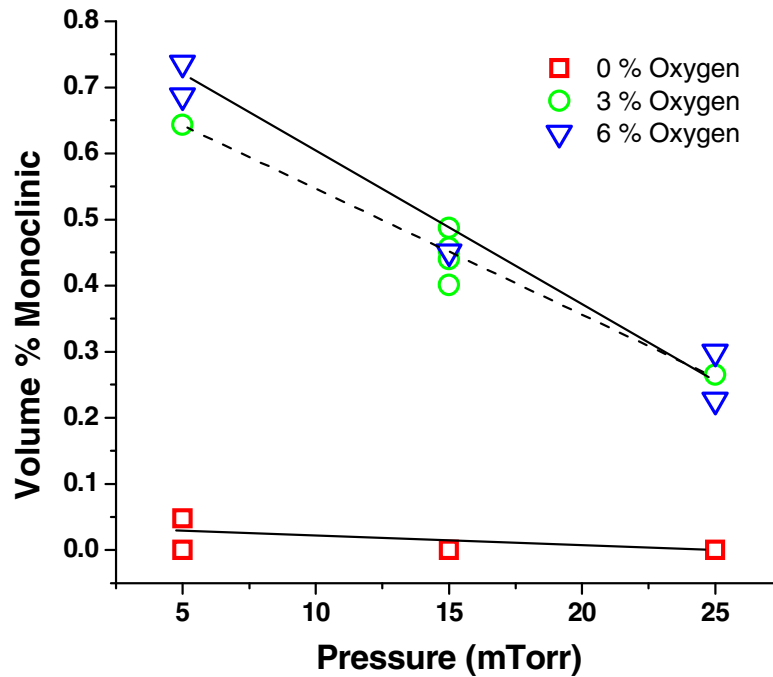


Figure 4.15: Effect of deposition parameters on the percentage of monoclinic phase formed. Depositions with no oxygen produced films ~100% tetragonal phase as oxygen flow increases, monoclinic phase becomes more prevalent with higher percentages produced at low working pressures.

With an increase in oxygen into the sputtering gas, films were shown to have both tetragonal and monoclinic phases. Monoclinic phase formation becomes favorable due to the stoichiometric O:Zr ratio and/or at lower deposition temperatures. It appears that

background pressure has a direct effect on the percentage of each phase. At low working pressures the percentage of monoclinic phase is at its highest, and this percentage decreases as working pressure is increased. At higher working pressures, collisions within the plasma cause an increase in neutral gas temperature, which allows the tetragonal phase to be more thermodynamically stable.

For films that had a mixture of two phases, stress values were lower in magnitude than for films with a lower percentage of monoclinic phase. The magnitude of stress increased compressively as the percentage of monoclinic phase increased. This is possibly due to the relative amounts of the two phases. An increase in the amount of monoclinic phase present, which has a larger unit cell (~ 4 vol. %), effectively increases the volume of the film [14]. Table 4.1 shows the data of intrinsic stresses within the films along with the calculated volume percent of monoclinic phase. It should be noted that the higher the intrinsic stress, the higher percentage of monoclinic phase present. A model for *in-situ* stress-induced phase transformation will be discussed later in Chapter 6.

Texturing was not investigated in this study, but preliminary analysis of the XRD data showed that the majority of films displayed a dominant <111> texture. Figure 4.16 displays representative XRD scans for films with predominant <111> texturing. However, this was not seen for columnar films deposited at low pressures and in pure argon plasma where a dominant <200> growth direction was observed (Figure 4.17). This is consistent with reports that low sputtering pressures yield a preferred texture along the <200> axis for YSZ thin films [15]. In addition, as pressure is increased, the intensity of the (200) peak decreases and the films are oriented in the <111> direction [16]. This c-axis texturing becomes important when examining tetragonal to monoclinic

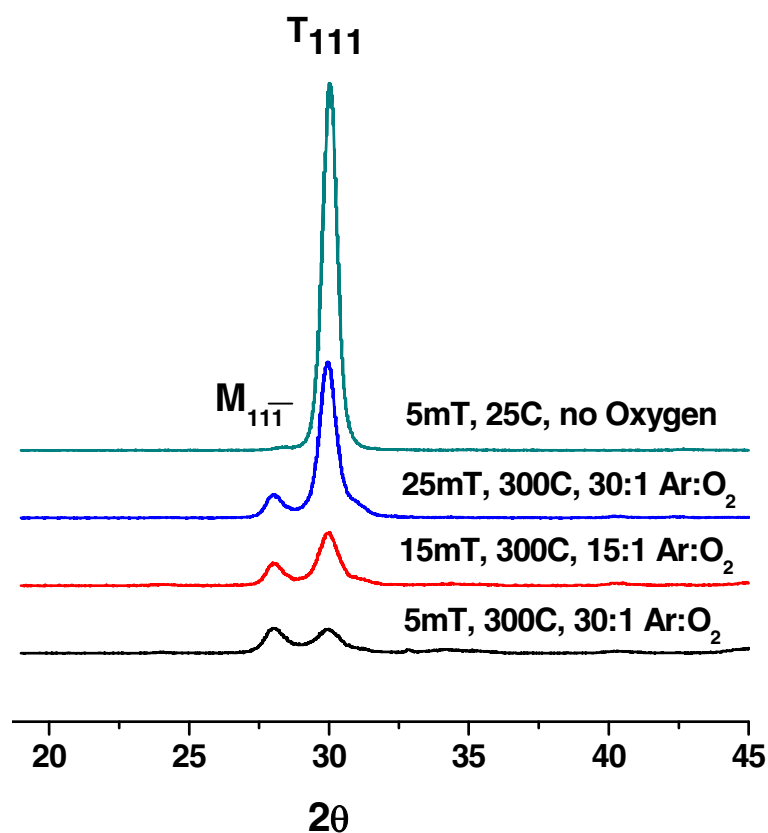


Figure 4.16: Representative XRD scans for YSZ thin films displaying a predominant <111> texture (deposition parameters are noted on the graph).

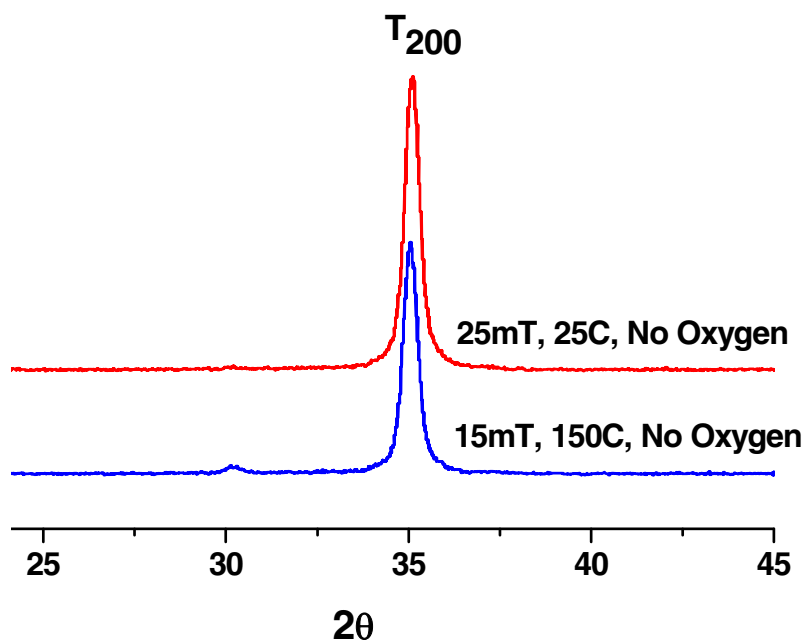


Figure 4.17: Representative XRD scans for YSZ thin films displaying a predominant <200> texture (deposition parameters are noted on the graph).

phase transformation, discussed later in Chapter 5 and 6. The $\langle 111 \rangle$ texturing suggests an orientation relationship between the tetragonal and monoclinic lattices is such that $(100)_M // (100)_T$ and $[001]_M // [001]_T$ [17].

4.2.4 Index of Refraction

Index of refraction data (Table 4.2) varied throughout the parameter space (ranging from 1.959 to 2.223). Films that were optically translucent or opaque, and were dark in color, had the highest index of refraction values. These films were deposited at low working pressures, and with no oxygen introduced in the sputtering gas. Since some films can be described as oxygen deficient and were deposited at low pressure, it is possible that free zirconium atoms form defect complexes in the growing film, either interstitially or at grain boundaries, causing the film to have a dark appearance. X-ray diffraction did not show the presence of phase separated zirconium supporting the conclusion that defect complexes are formed in sub-stoichiometric films. Within the same parameter space, it was seen that substrate temperature qualitatively decreased the level of opacity. Higher temperature may lead to a more favorable thermodynamic environment for zirconium atoms to be incorporated into the lattice. As working pressure increased, refractive index decreased, and films were optically clear.

As stated earlier, previous research has hypothesized that condensation and absorption of water molecules can take place in pores developed during the deposition process. By applying the rule of mixtures, the packing density (porosity density) can be calculated [9]:

$$n_m = n_s P + n_v (1-P) \quad [\text{Eqn. 4.2}]$$

where n_m is the measured index of refraction, n_s is the known index of refraction of the specific crystal phase structure, n_v is the index of refraction of the void constituent (1.00 for air and 1.35 for water), and P is the packing density (porosity) of the material. By analyzing the volumetric percentages of the crystal phases present in respective films, n_s was calculated using 2.16 for the tetragonal phase [18] and 2.24 for monoclinic phase [19]. The index of refraction of each film was measured immediately upon removal from vacuum and re-measured after exposure to ambient conditions. As shown in Figure 4.18, the packing density of each film was calculated. Films deposited at low working pressure have calculated packing densities close to 1. This coincides with a film that has a low defect density. At low pressure, sputtering yield is high, and particles impact the film surface with significant energy, increasing the mobility of sputtered adatoms. As

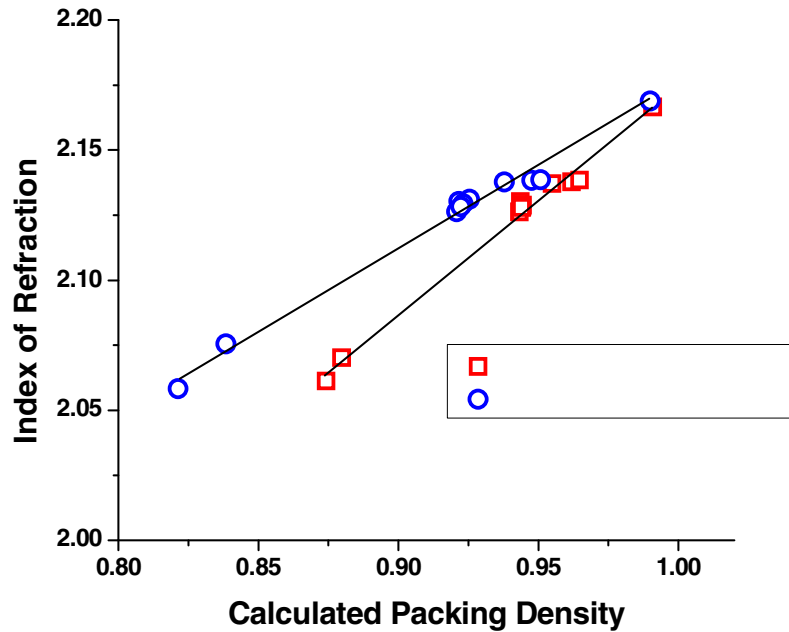


Figure 4.18: Packing density calculation (utilizing measured index of refraction).

pressure is increased, gas-phase collisions increase, and atoms arrive at the substrate with lower kinetic energy [9,11]. Therefore, sputtered atoms have less energy for surface diffusion and the resulting film will contain a higher porosity.

Pressure (mT)	Temp (C)	BG - O (sccm)	Index of Refraction	Index (t=720 hr.)	Color
* 5	22	0	n/a	n/a	Brown (metallic)
5	22	6	2.070	2.075	Clear
** 5	150	3	n/a	n/a	Clear (Whitish)
5	300	0	2.223	2.229	Tan
5	300	6	2.061	2.068	Clear (Whitish)
15	22	3	2.128	2.131	Clear
15	150	0	2.041	2.043	Clear
15	150	3	2.130	2.131	Clear
15	150	3	2.126	2.129	Clear
15	150	3	2.126	2.128	Clear
15	150	6	2.127	2.128	Clear
15	300	3	2.137	2.137	Clear (Whitish)
25	22	0	1.959	1.973	Clear
25	22	6	2.137	2.138	Clear
25	150	3	2.138	2.138	Clear
25	300	0	2.002	2.003	Clear (Whitish)
25	300	6	2.163	2.168	Clear

* Unable to obtain index of refraction measurement, ** Film de-bonded from substrate

Table 4.2: Index of refraction measurements for parameter space (measurements taken upon removal from vacuum chamber and 720 hr after aging in ambient environments). Color designates optical appearance of each film.

4.3 Summary – Process-Structure-Properties

YSZ thin films were deposited by r.f. magnetron sputtering, and it was demonstrated that film characteristics are greatly dependent on deposition parameters (working pressure, temperature, and gas composition). Resulting film stresses are primarily compressive and are shown to increase in the compressive direction when subjected to ambient conditions (25°C, 75 % relative humidity). It is hypothesized that

increases in film stress are due to absorption of water molecules into the defect structure of films. Using thermal treatment, films can be returned to near-post-deposition stress states. This mechanism is important to understand the possible degradation and mechanical behavior of the films when exposed to ambient or otherwise aggressive environments.

Structural studies revealed that films deposited with no oxygen in the sputtering gas contained primarily tetragonal phase. Introduction of oxygen and variation of total working pressure led to varying percentages of monoclinic and tetragonal phases. The parameter space explored has shown a clear relationship between specific film phase structures and deposition parameters, allowing for the development of future YSZ films characterized by phase structure.

Index of refraction measurements led to qualitative calculation of film packing density as a function of deposition parameters. Index of refraction decreases as total pressure is increased suggesting that resulting films have a high porosity density.

Key Findings: The above investigation led to several key findings that enable the process-structure-properties relationship to be established, as well as, detailed novel findings for further investigations to be discussed later.

- Film stress was shown to be dependent of process parameters – there was a distinct transition from tensile to compressive and it was shown to be tunable.
- Percentages of monoclinic to tetragonal crystal phase were shown to be dependent on process parameters (especially the induction of O₂ into the sputtering gas).

- Calculation of packing density as a function of index of refraction allowed for qualitative analysis of the film's structure or porosity.
- Novel relationship was developed linking water vapor absorption to the increase of compressive stress within the YSZ films.

4.5 References

1. Ruddell D.E., Stoner B.R., and Thompson J.Y., "The effect of deposition parameters on the properties of yttria-stabilized zirconia thin films", *Thin Solid Films* **445**, 14-19 (2003).
2. Liaw B.Y., Rocheleau R.E., and Gao Q., "Thin Film Yttria-Stabilized Tetragonal Zirconia", *Solid State Ionics* **92**, 85-89 (1996).
3. Gao P., Meng .L.J, dos Santos M.P., Teixeira V., and Andritschky M., "Study of ZrO₂-Y₂O₃ Films Prepared By RF Magnetron Reactive Sputtering", *Thin Solid Films*, **377**, 32-36 (2000).
4. Tomaszewski H., Haemers J., De Roo N., Denul J., and De Gryse R., "Yttria-stabilized zirconia thin films grown by r.f. magnetron sputtering from an oxide target *Thin Solid Films* **293**, 67-74 (1997).
5. Wang Y.H. and Li X.P., "Phase-Structure Characteristics of RF Reactively Sputtered Zirconia Thin-Film", *Thin Solid Films* **250**, 132-134 (1994).
6. Amor S.B., Rogier B., Baud G., Jacquet M., and Nardin M., "Characterization Of Zirconia Films Deposited By RF Magnetron Sputtering", *Mater. Sci. Eng. B* **57**, 28-39 (1998).
7. Koh Y-H, Kong Y-M, Kim S., and Kim H-E, "Improved low-temperature environmental degradation of yttria-stabilized tetragonal zirconia polycrystals by surface encapsulation", *J. Am. Ceram. Soc.* **82**, 1456-1458 (1999).
8. Hirsch E.H., "Stress in porous thin films through absorption of polar molecules", *J. Phys D: Appl. Phys.* **13**, 2081-2094 (1980).
9. Ohring M., *The Materials Science of Thin Films*, (Academic Press, London, 1992).
10. Hoffman D.W., "Perspective on stresses in magnetron-sputtered thin films", *J. Vac. Sci. Technol. A* **12**, 953-961 (1994).
11. Thornton J.A., "Influence of apparatus geometry and deposition conditions on the structure and topography of thick sputtered coating", *J. Vac. Sci. Technol.* **11**, 666-670 (1974).
12. Petrov I., Barna P.B., Hultman L., and Greene J.E., "Microstructural evolution during film growth", *J. Vac. Sci. Technol. A*, **21**, S117-S128 (2003).
13. Gilmer G.H., Huang H., de la Rubia T.D., Torre J.D., and Baumann F., " Lattice Monte Carlo models of thin film deposition", *Thin Solid Films* **365**, 189-200 (2000).

14. Garvie R.C., Hannink R.H.J., and Pascoe R.T., "Ceramic Steel", *Nature* **258**, 703-706 (1975).
15. Stamper A.K., Greve D.W., and Schlesinger T.E., "Deposition of textured yttria-stabilized ZrO₂ film on oxidized silicon", *J. Appl. Phys.* **70**, 2046-2051 (1991).
16. Tomaszewski H., Haemers J., Denul J., De Roo N., and De Gryse R., " Yttria-stabilized zirconia thin films grown by reactive r.f. magnetron sputtering", *Thin Solid Films* **287**, 104-109 (1996).
17. Muddle B.C. and Hannink R.H.J., "Crystallography of the tetragonal to monoclinic transformation in Mg)-partially-stabilized Zirconia", *J. Am. Ceram. Soc.*, **69**(7), 547-555 (1986).
18. French R.H., Glass S.J., Ohuchi F.S., Xu Y.N., and Ching W.Y., "Experimental and theoretical determination of the electronic structure and optical properties of three phases of ZrO₂", *Phys. Rev. B* **49**, 5133-5142 (1994).
19. Balzaretta N.M. and da Jornada J.A.H., "Pressure dependence of the refractive index of monoclinic and yttria-stabilized cubic zirconia", *Phys. Rev B* **52**, 9266-9269 (1995).

Chapter 5

Stress Evolution as a Function of Substrate Bias

Data presented in Chapter 4 revealed that sputter-deposited YSZ thin films when exposed to ambient conditions displayed modifications of film stress states in the compressive direction. This section will address the water vapor mechanism and show data on how to deposit a film that limits these affects.

In ambient conditions, effects of water absorption on film properties have been reported to depend on microstructure and composition [1-5]. A porous film structure can promote water vapor absorption in ambient conditions, which in turn can drastically affect optical and mechanical properties. It has also been shown that within stressed zones, water vapor may facilitate internal cracking by breaking metal-oxygen bonds [5]. *Hirsch* proposed a model of absorbed water vapor significantly altering stress states within a film via dipole-dipole interactions [1]. In order for substantial stress increase to occur, pores must be between 10-100Å in size (a smaller pore size leads to larger stress increase). Sign and magnitude of film stress are dependent on characteristics of structural defects and surface area of inter-granular pores [3].

Water vapor effects on yttria-stabilized zirconia (YSZ) thin films have yet to be investigated thoroughly, most likely due to the prevalence of high temperature applications where water vapor is not a factor. Researchers have investigated the detrimental effects of water molecules on other similarly deposited oxide thin films.

Several groups reported that a drift in stress in SiO₂ films was due to the repulsion of permanent dipole moments associated with water molecules that had absorbed on the surfaces of pores within the films [2-4].

Chapter 4 reviewed deposition process parameter space and its effects on stress for 3 mol% YSZ sputtered thin films. Film stress was shown to increase compressively when films were exposed to ambient conditions. It was proposed at the time that this increase was due to the incorporation of water vapor into grain boundary defects. It is important to understand this mechanism as it applies to specific applications (i.e. biomedical, low-temperature, etc.). Figure 5.1 show a representative model of water vapor molecules absorbing into the inter-columnar porosity of YSZ thin films. Increase of compressive stress is facilitated by the dipoles aligning, resulting in a repulsive force. Two distinct ways to eliminate water vapor absorption have been reported: (1) create a more dense film with limited inter-connected porosity (through the application of substrate bias deposition) [6], and (2) use an encapsulation layer that impedes water vapor absorption [7]. Here, YSZ thin films sputtered with varying substrate bias power were exposed to ambient conditions and film stress was evaluated to investigate water vapor effects.

5.1 Deposition of YSZ Thin Film

Chapter 3 describes the sputter deposition and RF magnetron system used throughout this entire study. Substrates used were single crystal four-inch diameter (10.2 cm) silicon wafers (100 orientation). All depositions (n=2) were performed at a RF

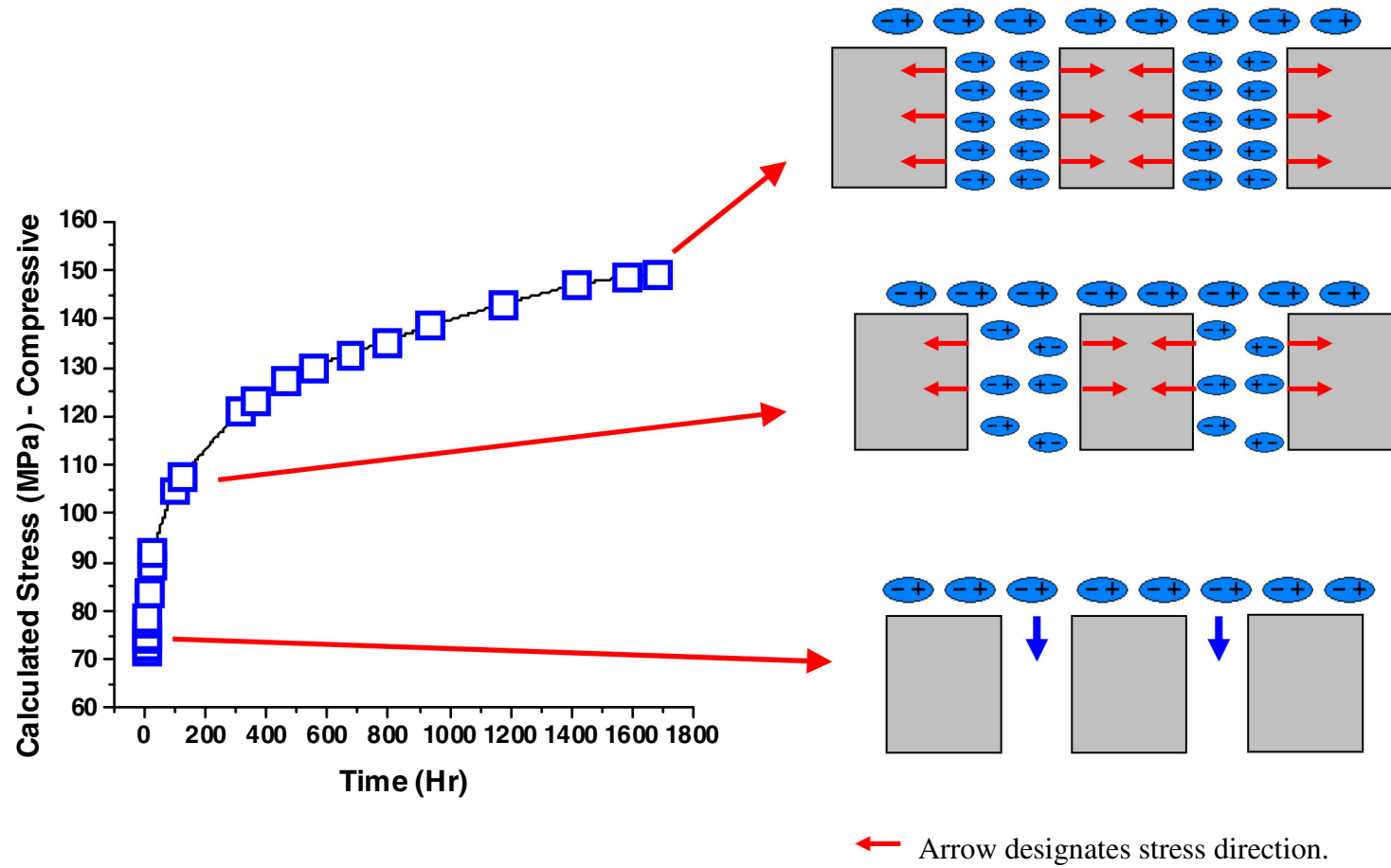


Figure 5.1: Representation of water vapor absorption into inter-columnar porosity of deposited YSZ thin films. Resulting interactions (dipole-dipole) induce compressive film stress.

power of 350W, working pressure of 15mT, temperature of 150°C and Ar/O₂ ratio of 15:1. For bias-assisted sputtering, a secondary RF power source was capacitively coupled to the substrate and increased to a maximum of 50W (10, 25, 50W).

Wafer bow was measured before deposition and then again immediately upon removal from the vacuum chamber, post deposition. Deposition times, regardless of substrate bias power level, were adjusted so that all films had a thickness of approximately 5μm. All films were deposited on the unpolished side of silicon wafer substrates (average roughness (R_a) = 0.4 μm) to increase film adhesion. Samples were stored in a typical ambient environment (75% relative humidity, 25°C) and wafer bow was measured as a function of time to evaluate the effects of environmental exposure.

5.2 Physical Characterization

5.2.1 Film stress

Figure 4.3 displays percent change in compressive stress on films deposited without substrate bias (refer to Chapter 2). Absolute stress values versus post deposition times are shown in Table 5.1. The films were exposed to ambient conditions and stress was measured as a function of time. The largest increase in stress occurred in the first 2 hr of exposure and film stress eventually reaches a steady-state after approximately 70 days. Films were then thermally treated (100°C, 5×10^{-6} torr, 12hr) and film stress re-measured (Figure 4.4). Measured film stress decreased to near baseline, post-deposition values, indicating that most water molecules are physisorbed within the porous structure of the films. Thermal treatments employed in this study may not have been sufficient to completely remove all species that may have chemisorbed onto exposed defect surfaces.

Any remaining chemisorbed water molecules would still result in a non-recoverable compressive stress.

Bias Power (W)	Stress (t = 0) (MPa)	Stress (t = 30d) (MPa)
0	80	150
10	100	170
25	240	270
50	300	310
* Stress values are compressive		

Table 5.1: Absolute stress values at post deposition times of 0 and 30 days.

Low ion energy bombardment during sputter deposition is commonly used to increase film density (refer to Chapter 2). It was thus speculated that using substrate bias would decrease permeability to water vapor and reduce the time-dependent variation in stress. A series of films were deposited using increasing substrate bias power values (10, 25, and 50 W). The films were exposed to ambient conditions and stress measured as a function of time, as with the unbiased films. Figure 5.2 shows measured stress values for each film deposited at varying substrate bias powers at post-deposition and 30 days post-deposition. Initial analysis shows that as bias was increased the percent change in compressive stress was reduced.

The films deposited with the highest applied substrate bias displayed no significant change in film stress upon exposure to ambient conditions for the first two hours following deposition (Figure 5.3). This lack of change in film stress is partially a result of increasing density and a corresponding decrease in inter-columnar porosity. *Knoll et al.* noted that as applied bias during sputtering was increased from 0 to -100V, the microstructure of deposited PSZ films changed from a columnar grain structure with

prominent porosity between grains to a more dense film [8]. Additionally, it was reported that for low applied bias deposited films, defect structure ranged in scale from large inter-columnar cracks to small inter-columnar voids.

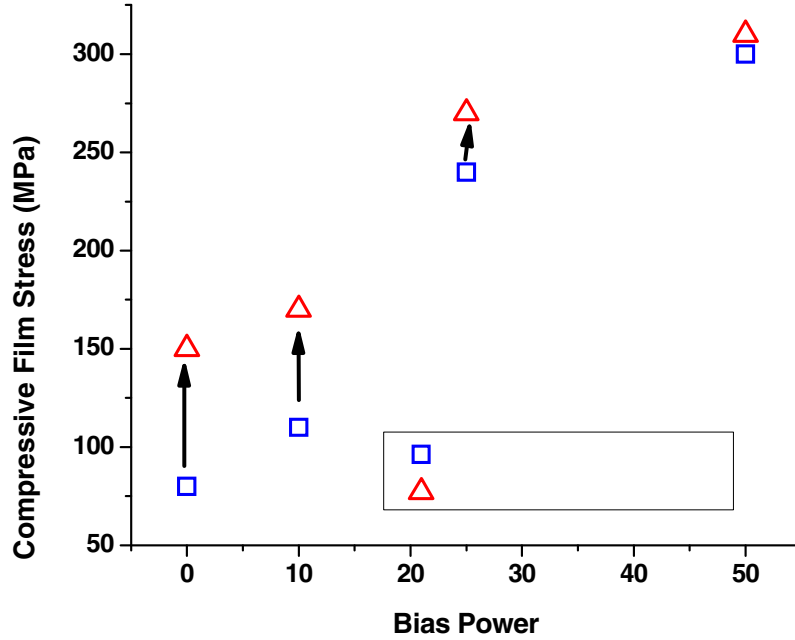


Figure 5.2: Compressive film stress measured for varying substrate bias YSZ films upon removal from vacuum and post 30 days exposure to ambient conditions.

5.2.2 Structural Characterization

However, further analysis of these films suggests that the mechanism may be more complicated than simple densification or elimination of pores. Preliminary analysis via SEM and TEM confirms that a distinct physical difference can be discerned between the biased and unbiased films. Figure 5.4 displays SEM micrographs from two films: (a) no substrate bias and (b) substrate bias power of 50W. Films deposited without substrate bias, display a typical uninterrupted columnar grain structure that would likely promote

inter-columnar porosity enabling the absorption of water molecules. By applying a substrate bias during deposition, the columnar grain growth is noticeably disrupted. This apparent reduction in inter-columnar porosity is expected to limit water vapor absorption

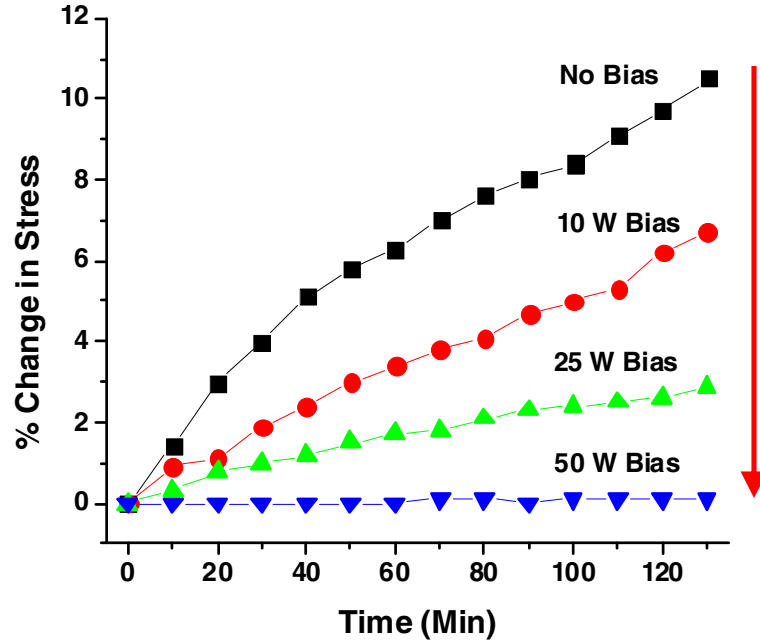


Figure 5.3: Percentage change in measured film stress for a series of films deposited with differing substrate bias power levels. Stress was measured incrementally for the first 2hr of exposure to an ambient environment upon removal from vacuum.

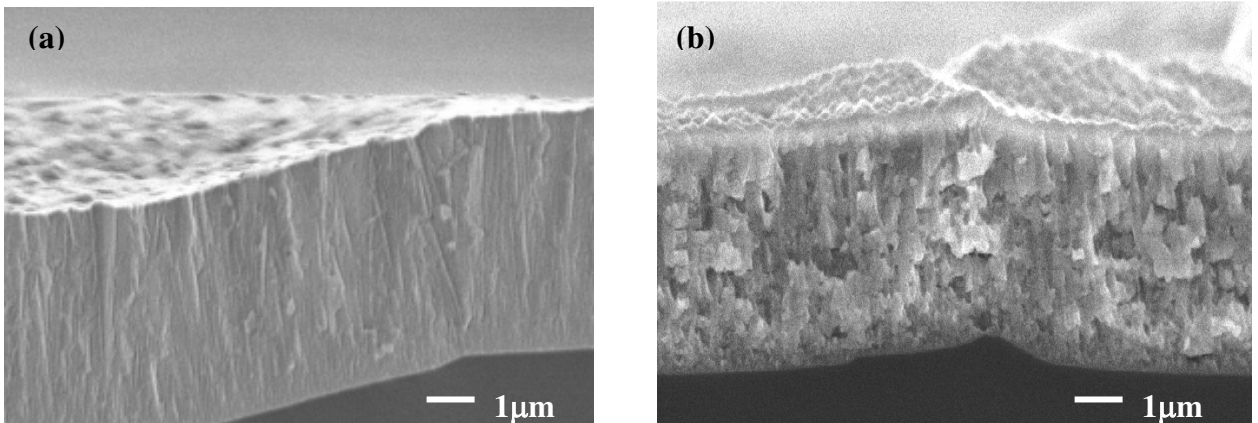


Figure 5.4: Representative SEM micrographs of YSZ sputter-deposited thin films: (a) film deposited without substrate bias and (b) film deposited with 50W power substrate bias.

and subsequently reduce the change in film stress upon exposure to ambient conditions.

Cross-sectional TEM images allowed for a more detailed analysis of the defect structure. Figure 5.5 displays TEM cross-sectional views of films deposited under: (a) no bias, (b) 25W substrate bias, and (c) 50W substrate bias. There is a distinct columnar grain structure (Figure 5.5(a)) with inter-columnar pores for the non-bias film that would enable the absorption of water into the structure. Voids between highly columnar grains typically originate due to low-adatom mobility and self-shadowing during film growth [26]. Figure 5.5(b) displays a film deposited with a 25W substrate bias. It still exhibits a distinct columnar grain structure with some level of inter-columnar porosity, but there also appears to be a large amount of lateral defects. Conversely, when a 50W substrate bias was applied during film deposition, the grains became larger and more equiaxed with limited inter-columnar porosity (Figure 5.5(c)). They also exhibit a regular array of larger, lateral intra-columnar or trans-granular defects. This is an interesting phenomenon whereby the absolute film density appears to have decreased as a result of these micro-cracks; however the water absorption is almost eliminated. It is hypothesized that the trans-granular micro-cracks form as a result of stress-relief in the growing film and the transformation from tetragonal to monoclinic phase due to the bias-induced compressive stress.

As mentioned earlier, the use of low energy ion bombardment during film growth was expected to increase film density, reducing susceptibility to water vapor absorption. As expected, the compressive stress increased and TEM analysis showed that the inter-columnar porosity was reduced. However, there was also a commensurate increase in trans-granular defects. These lateral defects actually suggest a decrease in overall film

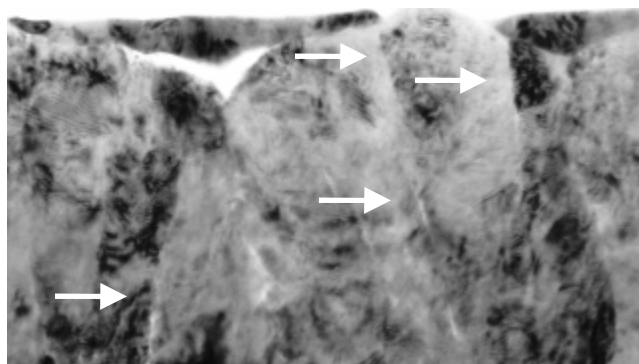
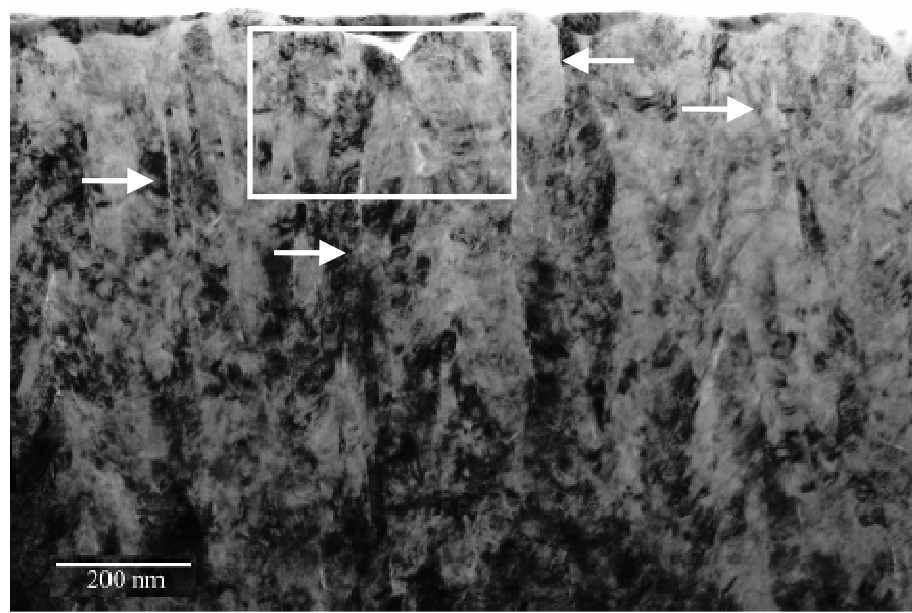


Figure 5.5: Representative cross-sectional TEM micrographs of YSZ sputter-deposited thin films: (a) film deposited without substrate bias exhibits columnar grain structure with inter-columnar porosity (arrows indicate inter-columnar porosity).

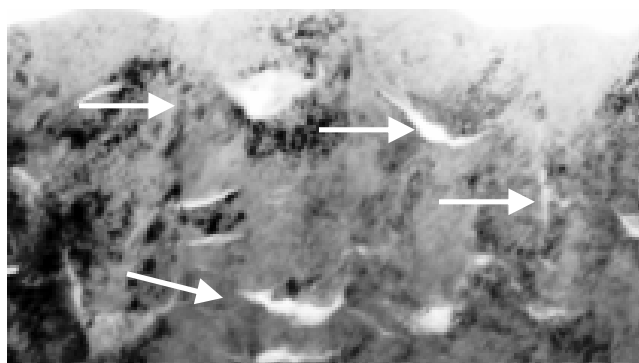
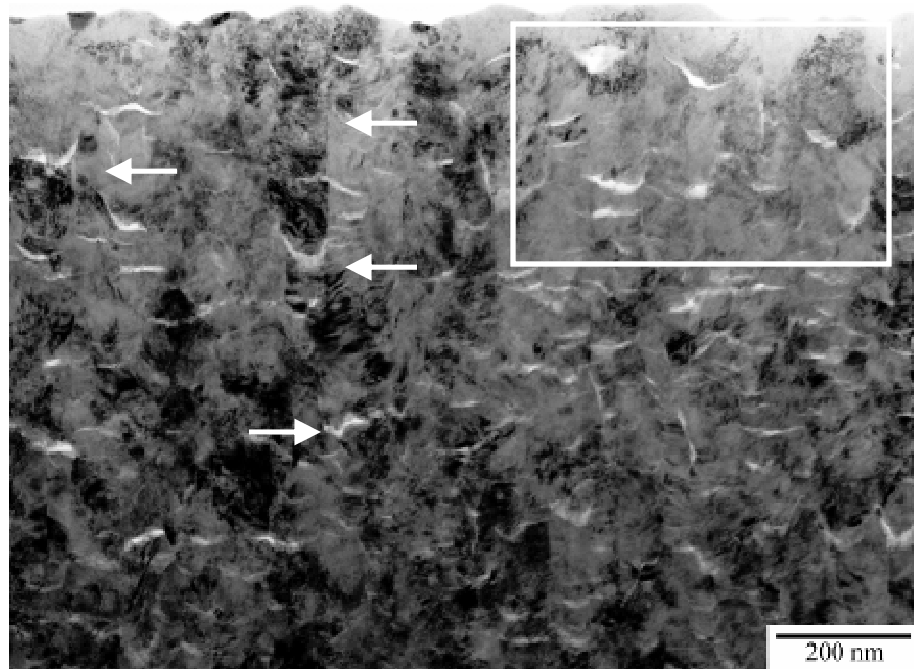


Figure 5.5 (cont): Representative cross-sectional TEM micrographs of YSZ sputter-deposited thin films: **(b)** film deposited with a 25W power substrate bias exhibits columnar grain structure with inter-columnar porosity and presence of lateral defects (arrows indicate inter-columnar porosity and lateral defects).

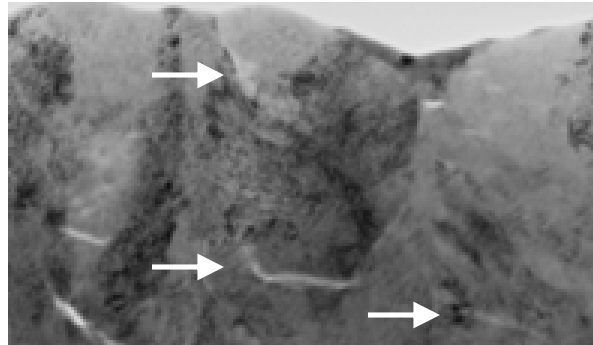
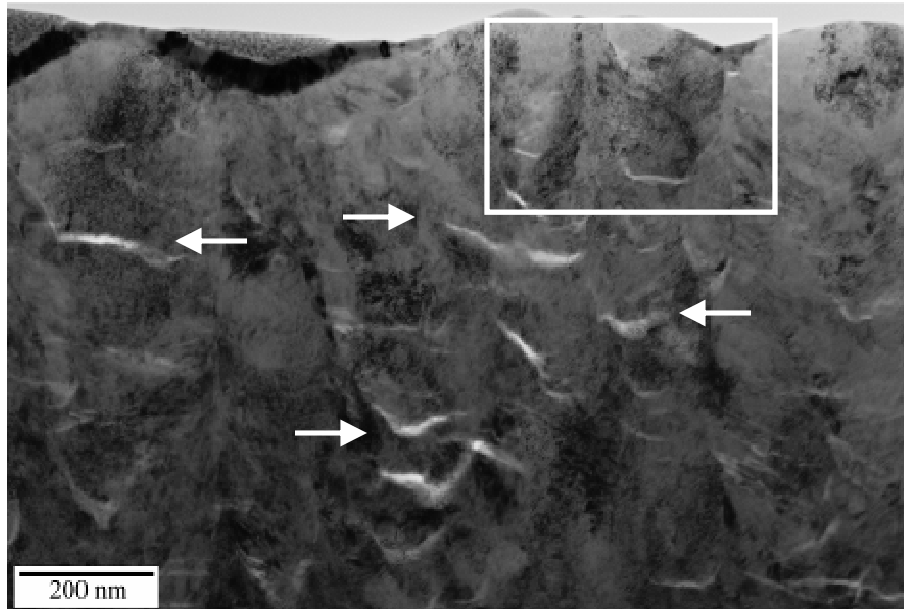


Figure 5.5 (cont): Representative cross-sectional TEM micrographs of YSZ sputter-deposited thin films: (c) film deposited with 50W power substrate bias shows signs of equiaxed grain structure with limited inter-columnar porosity (arrows indicate lateral defects).

density. It is proposed here that these trans-granular defects, or micro-cracks, are a result of a stress-induced phase transformation ($T \Rightarrow M$) that occurs during film deposition. *Garvie*, and *Garvie and Swain* investigated the thermodynamics of martensitic transformations for a constrained YSZ microcrystal with and without an applied stress [9,10]. It was reported that there needs to be sufficient strain energy density produced from an applied stress to overcome the necessary energies within the process zone for such a phase transformation. According to the stress data presented in this research, the compressive values for the biased films may be sufficiently high to induce a martensitic transformation.

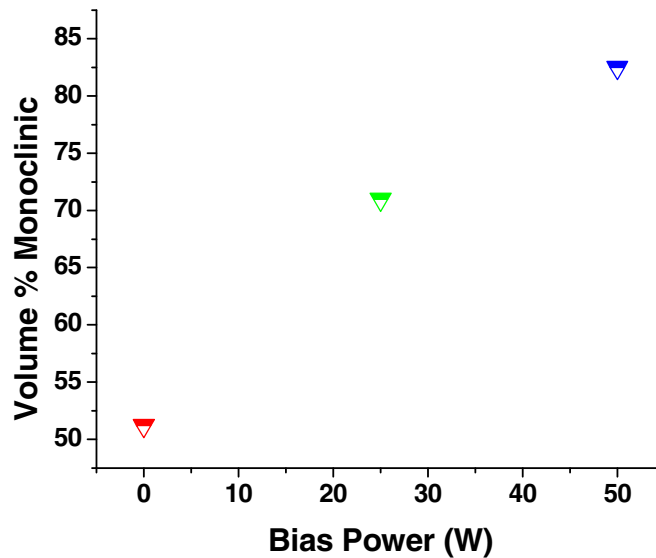


Figure 5.6: Volume % monoclinic phase versus differing bias powers. Graph represents an increase in monoclinic as bias power increases.

By analyzing x-ray diffraction scans, volumetric percent of monoclinic versus tetragonal was calculated [11]. It was found that as bias was increased, the percentage of monoclinic phase increased (Figure 5.6). Since the predominantly c-axis textured, columnar grain structure is a constrained system, periodic micro-cracking may result as a

means of stress relief following phase transformation. Furthermore, *in-situ* martensitic transformation ($T \Rightarrow M$) may explain the higher compressive stress measured in higher biased sample, as a result of volumetric expansion of textured grains. This lateral expansion closes the columnar intra-granular pores and this reduces the films permeability to water vapor.

5.3 Summary – Substrate Bias Deposition

Film stress for RF magnetron sputtered YSZ thin films was investigated as a function of exposure to ambient conditions. It was determined that film stress for films deposited without substrate bias increased compressively due to the incorporation of water molecules into the porous structure. It was verified that an increase in substrate bias power facilitates a reduction in the percent change in compressive film stress upon exposure to ambient conditions. Furthermore, the bias treatment is shown to result in the formation of trans-granular defects that significantly alter the structure and properties of the YSZ thin films. A novel mechanism is proposed whereby the compressive stress increases as a result of ion bombardment. The stress then reaches a threshold for tetragonal to monoclinic transformation; and a volumetric expansion of the constrained, predominately c-axis textured film forces cracking in the z-direction accompanied by an expansion in the x- and y-direction. The next chapter will address and model this transformation mechanism as it relates with intrinsic stress.

Key Findings: Within this section several findings pertaining to YSZ film structure were presented.

- Revealed that sputter-deposited YSZ thin films when exposed to ambient conditions displayed modifications of film stress states in the compressive direction. This section will address the water vapor mechanism and show data on how to deposit a film that limits these affects. Novel water vapor absorption mechanism was shown to be reduced as the application of substrate bias was increased.
- Films deposited with substrate bias had higher compressive film stress and higher percentages of monoclinic phase.
- Lateral defects (or microcracks) were observed in bias films. This coupled with intrinsic film stress was presented as a model of *in-situ* (T \Rightarrow M) phase transformation.

5.4 References

1. Hirsch E.H., "Stress in porous thin films through absorption of polar molecules", J. Phys D: Appl. Phys. **13**, 2081-2094 (1980).
2. Kim S.P., Choi S.K., Park Y., and Chung I., "Effect of water-absorption on the residual stress in fluorinated silicon-oxide thin films fabricated by electron-cyclotron-resonance plasma-enhance chemical-vapor deposition", Appl. Phys. Lett. **79** (2), 185-187 (2001).
3. Sankur H. and Gunning W., "Sorbed water and intrinsic stress in composite TiO₂-SiO₂ films", J. Appl. Phys. **66** (2), 807-812 (1989).
4. Park Y., Lee J.K., Jung I., Heo S-B, and Lee J-Y, "Evolution of residual stress in plasma-enhanced chemical-vapor-deposited silicon dioxide film exposed to room air", Appl. Phys. Lett. **75** (24), 3811-3813 (1999).
5. Michalski T. A. and Frieman S.W., "A molecular mechanism for stress corrosion in vitreous silica", J. Am. Ceram. Soc. **66** [4], 284 (1983).
6. Ljungcrantz H., Hultman L., Sundgren J.E., Johansson S., Kristensen N., Schweitz J.A., and Shute C.J., "Residual stresses and fracture properties of magnetron sputtered Ti films on Si microelements", J. Vac. Sci. Technol. A **11** (3), 543-553 (1993).
7. Koh Y-H., Kong Y-M, Kim S., and Kim H-E., "Improved low-temperature environmental degradation of yttria-stabilized tetragonal zirconia polycrystals by surface encapsulation", J. Am. Ceram. Soc. **82**, 1456-1458 (1999).
8. Knoll R.W. and Bradley E.R., "Correlation between the stress and microstructure in bias-sputtered ZrO₂-Y₂O₃ films", Thin Solid Films **117**, 201-210 (1984).
9. Garvie R.C. and Swain M.V., "Thermodynamics of the tetragonal to monoclinic phase transformation in constrained zirconia microcrystals", J. Mater. Sci., **20** 1193-1200 (1985).
10. Garvie R.C., "Thermodynamic analysis of the tetragonal to monoclinic transformation in a constrained zirconia microcrystal", J. Mater. Sci., **20** 3479-3486 (1985).
11. Wang Y.H. and Li X.P., "Phase-Structure Characteristics of RF Reactively Sputtered Zirconia Thin-Film", Thin Solid Films **250**, 132-134 (1994).

Chapter 6

Stress-induced Phase Transformation in YSZ Thin Films

Earlier chapters have discussed the deposition of YSZ thin films and how the material properties can be altered. Chapter 5 presents a model of an *in-situ* stress-induced phase transformation within the films. This chapter focuses on specific structures developed using substrate bias, and a detailed model of $T \Rightarrow M$ phase transformation using TEM and FEA techniques.

It has been well documented that phase transformation in PSZ can be induced either thermally or mechanically within a crack-tip stress field, associated with a volume strain (4-5%) and a large shear strain (~7%) [1]. Toughening of the material is due to compressive stress generated around the advancing crack tip, which in turn helps absorb crack advancement energies. Additionally, microcracking related to the microstructural accommodation of the transformation shape helps reduce strains and increases toughness by reducing stresses within the transformation zone [1-3]. Garvie presented the first representation of $T \Rightarrow M$ transformation entirely as a function of stress [4]. The Garvie study introduced a model of an individual tetragonal grain subjected to iso-static forces transforming into a monoclinic grain. Garvie concluded that energy supplied by external stress could be thermodynamically linked to transformation.

For a YSZ thin film to be useful as a strengthening coating, it is believed that a majority of the film must consist of tetragonal phase, which could locally transform to monoclinic phase under an applied stress. Discussed in Chapter 4, sputtered YSZ thin films can be deposited in varying percentages of tetragonal phase and varying magnitudes of film stress. Unlike bulk YSZ with micron sized grains, sputter-deposited YSZ thin films have grain sizes in the nanometer range. Intrinsic and thermal stresses, produced during deposition, provide possible transformation mechanisms that are not currently understood. Thus, it is important to investigate transformation within the constraints of a thin film system.

In this chapter, evidence of *in-situ* martensitic transformation ($T \Rightarrow M$) for YSZ sputter-deposited thin films is presented. Our earlier work demonstrated that substrate bias-assisted deposition resulted in higher film stress, increased monoclinic phase content, and a series of lateral defects throughout the film structure. It is proposed here that stresses generated during film growth were sufficient to induce a $T \Rightarrow M$ phase transformation. Lateral defects formed as a result of stress-relief along the columnar grains which undergo rotational strain and volumetric expansion associated with the martensitic transformation. Larger defects, spanning an entire grain, thus form, separating transformed sections of the original columnar structure. Similarly, smaller microcracks form, within a partially transformed zone, displayed a $T \Rightarrow M$ parent-to-daughter phase transition. Both defect structures are presented in this study with supporting analysis from high resolution TEM and fast Fourier Transform (FFT) diffractograms.

6.1 Deposition of YSZ Thin Films

All sputter depositions are outlined in Chapter 3. Substrates used were 10.2cm (4in) single crystal silicon wafers (100 orientation), and films were deposited on the non-polished side ($R_a=0.4\mu\text{m}$) to simulate end-application and increase film adhesion. All depositions were performed at a power of 350 W, 15mT working pressure, 150°C, and an Ar:O₂ ratio of 30:1. For bias-assisted sputtering, a secondary RF power source was capacitively coupled to the substrate and power incrementally increased to a maximum of 50 W.

Film stresses were determined by wafer bow measurements and crystal structure was determined by XRD. Cross-sectional scanning electron microscopy (SEM) and transmission electron microscopy (TEM) samples were prepared to analyze structural differences and investigate martensitic transformations that occurred under bias conditions.

6.2 Physical Characterization

Chapter 5 focused on investigating substrate bias effects on YSZ sputtered thin films. The primary goal was to eliminate water vapor absorption into defects and exposed porosity within the films. The development of unique bias-deposited structures led to further in-depth investigation of observed microstructural defects.

6.2.1 Crystal Structure Analysis

XRD analysis showed that as substrate bias was increased, the amount of monoclinic phase increased with respect to the tetragonal phase (Figure 6.1). A film deposited without bias had approximately 56% monoclinic phase. As bias was increased

the percent monoclinic phase increased to 75% and 83% for 25W and 50W bias respectively. Furthermore, measured film stress increased compressively with higher substrate bias; 310MPa for films deposited with 50W substrate bias.

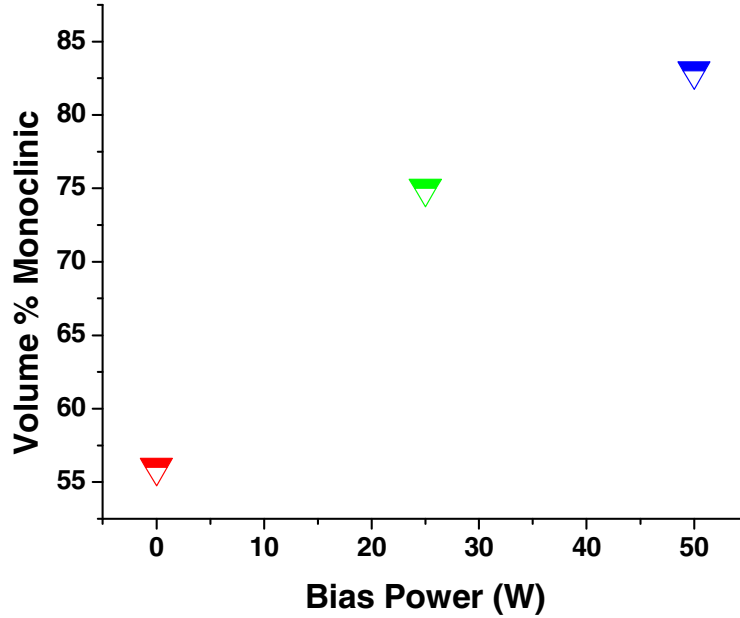


Figure 6.1: Graph displays the relative amount of monoclinic phase present for YSZ films deposited at 0W, 25W, and 50W substrate bias.

Texturing was not investigated, however XRD analysis showed that all films displayed a strong c-axis $\langle 111 \rangle$ texture and SEM cross-sections depicted a highly columnar microstructure. Bauer reported that for tetragonal zirconia the (111) is the most densely packed plane and thermodynamically favorable to grow parallel to an amorphous substrate [6]. Due to this texturing, it has been reported that there is a $(100)_M // (100)_T$ and $[001]_M // [001]_T$ plane and direction relationship, and a corresponding $\sim 9^\circ$ tilt between the $(111)_M$ and $(111)_T$ that occurs after phase transformation [3,7-8].

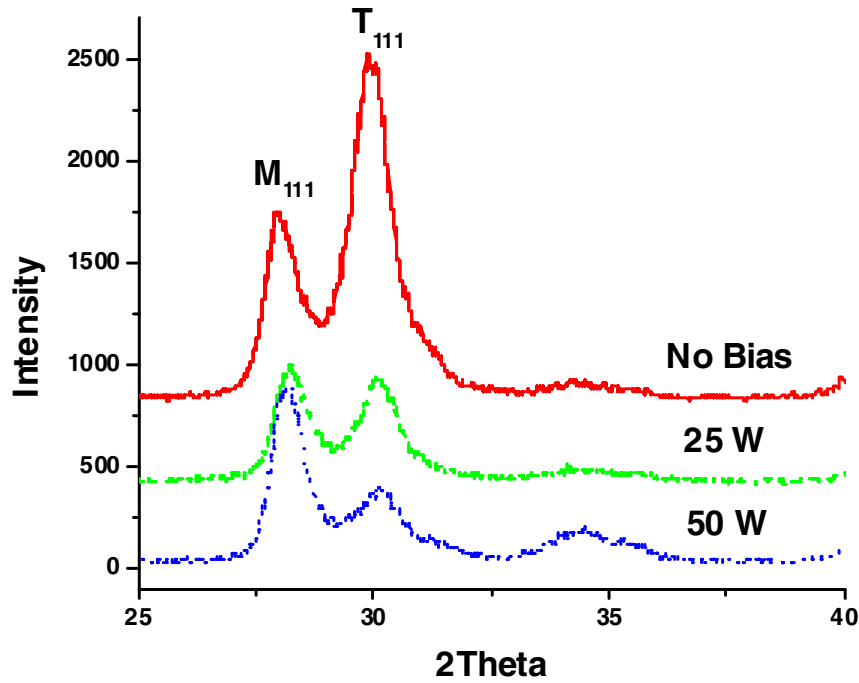


Figure 6.2: XRD patterns for non-bias, 25W, and 50W bias sputtered films showing a decrease in tetragonal phase and increase in monoclinic phase with increased bias power.

6.2.2 Structural Analysis

SEM analysis of YSZ sputtered films confirmed that when deposited without substrate bias, films displayed a columnar grain structure (Figure 6.3(a)). Figure 6.3(b) shows a cross-sectional micrograph of a film deposited with 50W substrate bias. The columnar grain structure is noticeably disrupted and lateral defects can be discerned. Cross-sectional TEM allowed for a more detailed analysis of film structure. It was observed that films deposited with substrate bias had a more equiaxed microstructure, but also exhibited a regular array of lateral defects (or trans-granular microcracks). It is hypothesized that these lateral defects or trans-granular microcracks form as a result of stress relief in the growing film due to the $T \Rightarrow M$ transformation caused by bias-induced compressive film stress.

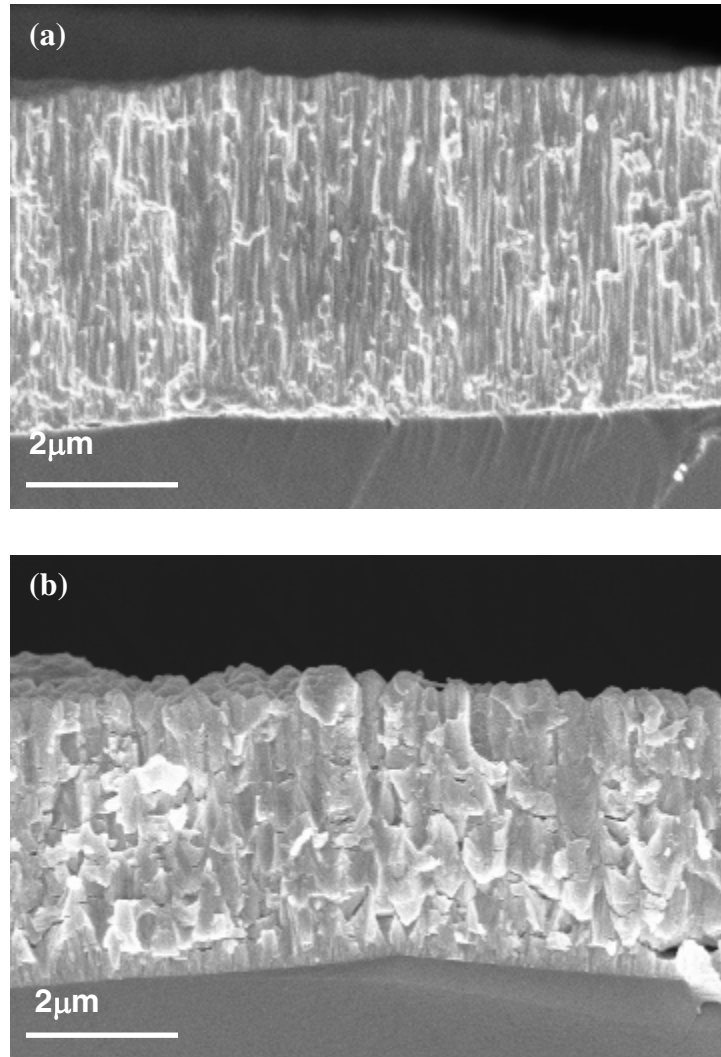


Figure 6.3: Representative SEM images for films deposited (a) without substrate bias and (b) with substrate bias of 50W.

Garvie proposed a simple model based on a tetragonal ZrO_2 microcrystal, subjected to external constraints and a hydrostatic stress field [4]. It was reported that for a $T \Rightarrow M$ phase transformation within the system to occur there must be sufficient strain energy density produced from the externally applied stress. Figure 6.4 is a simplified schematic drawing of a constrained columnar grain of a PSZ sputtered thin film. The model describes a tetragonal grain constrained by surrounding grains, subjected to a bi-

axial external film stress. Earlier film stress measurements confirmed that stress values for the biased films may be on the order of 300 MPa, which, based on Garvie's work, is sufficiently high to initiate a T \Rightarrow M transformation. If this transformation is complete, then there would be a $\sim 9^\circ$ rotation about the a-axis between the tetragonal and monoclinic (111) crystal planes. There is also an accompanied expansion along the c-axis, which results in the volumetric expansion of $\sim 4\%$ within the material. It is thus proposed in this thesis that intrinsic stresses produced during film growth will supply enough energy to the system for phase transformation to occur. However, due to constraints of neighboring columnar grains, there is not sufficient space to accommodate either full rotation or volumetric expansion. Consequently, periodic micro-cracking allows sub-sections to fully or partially transform within the constrained system (Figure 6.4(b)) while minimizing the total film stress.

As described above, the tetragonal to monoclinic transformation is accompanied by a lateral volumetric expansion for a c-axis textured film. The model we proposed is as follows: As the film texture evolves into a columnar grain structure, the system reaches a critical stress threshold supplying sufficient energy to elicit a phase transformation; larger, trans-granular cracks are dispersed throughout the textured grains, bound by both tetragonal and monoclinic phases; and since the transformation alone would result in a further increase in compressive stress, it is believed that nucleation of these trans-granular defects is driven by the need to relieve the overall stress of the system. The u-shaped structure of the defects provides tensile relaxation that reduces the compressive film stress.

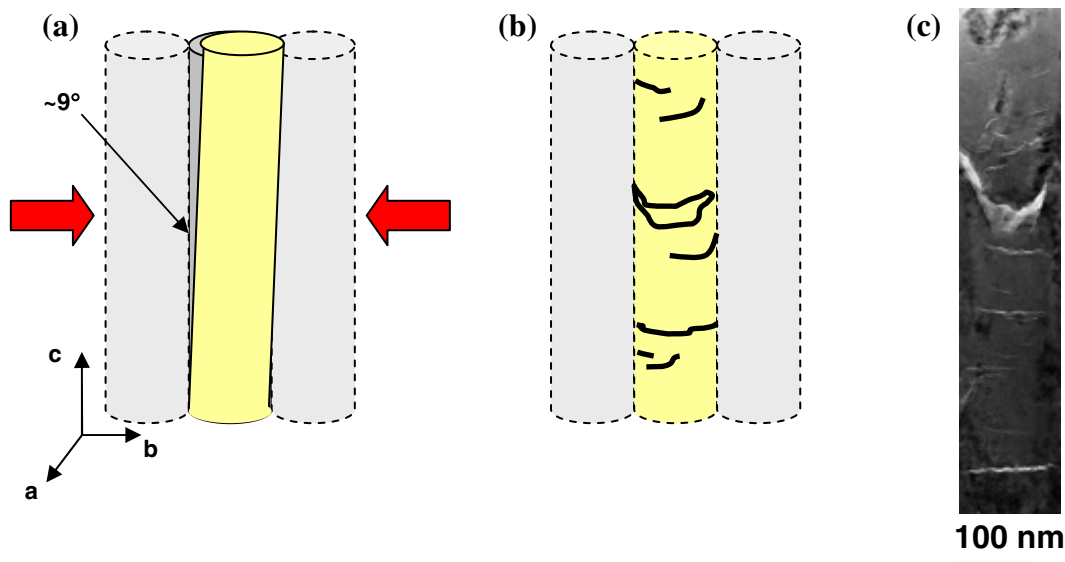
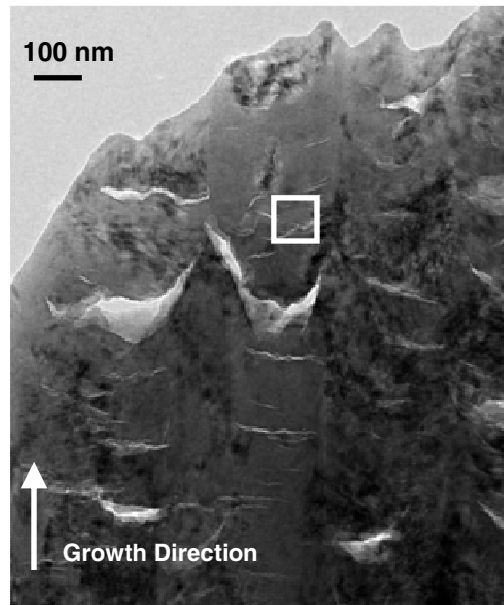


Figure 6.4: Schematic drawing of a constrained T-YSZ cylindrical grain transforming in the presence of an applied film stress: **(a)** shows constrained columnar grains under an applied stress and subsequent transformed grain at a 9° shift, **(b)** depicts the transformed grain with lateral defects (or microcracks), and **(c)** is a low magnification TEM image showing a columnar grain structure from a bias-assisted YSZ sputter deposited film.

As stated earlier, it is believed that larger defects separate areas of complete transformation resulting in primarily monoclinic phase on one or both sides of the defect. The smaller defect regions are also noteworthy: It is presumed that volumetric expansion due to transformation would elicit microcracking and areas of tetragonal phase with a transition to monoclinic phase would be evident. To further support this model, HRTEM and fast Fourier Transform (FFT) diffractogram calculations of planar spacing were performed in areas close to observed defects. Shown in Figure 6.5(a) is a TEM micrograph of a cross-sectioned 50W substrate bias deposited film. Lateral defects and smaller phase boundaries can be identified throughout the film. Figure 6.5(b) is a HRTEM with boxed areas showing a tetragonal region, a region of transformation, and a converted

(a)



(b)

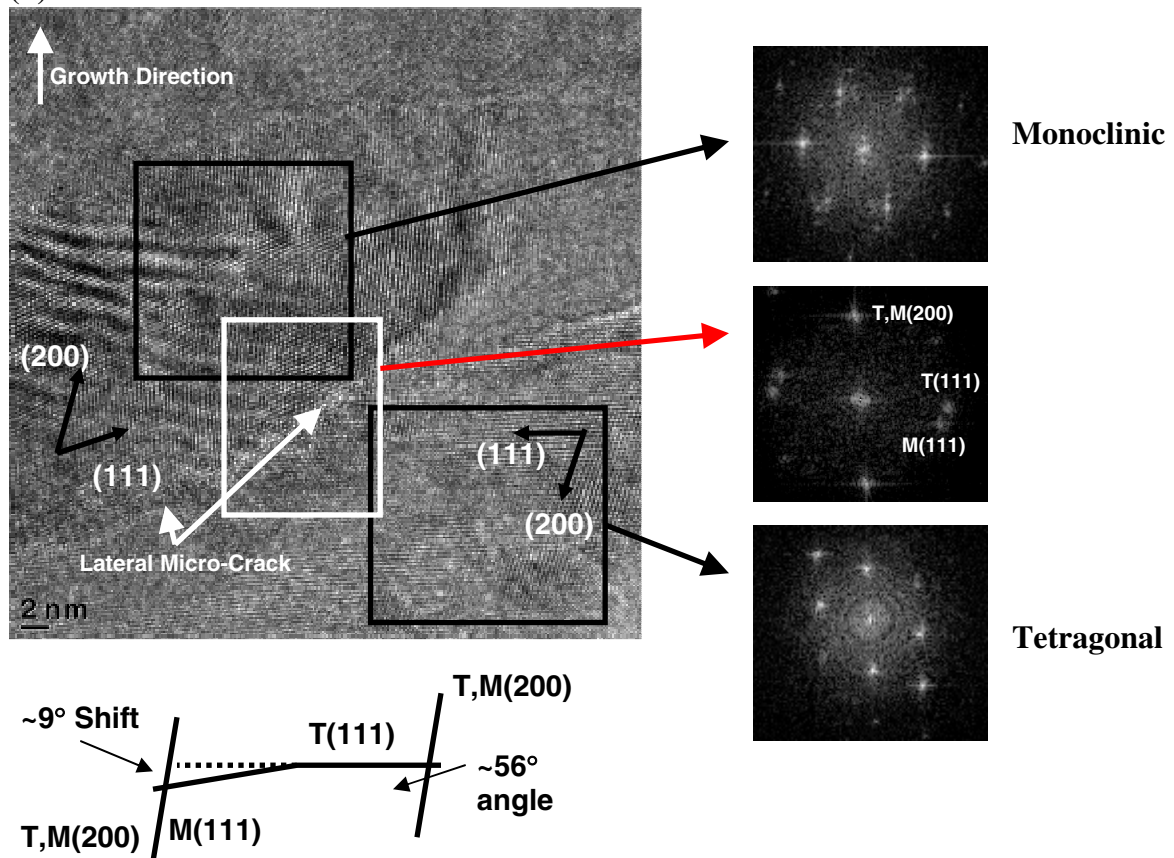
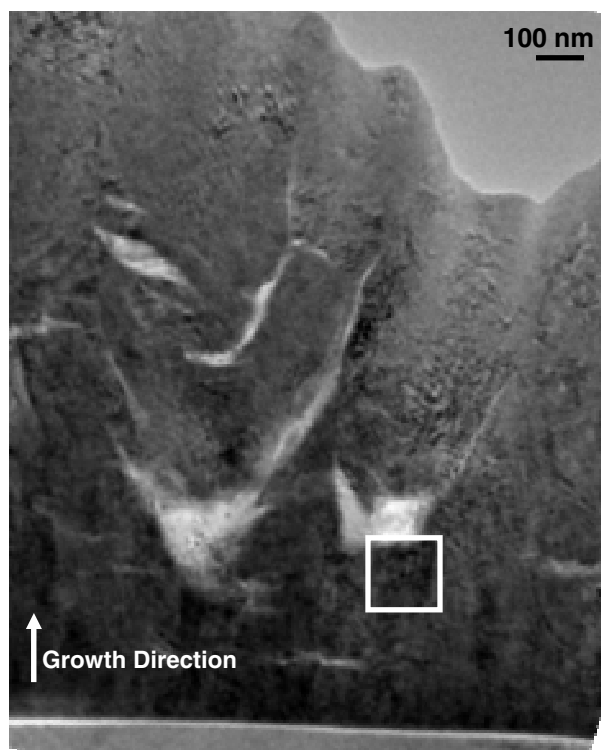


Figure 6.5: (a) Low magnification of 50W substrate bias deposited YSZ thin film. (b) High resolution TEM of boxed area shown in (a). FFT diffractograms confirm T \Rightarrow M transformation area.

monoclinic phase region. Corresponding FFT diffractograms are shown with lattice spacing confirming the transformation from tetragonal to monoclinic phase near a defect. As reported in earlier studies, the c-axis of parent and daughter phases are parallel and the (200) lattice fringes are invariant in spacing and have an angle of $\sim 56^\circ$ with both the tetragonal and monoclinic regions [7, 9]. Based on d_{hkl} spacing of bulk ZrO_2 , $(111)_T$ and $(111)_M$ are 2.96Å and 3.16Å [10]. The measured planar spacings were 2.965Å and 3.087Å respectively. The measured inter-planar angle between the $(111)_T$ -(200) $_T$ was $\sim 59^\circ$, and $(111)_M$ -(200) $_M$ was distorted to $\sim 63^\circ$. In the current study, the transformation region displays $\sim 10^\circ$ tilt between the $(111)_T$ and $(111)_M$ confirming a $T \Rightarrow M$ transformation that involves an out-of-plane rotation of $\sim 9^\circ$ between the two planes. It is believed this 10° tilt about the a-axis is enhanced due to transformation-induced volumetric expansion of the material, and a result of stress-relief microcracking. Light and dark bands can be seen in the transformed monoclinic area. Further investigation needs to be performed to differentiate between areas of residual strain as a result of the transformation, possible twinning, or Moire fringes [7, 11].

Figure 6.6(a) is a low magnification TEM of an area close to the substrate/film interface. Figure 6.6(b) depicts a high magnification area close to the interface and below a large lateral defect. What is shown is an area of parent tetragonal phase and the subsequent transformation zone, which has changed to monoclinic phase. FFT diffractograms of the boxed areas confirmed the phase identification of both T and M phases. Lattice measurements corresponded to previous measured values and are noted within the figure. Tetragonal phase near the interface of the Si substrate was observed, similar to previous reports [24]. During film growth, stress becomes a dynamic factor

(a)



(b)

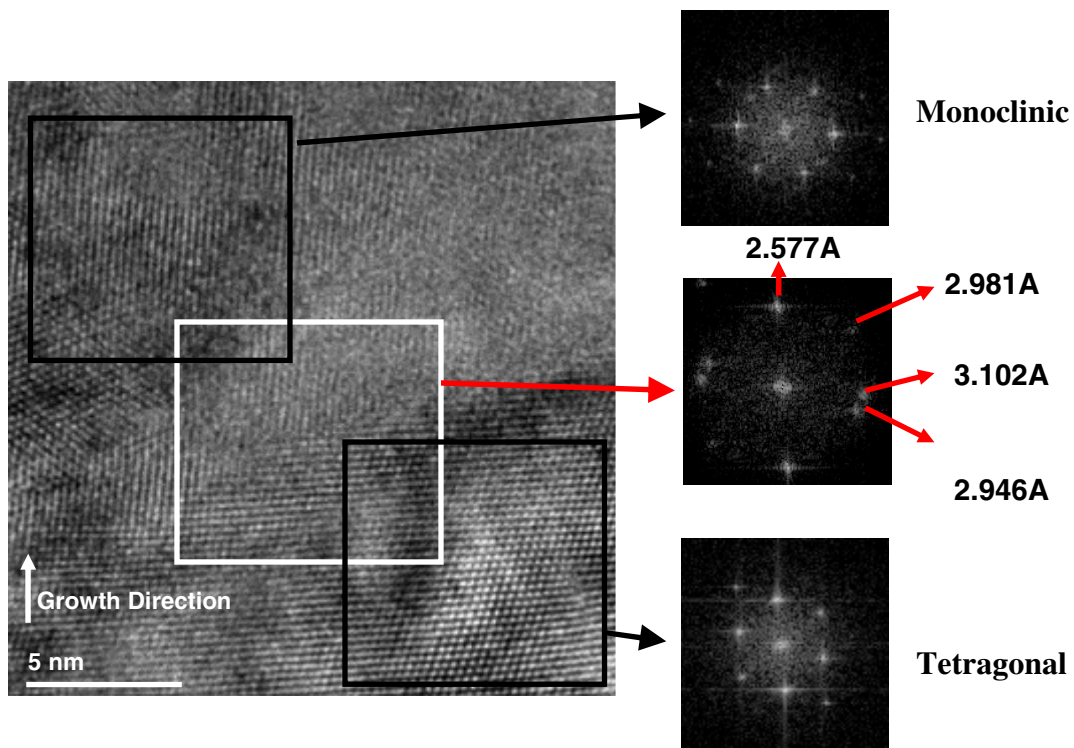


Figure 6.6: (a) Low magnification TEM of 50w substrate bias YSZ film showing lower portion of the cross-sectional wedge - interface between film and substrate. (b) High resolution TEM of transformation area.

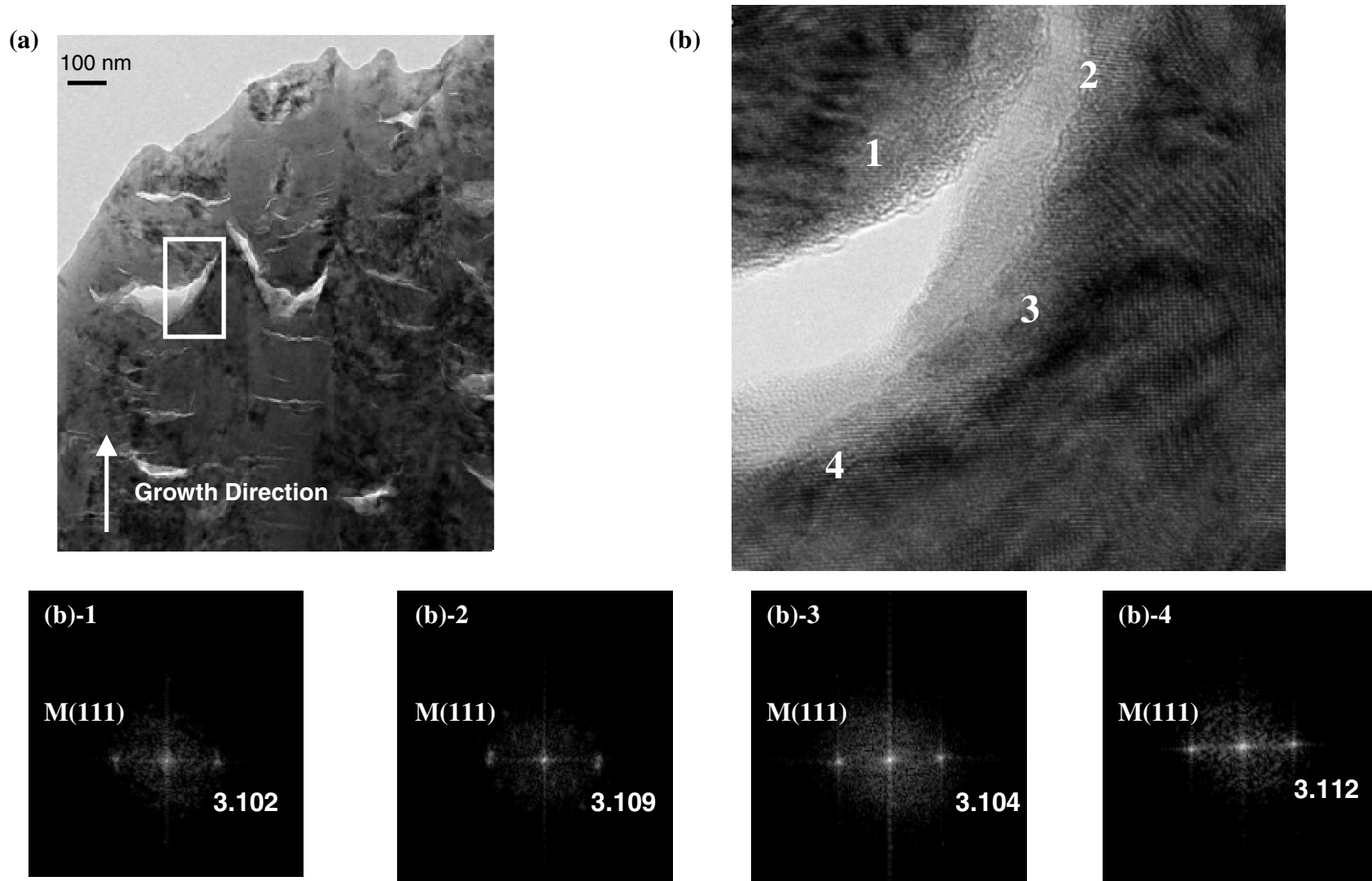


Figure 6.7: (a) Low magnification of 50W substrate bias deposited YSZ thin film. (b) High resolution TEM of boxed area shown in (a). FFT diffractograms confirm M transformation area around the edges of large u-shaped defect.

(thermodynamically) in supplying energy to the system, increasing the probability of transformation.

Figure 6.7 is a representative TEM of a film deposited with a 50W substrate bias. In Figure 6.7(b), is a HRTEM of the boxed are shown in (a) of one of the large u-shaped defects. Noted earlier, it was hypothesized that these defects are areas of complete transformation and should be bound by transformed monoclinic phase. Specific locations surrounding the defect were selected for FFT analysis. The FFT diffractograms and lattice spacing measurements confirmed that monoclinic phase binds the edges of the defect. Lattice spacing measurements are noted on the diffractograms shown in Figure 6.7.

6.2.3 Finite Element Analysis (FEA)

The model of transformation assumed that the applied stress was bi-axial stress and compressing the circumference of the columnar grains. The portion of the strain energy density generated by the applied stress which is involved in the thermodynamics of the transformation is designated W_a , and is related to interaction energies. To facilitate analysis, the tetragonal metastable grains are assumed to be located within specific process zones; these zones are described as a region where t-particles transform to m-symmetry due to the influence of the applied stress via the interaction energy term W_a . The thermodynamic description of the transformation is given by [Garvie]:

$$(\Delta F_0/V) = \Delta F_{\text{chem}} + \Delta F_{\text{dil}} + \Delta F_{\text{shr}} + (6\sum \Delta S/d_c) + W_a < 0 \quad [\text{Eqn. 6-1}]$$

where ΔF_0 total change in free energy of the transformation, V is the volume, ΔF_{chem} is the chemical (Helmholz) free energy, ΔF_{dil} is the strain energy density generated by the volume expansion associated with transformation, ΔF_{shr} is the residual shear stress after

transformation, $\sum \Delta S$ is the sum of all the interfacial energy terms, and d_c is the critical diameter for which transformation occurs for a particular applied stress [Garvie no stress]. Using these thermodynamic relationships established by Garvie, it was determined that the overriding transformation strain within the system is solely dependent on the applied bi-axial stress.

For brittle materials, cracks are generally assumed to form by the cleavage of atomic bonds in highly stressed regions. These stresses may be due to stress concentrations or residual stress and they will be particularly effective in producing cracks if weak interfaces are present. It has been stated that the presence of high stresses is associated with the heterogeneous nature of the material at the microstructural level or inelastic deformation at localized contacts. It is known that cracks can form at contact events, voids produced during processing, and stresses formed due to temperature changes. It is extremely useful to identify sources of high stress within the microstructure. Areas of microstructural misfits or phase transformations can lead to microscopic areas of stress, which in turn leads to crack formation. Once a crack nucleates, it may undergo further growth, especially if there is a localized stress field associated with the nucleation process, or if growth is impeded by microstructural obstacles [Green].

SEM and TEM micrographs showed that bias-assisted films displayed large lateral defects (or microcracks) dispersed throughout the entire thickness of the films. It was therefore hypothesized that the presence of the defects was a function of stress-relief in the growing film induced by the $T \Rightarrow M$ phase transformation. The model consisted of evaluation of film stress and assuming a constrained system, that film stress reaches a

transformation threshold, and that do to volumetric expansion, microcracking results as a consequence of system stress-relief.

FEA allowed for the system to be modeled and stress contours (fields) to be mapped to better understand the mechanisms of the model. The constraints for the purpose of analysis (Figure 6-8) of a 50W substrate bias deposited film, is applying a uniform pressure at all curved surfaces. The top surface is free of constraints and the base is fixed to the substrate. The areas shown in red designate pressure or the applied stress, the lower portion (blue region) displays the boundary conditions, and the arrows (lower portion) describe the reaction on the substrate. Based on this model, the uniform pressure means that the Poisson's effect is seen along the c-axis.

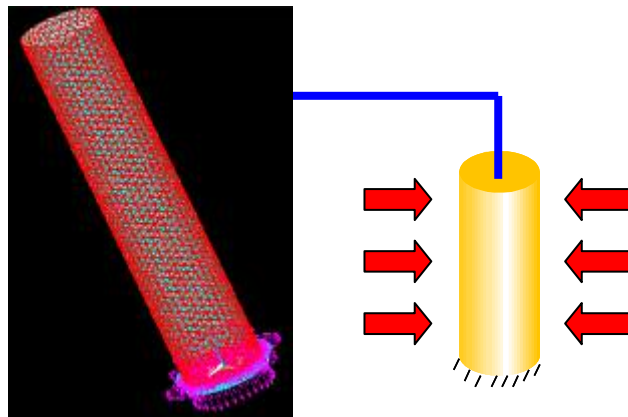


Figure 6.8: Representation of the 3-D model using in evaluating stress in columnar grains.

A compressive film stress (Figure 2.3) would provide a bi-axial stress on the outer surfaces of the columnar grains by the surrounding grains. Also, the bottom of each grain is constrained due to attachment to the substrate. The top portion (or addition of material due to growth) would be unconstrained and not bound by external forces. Using substrate bias during deposition alters the internal (or intrinsic) stresses within the

growing film. Mentioned in Chapter 2, substrate biasing is used to increase the density of the film. This ion bombardment during film growth can increase intrinsic stress (compressive) and produce crystallographic flaws; such as, interstitial defects and/or entrapped species. A consequence of a high compressive intrinsic stress is that the grain would literally want to expand out from its boundaries.

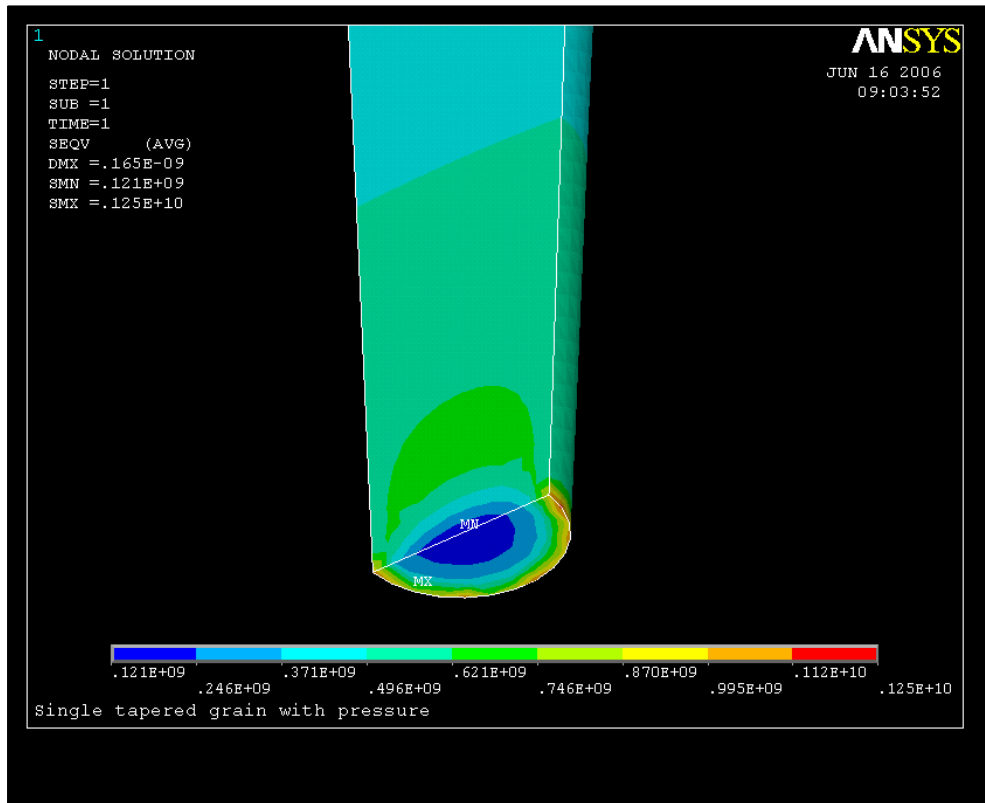


Figure 6.9: FEA analysis of 300 MPa film stress (Von Mises) on columnar grain.

It is proposed that the larger, u-shaped defects (Figure 6.6(a)) are areas of complete phase transformation, resulting in monoclinic phase present around the edges of the defect. Based on experimental measurements, film stress post-deposition was 300 MPa. The neighboring grains would then effectively press on each other, creating a constrained system. Using the above parameters, a FEA model was created to map stress

fields within a columnar grain (Figure 6-9). The FEA model showed that stress reaches a maximum, creating domed shaped stress fields (contours) inside the grain. The apex of the dome, described by a higher stress magnitude, would depict a nucleation site for $T \Rightarrow M$ transformation. The base radius was very critical because it was constrained and subsequently causes an increase in stress. The smaller the radius, the lower the maximum stress and sharper the stress contours.

Since the films are predominantly c-axis ($\langle 111 \rangle$) texture, there is a $(100)_M // (100)_T$ and $[001]_M // [001]_T$ plane and direction relationship, and a corresponding $\sim 9^\circ$ tilt between the $(111)_M$ and $(111)_T$ that occurs after transformation. Also, there is an accompanied expansion along the c-axis, which results in a volumetric expansion of $\sim 4\%$ within the material. As the film texture evolves into a columnar grain structure, the system reaches a critical stress threshold supplying sufficient energy to

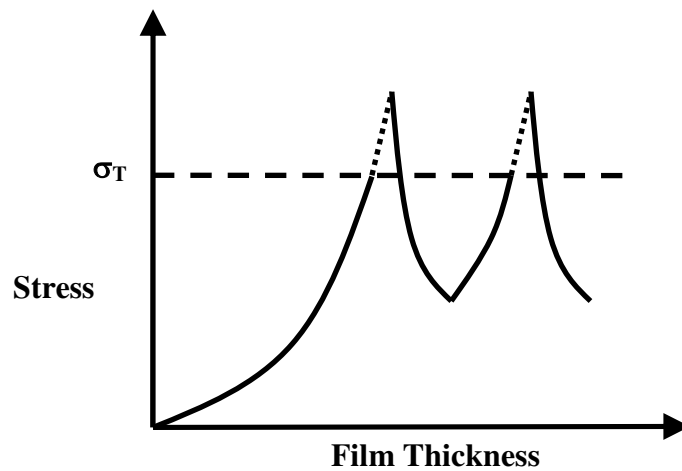


Figure 6.10: Plot representing increase in film stress versus thickness. Stress reaches a threshold (σ_T) designating phase transformation, spikes upward, and then relaxes.

elicit a phase transformation. This point of transformation was determined by the apex of the domed stress field created inside the grain. Stress contours for a 300 MPa biaxial stress were shown to reach a maximum of approximately 620 MPa, leading to the

conclusion that there was sufficient energy for transformation. It is believed that once a transformation event occurs, there is spike in stress as a result of volumetric expansion. A subsequent microcrack is formed by the need to relieve the overall stress of the brittle material system. Figure 6-10 is a proposed relationship for stress versus evolving film thickness. It was presumed that as a film grows, the stress will increase and reach a threshold for transformation (σ_T). At this point stress will increase further due to the transformation-induced lateral and volumetric expansion. Once transformation is complete and structural accommodations have occurred (or microcrack formation), then there is a relaxation that relieves the intrinsic stress. As the film continues to grow, this behavior of stress increase, followed by transformation, followed by defect introduction will persist until film deposition termination.

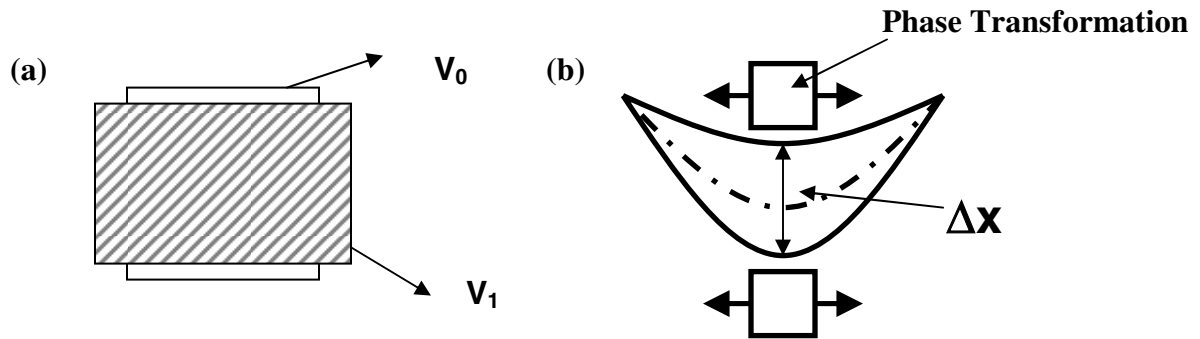


Figure 6.11: (a) Representation of volumetric change due to Poisson's effect (where V_0 is the original volume and V_1 is the post transformation volume). (b) Dimensions of a u-shaped defect bounded by transformation events.

The larger, u-shaped defects are believed to be areas of complete transformation with edges bounded by the resultant monoclinic phase. It was suggested that once a transformation event takes place, there is a lateral expansion complemented by a longitudinal relaxation, or Poisson's effect (Figure 6-11(a)). Since the film is c-axis textured, the lateral and volumetric expansion would elicit this relaxation in the c-

direction. A crack would initiate due to an increase in localized strain at the point on transformation and the need to relieve stress within the grain. This crack initiation was believed to happen since the film does not delaminate from the substrate. Based on Poisson's ratio and volumetric change, the deformation of the material can be calculated using a simplified formula (only for small deformations):

$$(\Delta V/V) = (1 - 2\nu) (\Delta L/L) \quad [\text{Eqn. 6-2}]$$

where, V is material volume, ΔV is material volume change, ν is Poisson's ratio, L is original length (before stretch), and ΔL is the change in length ($\Delta L = L_{\text{Old}} - L_{\text{New}}$). By normalizing the dimensions of the basic crystal structure, it was determined that there would be ~10% longitudinal reduction (c-axis) as a result of transformation. This

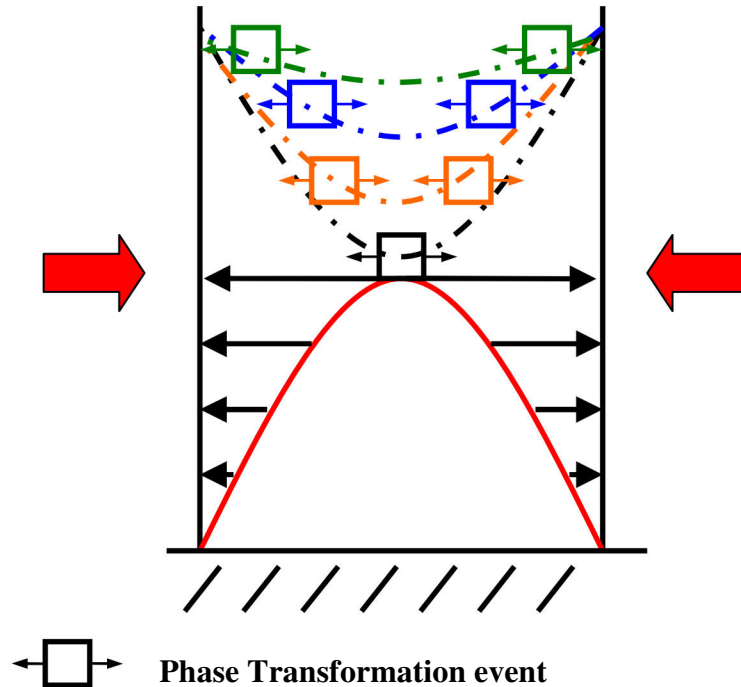


Figure 6.12: Schematic of defect generation as a function of intrinsic stress and transformation events.

normalization allows for the approximation of 9-10% change in defect width shown in Figure 6.11(b).

Once this transformation occurs and a subsequent crack is formed, then stress within the grain would be altered. The same boundaries would apply underneath the crack, three sides fixed with neighboring grains supplying a bi-axial stress, but stress states above the crack would be altered. As transformation and a crack are initiated there is still sufficient strain within the system to elicit further transformation events. The resulting transformation would supply additional strain, allowing the crack to grow. The shape of the crack follows the direction of lower opposing stresses from neighboring grains. The crack will allow the grain to relax inwards, toward the center, reducing the external stresses produced by neighboring grains. It is hypothesized that the u-shaped defects are formed rapidly and are terminated at the grain boundaries.

Partial phase transformations described in Figure 6.5 are randomly oriented small lateral defects. These are generated due to localized XY shear strain caused by either film growth and/or redistribution of intrinsic stresses caused by u-shape defect formation. FEA modeled a columnar grain under the above noted constraints. Figure 6.13 describes the XY localized shear stress due to a 300 MPa bi-axial film stress. Areas of shear stress are shown to be random in orientation within the interior of the grain. The current model does not account for larger u-shape defect formation, so exact prediction of specific areas of localized stress was difficult. However, based on the model, it was determined that during growth, intrinsic stresses would enhance the probability of induced partial phase transformations.

6.3 Summary – TEM and FEA Modeling of Phase Transformation

YSZ thin films deposited with an accompanying substrate bias displayed higher compressive stresses and a larger percentages of monoclinic phase. In addition, cross-sectional SEM and TEM showed that bias-assisted films had a large array of lateral defects (microcracks) throughout the film structure. A model was derived to explain the presence

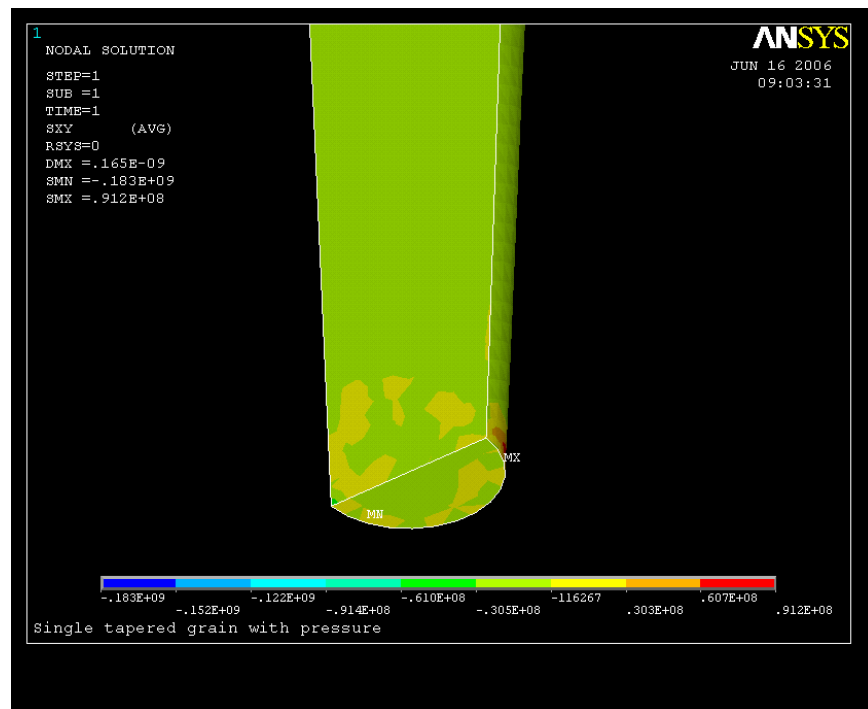


Figure 6.13: Representation of XY shear stress within a columnar grain subjected to a 300 MPa uniform bi-axial stress.

of the defects as a function of stress-relief in the growing film during stress-induced phase transformation from $T \Rightarrow M$. HRTEM and FFT diffractograms of suspected transformation areas close to observed defects confirmed $T \Rightarrow M$ transformation zones. By evaluating film stress and assuming a constrained system, it is believed that film

stress reaches a threshold for $T \Rightarrow M$ transformation, and that due to transformation-induced volumetric expansion, microcracking results as a consequence of stress relief.

The observed lateral defects create an interesting structure that could be useful in increasing brittle substrate fracture toughness. Applying YSZ thin films with intrinsic lateral defects may provide a useful structure when subjected to forces perpendicular to the surface. This structure could promote crack-tip shielding better known as microcrack toughening.

Utilizing FEA techniques allowed for development of a model of phase transformation. As a uniform stress is applied to a columnar grain, stress fields within the grain dome upward, away from the substrate until it reaches a maximum. Once enough energy is supplied from intrinsic stresses, transformation will occur. Due to the brittle nature of YSZ, sites of transformation create nucleation sites for microcracks (of defects).

Key findings: The phase transformation within YSZ thin films had not been investigated as thoroughly as bulk YSZ. Mainly due to the constraints bound by grain size and analytical techniques.

1. HRTEM and FFT documented $T \Rightarrow M$ phase transformation never seen before in sputter-deposited YSZ thin films.
2. Novel model of stress-induced phase transformation and resultant lateral defect generation due to system stress-relief mechanisms.
3. FEA supported model of transformation and defect generation.

6.4 References

1. Green D.J, *An Introduction to the Mechanical Properties of Ceramics*, (Cambridge University Press, London, 1998).
2. Hoshide T., Nebu A., and Hayashi K., "Bending strength of borosilicate glass coated with alumina and silicon carbide by rf magnetron sputtering", *JSME Int. J.* **41**, 332-337 (1998).
3. Hannink R.H.J. and Swain M.V., "Progress in transformation toughening of ceramics", *Annu. Rev. Mater. Sci.*, **24**, 359-408 (1994).
4. Garvie R.C., "Thermodynamics of the monoclinic phase-transformation in constrained zirconia microcrystals in the presence of an applied stress", *J. Mater. Sci.*, **20** 3479-3486 (1985).
5. Ruddell D.E., Stoner B.R., and Thompson J.Y., "The effect of deposition parameters on the properties of yttria-stabilized zirconia thin films", *Thin Solid Films* **445**, 14-19 (2003).
6. Bauer E., *Single Crystal Films*, (MacMillan Press, New York, 1964).
7. Gajdardziska-Josifovska M. and Aita C.R., "The transformation structure of zirconia-alumina nanolaminates studied by high resolution electron microscopy", *J. Appl. Phys.*, **79**(3), 1315-1319 (1996).
8. Muddle B.C. and Hannink R.H.J., "Crystallography of the tetragonal to monoclinic transformation in Mg)-partially-stabilized Zirconia", *J. Am. Ceram. Soc.*, **69**(7), 547-555 (1986).
9. J.W. Edington, *Practical Electron Microscopy in Materials Science*, (MacMillan Philips Technical Library, Eindhoven, 1975).
10. ASTM Joint Committee on Powder Diffraction Standards, 1974, File Nos. 17-923 and 37-1484.
11. Dravid V.P., Notis M.R., and Lyman C.E., "Twinning and microcracking associated with monoclinic zirconia in the eutectic system zirconia-mullite" *J. Am. Ceram. Soc.*, **71**(4), C219-C221 (1988).
12. Garvie R.C. and Swain M.V., "Thermodynamics of the tetragonal to monoclinic phase transformation in constrained zirconia microcrystals", *J. Mater. Sci.*, **20** 1193-1200 (1985).
13. Green D.J, *An Introduction to the Mechanical Properties of Ceramics*, (Cambridge University Press, London, 1998).

14. Gere J.M. and Timoshenko S.P., *Mechanics of Materials*, (PWS, Boston, MA, 1997).
15. Askland, D.R., *The Science and Engineering of Materials*, (PWS-Kent, Boston, MA, 1984).

Chapter 7

Deposition of YSZ thin films on soda-lime glass substrates

This work focused on understanding material properties of YSZ thin films as they relate to deposition parameters. Previous chapters detail techniques, material properties, and a unique structure created by depositing films with an applied substrate bias. It is important to evaluate these properties to better understand what type of film could be produced for end applications. This chapter will focus on describing replication of specific structures on a different substrate (soda-lime glass) that has similar bulk properties to a dental ceramic (porcelain).

Water vapor effects on YSZ thin films have not been investigated thoroughly, but its importance for any biomedical application is potentially critical, and needs to be fully understood. Chapter 5 details the effects of applying a substrate bias to alter film structure, which ultimately changes YSZ film density, eliminating water vapor absorption in the structure. In order to increase film density, low-energy ion bombardment (substrate bias) is commonly used [1-3]. It was shown that by increasing substrate bias power, the film stress increased compressively, and water vapor absorption was reduced. A complete analysis of the films showed a more complicated mechanism was present (Chapter 6). Intrinsic stresses, produced during deposition, provided sufficient energy to elicit a T \Rightarrow M phase transformation. Instead of an expected increase in film density,

substrate bias-assisted deposition resulted in higher film stress, increased monoclinic phase content, and a series of lateral defects throughout the film structure. Chapter 6 describes that stresses generated during film growth induce a $T \Rightarrow M$ phase transformation and lateral defects form as a result of a stress-relief mechanism. It is hypothesized that this structure may produce improved fracture toughness properties when applied to brittle substrates, similar to microcrack toughening [4].

7.1 Deposition of YSZ thin films

Sputtering techniques are described in Chapter 3. Substrates used were 4in. (10.2cm) single crystal silicon wafers (100 orientation) and soda-lime glass (Mark Optics, Santa Ana, CA). Specific material properties are shown in Table 3.1. Films were deposited on the non-polished ($R_a=0.4\mu\text{m}$) side to simulate end-application and increase film adhesion. All depositions were performed at a power of 350W, 15mT working pressure, 150°C, and an Ar:O₂ ratio of 30:1. For bias assisted sputtering, a secondary radio frequency (RF) power source was capacitively coupled to the substrate and power increased to a maximum of 100 W. Film stress was determined by wafer bow measurements, crystal structure was analyzed using a powder x-ray diffractometer (XRD), and scanning electron microscopy (SEM) was used to analysis film structure.

7.2 Physical Characterization

7.2.1 Crystal Structure Analysis

XRD analysis showed that as substrate bias was increased, the amount of monoclinic phase increased with respect to the tetragonal phase on both silicon and soda-

lime glass substrates (Table 7.1). For silicon substrates, a deposited film had approximately 56% monoclinic phase, and as bias was increased during deposition the percent monoclinic increased to 75% and 83% for 25W and 50W bias, respectively. A no bias film had approximately 49% monoclinic and 100 W was required to achieve a

Silicon Wafer	Film Stress (MPa)	Intrinsic Stress (MPa)	Vol % Monoclinic
No Bias	-80	-255	53
10W	-100	-275	62
25W	-240	-415	75
50W	-300	-475	83
Glass Wafer			
No Bias	-177	-227	48
50W	-244	-294	70
75W	-345	-395	75
100W	-477	-527	86

Table 7.1: Reported film stress values, calculated intrinsic stress, and volume percentage of monoclinic phase for deposited YSZ thin films

monoclinic percentage of 86% on soda-lime glass (Table 7.1). Representative XRD diffraction patterns of films deposited on soda-lime wafers are displayed in Figure 7.1. These show a reduction in the T_{111} peak and an increase in the M_{111} as substrate bias was increased. XRD diffraction patterns for depositions of varying substrate bias on silicon are shown in Figure 6.2.

7.2.3 Film Stress

The internal stress is comprised of two factors: thermal (σ_{th}) and intrinsic (σ_i) components (equation shown in Eqn. 2.1) [1]. The thermal stress is due to the difference in thermal coefficients of expansion between the substrate and deposited film. The intrinsic stress is due to the accumulation of crystallographic flaws that develop during film growth [1, 5-6]. Using the coefficient of thermal expansion values shown in Table 3.1, the thermal stresses were calculated to be 175 MPa and 50 MPa for silicon and soda-

lime glass, respectively. The direction of thermal stress was tensile due to the fact that coefficient of thermal expansion values for both substrate materials are less than that for YSZ. With the measured film stress and calculated thermal stress, the intrinsic stresses for each film were calculated (Table 7.1). Data showed that higher substrate bias powers were required to achieve similar intrinsic stresses and volume percent monoclinic for the soda-lime versus silicon. This increase in bias can be attributed to the differing dielectric properties between the two substrates. This difference in bias power is specifically due to the physical setup of the deposition chamber used in this research. Silicon, being more

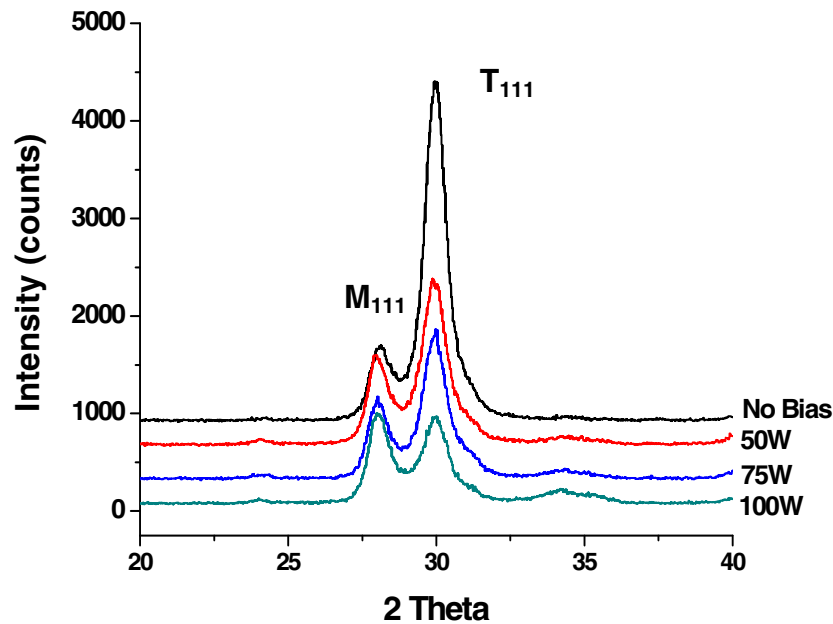


Figure 7.1: Representative XRD patterns for varying substrate bias YSZ deposited thin films on soda-lime glass wafers.

conductive than the insulating soda-lime glass wafers, does not need high substrate biasing power to produce significant ion-bombardment.

7.2.3 Film Structure

Figures 7.2-7.6 are representative SEMs of YSZ thin films deposited on soda-lime glass wafers at varying powers of substrate bias. As expected, films deposited without substrate biasing displayed a columnar grain structure (shown in Figure 7.2) [5]. However, a 100W substrate bias was needed to achieve a similar structure seen for a 50W bias film deposited on silicon. The structure appeared disrupted for the 50W and 75W bias films, but the intrinsic stresses and physical structures were similar to the 10W and 25W films deposited on silicon. It is assumed that mechanistically, the films deposited on soda-lime underwent similar growth and stress related transformations.

7.4 Summary

YSZ thin films deposited on silicon and soda-lime glass substrates showed similar intrinsic stresses and monoclinic volume fractions, but at differing substrate bias powers. The primary goal of this investigation was to produce similar YSZ film structures on soda-lime glass substrates as those reported on silicon substrates. Stress data and XRD showed that an increase in substrate bias power was needed to achieve such a film on soda-lime glass. Based on the intrinsic stress values and visual inspection of SEM micrographs, it is believed that the previously reported model of stress-induced transformation with YSZ sputtered thin films would apply to the YSZ/soda-lime glass system. This section confirms that the unique structure described previously can be reproduced on differing substrates.

Key Findings: This study showed that depending on the substrates dielectric properties, varying substrate bias powers are needed to replicate varying film structures.

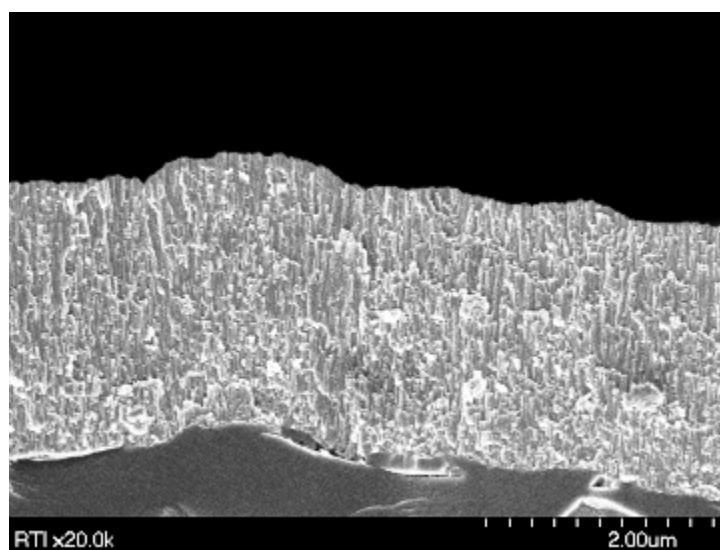
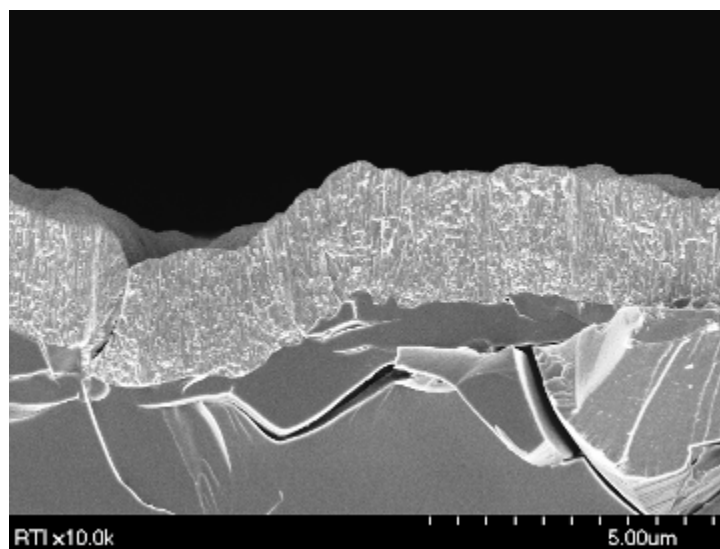


Figure 7.2: Representative SEM of film deposited without substrate bias on soda-lime glass wafer (Deposition conditions 350W, 150°C, and 30:1 Ar:O₂).

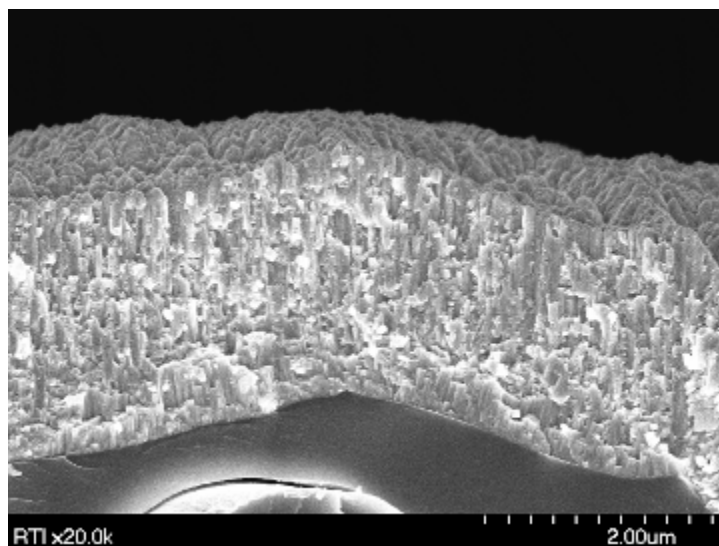
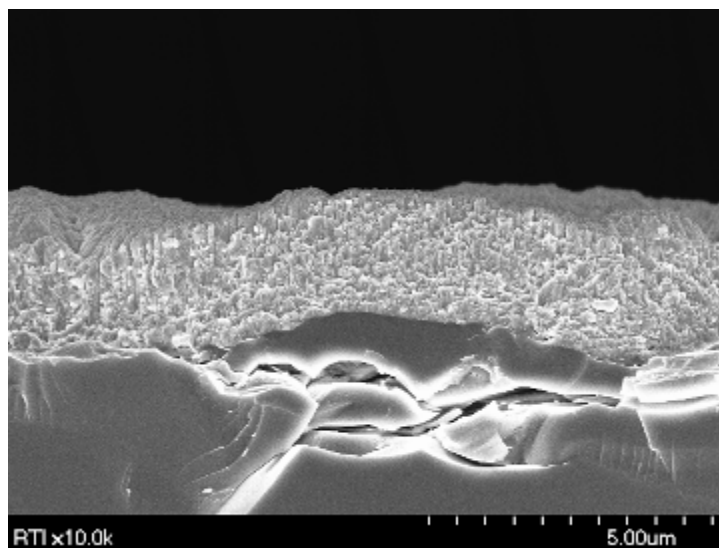


Figure 7.3: Representative SEM of 50W substrate bias film deposited on soda-lime glass wafer (Deposition conditions 350W, 150°C, and 30:1 Ar:O₂).

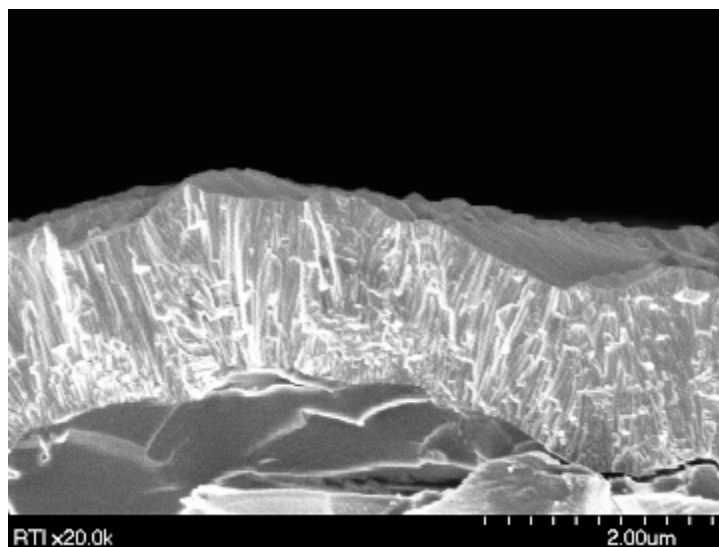
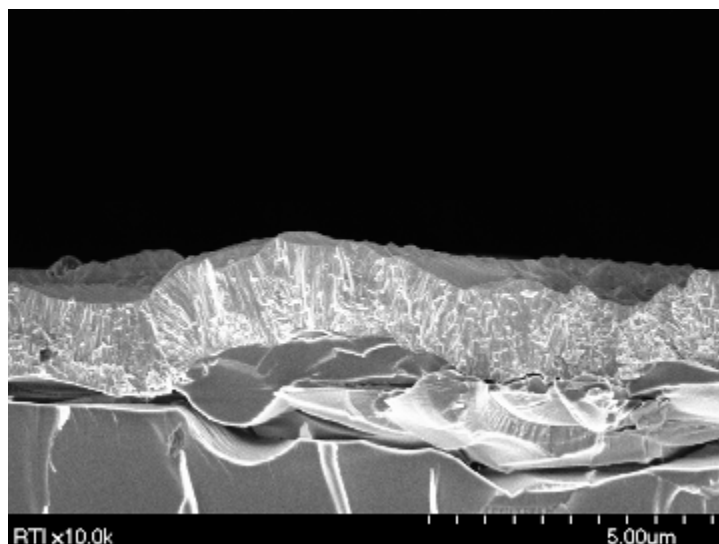


Figure 7.4: Representative SEM of 75W substrate bias film deposited on soda-lime glass wafer (Deposition conditions 350W, 150°C, and 30:1 Ar:O₂).

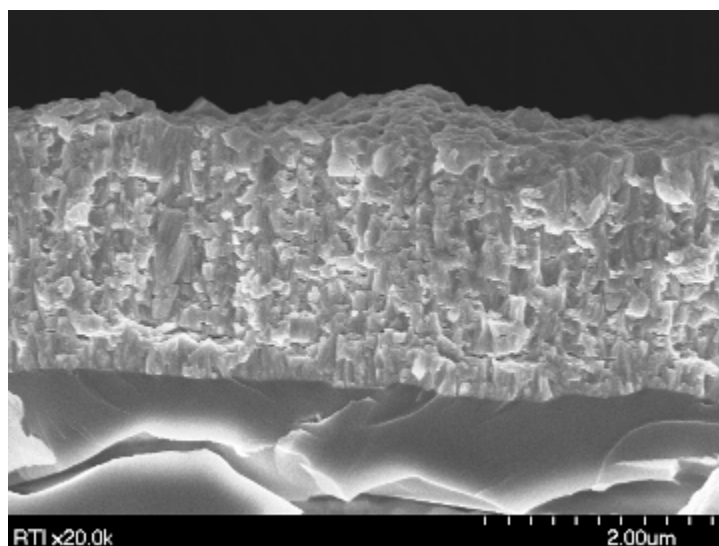
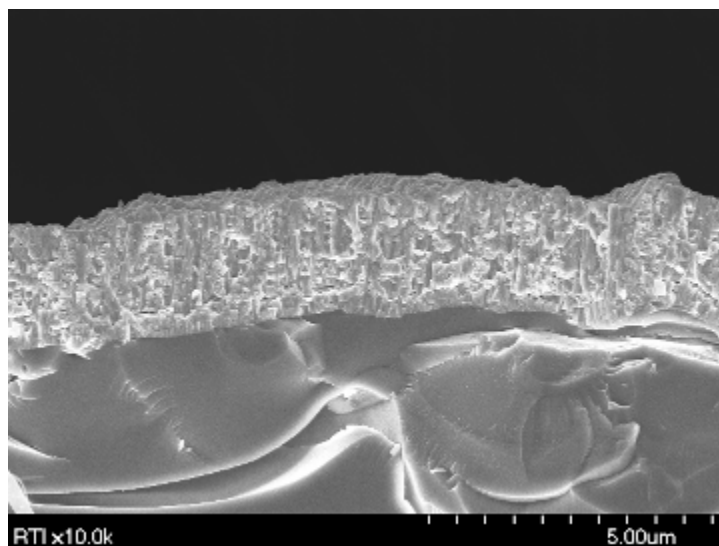


Figure 7.5: Representative SEM of 100W substrate bias film deposited on soda-lime glass wafer (Deposition conditions 350W, 150°C, and 30:1 Ar:O₂).

7.5 References

1. Ohring M., *The Materials Science of Thin Films*, (Academic Press, London, 1992).
2. Vossen J.L., “Control of film properties by rf-sputtering techniques”, *J. Vac. Sci. Technol.*, **8**(5), S12-S30 (1971).
3. Thornton J.A. and Hoffman D.W., “Stress-related effects in thin films”, *Thin Solid Films*, **171**, 5-31 (1989).
4. Green D.J, *An Introduction to the Mechanical Properties of Ceramics*, (Cambridge University Press, London, 1998).
5. Thornton J.A., “Influence of apparatus geometry and deposition conditions on the structure and topography of thick sputtered coatings”, *J. Vac. Sci. Technol.*, **11**(4), 666-670 (1974).
6. Buckel W., “Internal stress”, *J. Vac. Sci. Technol.*, **6**(4), 606-609 (1969).

Chapter 8

Conclusion

Over the course of this study, the research goals evolved into more of an investigation of specific material properties. The initial primary objective was to develop a process-structure-property relationship of sputtered-deposited yttria-stabilized zirconia thin films. The findings directed the research into areas not yet investigated for YSZ thin films. The first being a novel water vapor absorption effect on film stress. Secondly, a stress-induced phase transformation ($T \Rightarrow M$) never reported in nano-crystalline sputter-deposited YSZ thin films.

The first goal was largely accomplished. The initial depositions described in Chapter 4 showed the variation in film properties (crystal structure, film stress, and index of refraction) that were possible by varying deposition conditions. The key findings are:

- Film stress is dependent of process parameters – there is a distinct transition from tensile to compressive film stress, and this stress was shown to be tunable.
- Percentages of monoclinic to tetragonal crystal phase are dependent on process parameters (especially the induction of O_2 into the sputtering gas).
- Calculation of packing density as a function of index of refraction allows for qualitative analysis of film packing density or porosity.

- A novel relationship regarding inter-granular porosity was developed linking water vapor absorption to an increase of compressive stress within the YSZ films.

Chapter 5 describes the behavior of sputter-deposited YSZ thin films when exposed to ambient conditions. The films display modifications of film stress states in the compressive direction when exposed to this environment. This section addresses the water vapor mechanism and shows methods, which are validated with experimental data, on how to deposit a film that limits these affects. Utilizing a substrate bias, film structures can be tailored that limit water vapor absorption.

- Films deposited with substrate bias have higher compressive film stress and higher percentages of monoclinic phase.
- Lateral defects (or microcracks) are observed in bias deposited films. This coupled with intrinsic film stress is presented as a model of *in-situ* (T \Rightarrow M) phase transformation.

The film structure and stress data acquired in Chapter 5 led to the hypothesis that substrate bias deposition led to an *in-situ* stress-induced phase transformation (T \Rightarrow M). Prepped TEM samples and FFT diffractograms confirmed areas of complete and partial phase transformation in substrate bias films. This evaluation created a model of defect generation that was supported with FEA. The observed lateral defects create an interesting structure that could be useful in increasing brittle substrate fracture toughness. Applying YSZ thin films with intrinsic lateral defects may provide a useful structure for applications where the film is subjected to forces perpendicular to the growth direction

(surface). This structure could promote crack-tip shielding, better known as microcrack toughening.

FEA techniques allowed phase transformation to be modeled. As a uniform stress is applied to a columnar grain, stress fields within the grain dome upward, away from the substrate until it reaches a maximum. Once enough energy is supplied from the intrinsic stresses, transformation occurs. Due to the brittle nature of YSZ, sites of transformation create nucleation sites for microcracks (of defects).

The above study led to novel findings yet investigated in sputter-deposited YSZ thin films. The $T \Rightarrow M$ phase transformation in nano-sized grains coupled with intrinsic stress had not been reported in the scientific literature to date. This model of transformation and ability to tailor YSZ film properties, ultimately will allow better understanding of YSZ thin film material properties and mechanics.

8.1 Suggested Future Work

Comparing thin film microstructure with its bulk counterpart is widely becoming an area of interest. This study concentrated on developing basic knowledge of specific material properties of YSZ thin films by relating them to bulk YSZ. Reports have detailed a multitude of interesting material properties; such as, phase transformation, and toughening mechanisms, for YSZ ceramic, and described potential applications. As the world trends toward more of a nano-scale, it will be important to fully understand benefits that thin films with nano-scaled ultra-structure have to offer.

Being that the overall goal of research program is to strengthen brittle substrates, one question that arose from this study is whether a purely 100% tetragonal film is the

optimal coating. It is hypothesized that under applied stress, a phase transformation will offer a toughening mechanism similar to sintered, bulk YSZ. Due to water vapor concerns and possible film degradation, a unique structure was produced. This structure, with a higher fraction of monoclinic to tetragonal phase due to a phase transformation during growth, could provide an alternative solution. Lateral defects, parallel to the substrate surface and perpendicular to mechanical loading, could offer a material system that is pre-toughened and deflect a propagating crack by microcrack toughening.

Ruddell *et al.* reported that YSZ deposited films on varying substrates did not significantly improve the mechanical properties of the composite [1]. Structurally, the film had columnar grains evolving upwards from the substrate which offer no means of crack deflection. Actually this structure would promote crack propagation rather than impeding it. Teixeira *et al.* investigated the strengthening of dental porcelain as a function of YSZ thin film thickness [2]. The results showed that the strength of porcelain significantly increased with deposition of a 3 μ m YSZ coating. A non-linear relationship was observed between film thickness and strength. It was presumed that strengthening is due to modification of surface flaws and/or surface residual stress by the applied thin film. For the application of strengthening brittle substrates, the unique structures shown within this thesis should be deposited and tested. This very well might answer the question of whether phase transformation before mechanical loading could offer the best solution.

Phase transformation in YSZ has been studied extensively in bulk materials and can be reviewed in the following references [3-10]. A reported signature of T \Rightarrow M transformation is the formation of slip or twinning, which has been reported in micro-size

grain structures. This study did not concentrate on verifying twinning, but it is a topic that should be investigated more thoroughly. This would ultimately help in understanding transformation in nano-grain size materials.

Preliminary FEA modeled the generation of lateral defects with YSZ films deposited with a substrate bias. As mentioned above, this film might offer a unique structure for strengthening. Additional work is needed to fully understand multiple defects within a single grain and also throughout the entire film. Also, it may be possible to derive a model that would correlate effective toughness with defect distribution.

The culmination of this work has answered questions relating to YSZ thin films material properties, but has also offered insight into the materials science of thin film versus bulk physical and mechanical behavior.

8.2 References

1. Ruddell D.E., Stoner B.R., and Thompson J.Y., "The effect of deposition parameters on the properties of yttria-stabilized zirconia thin films", *Thin Solid Films* **445**, 14-19 (2003).
2. Teixeira E.C.N, Piascik J.R., Stoner B.R., and Thompson J.Y., "Effect of YSZ thin film coating thickness on the strength of a ceramic substrate", *J. Mat. Sci. in Med.*, *in press* (2006).
3. Hannink R.H.J., Kelly P.M., and Muddle B.C., "Transformation toughening in zirconia-containing ceramics", *J. Am. Ceram. Soc.*, **83**[3], 461-487 (2000).
4. Heuer A.H., Chaim R., and Lanteri V., "Review: Phase transformations and microstructural characterization of alloys in the system Y_2O_3 - ZrO_2 ", *Adv. in Ceram.*, **24**, 3-20 (1988).
5. Garvie R.C., "A personal history of the development of transformation toughened PSZ ceramics", *Mater. Sci. Forum*, **34-36**, 65-77 (1988).
6. Evans A.G. and Heuer A.H., "Review – Transformation toughening in ceramics: Martensitic transformations in crack-tip stress fields", *J. Am. Ceram. Soc.*, **63**[5-6], 241-248 (1980).
7. McMeeking R.M. and Evans A.G., "Mechanics of transformation-toughening in brittle materials", *J. Am. Ceram. Soc.*, **65**[5], 242-246 (1981).
8. Chen I-WEI and Reyes Morel P.E., "Implications of transformation plasticity in ZrO_2 -containing ceramics: I, shear and dilatation effects", *J. Am. Ceram. Soc.*, **69**[3], 181-189 (1986).
9. Hannink R.H.J., Kelly P.M., and Muddle B.C., "Transformation toughening in zirconia-containing ceramics", *J. Am. Ceram. Soc.*, **83**[3], 461-487 (2000).
10. Green D.J., Hannink R.H.J., and Swain M.V., *Transformation toughening of ceramics*, (CRC, Boca Raton, FL, 1989).

BIBLIOGRAPHY

- Aita C.R., Wiggins M.D., Whig R., Scanlan C.M., and Gajdardziska-Josifovska M., "Thermodynamics of tetragonal zirconia formation in a nanolaminates film", J. Appl. Phys., **79**(2), 1176-1178 (1996).
- Amor S.B., Rogier B., Baud G., Jacquet M., and Nardin M., "Characterization Of Zirconia Films Deposited By RF Magnetron Sputtering", Mater. Sci. Eng. B **57**, 28-39 (1998).
- Askland, D.R., *The Science and Engineering of Materials*, (PWS-Kent, Boston, MA, 1984).
- ASTM Joint Committee on Powder Diffraction Standards, 1974, File Nos. 37-1484.
- ASTM Joint Committee on Powder Diffraction Standards, 1974, File Nos. 17-923.
- Balzaretti N.M. and da Jornada J.A.H., "Pressure dependence of the refractive index of monoclinic and yttria-stabilized cubic zirconia", Phys. Rev B **52**, 9266-9269 (1995).
- Bendersky L.A. and Gayle F.W., "Electron diffraction using transmission electron microscopy. J. Res. Natl. Inst. Technol., **106**, 997-1012 (2001).
- Buckel W., "Internal stress", J. Vac. Sci. Technol., **6**(4), 606-609 (1969).
- Bunshah R.F., *Handbook of deposition technologies for films and coatings: science, technology, and applications*, (Noyes, NJ (1994)).
- Butler E.P., "Transformation-toughened zirconia ceramics", Mater. Sci. Technol, **1**, 417-431 (1985).
- Chen I-WEI and Reyes Morel P.E., "Implications of transformation plasticity in ZrO₂-containing ceramics: I, shear and dilatation effects", J. Am. Ceram. Soc., **69**[3], 181-189 (1986).
- Cheng Y.H., Tay B.K., Lau S.P., Shi X., and Tan H.S., "Influence of substrate bias on the microstructure and internal stress in Cu films deposited by filtered cathodic vacuum arc", J. Vac. Sci. Technol. A **19**(5), 2102-2108 (2001).
- Chopra K.L., *Thin Film Phenomena*, (McGraw-Hill, NY, 1969).
- Crookes W., "On electrical evaporation", Proc. Roy. Soc. Lond., **50**, 88-105 (1891).
- Cullity B.D., "Elements of X-Ray Diffraction". Addison-Wesley, Reading, PA (1978).

Cuomo J.J. and Gambino R.J., "Incorporation of rare gases in sputtered amorphous metal films", J. Vac. Sci. Technol. **14**(1), 152-157 (1977).

D.W. Hoffman, "Perspective on stresses in magnetron-sputtered thin films", J. Vac. Sci. Technol. A **12**, 953-961 (1994).

Diaz-Parralejo A., Caruso R., Ortiz A.L., and Guiberteau F., "Densification and porosity evaluation of ZrO₂-3mol% Y₂O₃ sol-gel thin films", Thin Solid Films **458**, 92-97 (2004).

Edington J.W., *Practical Electron Microscopy in Materials Science*, (MacMillan Philips Technical Library, Eindhoven, 1975).

Evans A.G. and Heuer A.H., "Review – Transformation toughening in ceramics: Martensitic transformations in crack-tip stress fields", J. Am. Ceram. Soc., **63**[5-6], 241-248 (1980).

French R.H., Glass S.J., Ohuchi F.S., Xu Y.N., and Ching W.Y., "Experimental and theoretical determination of the electronic structure and optical properties of three phases of ZrO₂", Phys. Rev. B **49**, 5133-5142 (1994).

Gajdardziska-Josifovska M. and Aita C.R., "The transformation structure of zirconia-alumina nanolaminates studied by high resolution electron microscopy", J. Appl. Phys., **79**(3), 1315-1319 (1996).

Gao P., Meng .L.J, dos Santos M.P., Teixeira V., and Andritschky M., "Study of ZrO₂-Y₂O₃ Films Prepared By RF Magnetron Reactive Sputtering", Thin Solid Films, **377**, 32-36 (2000).

Gao P., Meng .L.J, dos Santos M.P., Teixeira V., and Andritschky M., "Study of ZrO₂-Y₂O₃ Films Prepared By RF Magnetron Reactive Sputtering", Thin Solid Films, **377**, 32-36 (2000).

Garvie R.C. and Swain M.V., "Thermodynamics of the tetragonal to monoclinic phase transformation in constrained zirconia microcrystals", J. Mater. Sci., **20** 1193-1200 (1985).

Garvie R.C., "A personal history of the development of transformation toughened PSZ ceramics", Mater. Sci. Forum, **34-36**, 65-77 (1988).

Garvie R.C., "Thermodynamic analysis of the tetragonal to monoclinic transformation in a constrained zirconia microcrystal", J. Mater. Sci., **20** 3479-3486 (1985).

Gere J.M. and Timoshenko S.P., *Mechanics of Materials*, (PWS, Boston, MA, 1997).

Gilmer G.H., Huang H., de la Rubia T.D., Torre J.D., and Baumann F., “ Lattice Monte Carlo models of thin film deposition”, *Thin Solid Films* **365**, 189-200 (2000).

Green D.J., *An Introduction to the Mechanical Properties of Ceramics*, (Cambridge University Press, London, 1998).

Green D.J., Hannink R.H.J., and Swain M.V., *Transformation toughening of ceramics*, (CRC, Boca Raton, FL, 1989).

Grove W.R., “On the electro-chemical polarity of gases”, *Trans. Roy. Soc. Lon.*, **142**, 87-101 (1852).

Hakansson G., Sundgren J.E., McIntyre D., and Greene J., “Microstructure and physical properties of polycrystalline metastable $\text{Ti}_{0.5}\text{Al}_{0.5}\text{N}$ alloys grown by DC magnetron sputter deposition”, *Thin Solid Films* **153**, 55-65 (1987).

Hannink R.H.J., Kelly P.M., and Muddle B.C., “Transformation toughening in zirconia-containing ceramics”, *J. Am. Ceram. Soc.*, **83**[3], 461-487 (2000).

Heuer A.H., Chaim R., and Lanteri V., “Review: Phase transformations and microstructural characterization of alloys in the system $\text{Y}_2\text{O}_3\text{-ZrO}_2$ ”, *Adv. in Ceram.*, **24**, 3-20 (1988).

Hirsch E.H., “Stress in porous thin films through absorption of polar molecules”, *J. Phys D: Appl. Phys.* **13**, 2081-2094 (1980).

Hoffman D.W., “Perspective on stresses in magnetron-sputtered thin films”, *J. Vac. Sci. Technol. A* **12**, 953-961 (1994).

Hoffman R.W., “Stresses in thin films: The relevance of grain boundaries and impurities”, *Thin Solid Films*, **34**, 185-190 (1976).

Hoshida T., Nebu A., and Hayashi K., “Bending Strength of Borosilicate Glass Coated With Alumina and Silicon Carbide by RF Magnetron Sputtering”, *JSME International Journal Series , A* **41**, 332-337 (1998).

Howard C.J., Hunter B.A. and Kim D-J, “Oxygen position and bond lengths from lattice parameters in tetragonal zirconia”, *J. Am. Ceram. Soc.*, **81**[1], 241-243 (1998).

Itoh, T., *Ion Beam Assisted Film Growth*, (Elsevier, Amsterdam, 1989).

Kao A.S. and Gorman G.L., “Modification of zirconia film properties by low-energy bombardment during reactive ion-beam deposition”, *J. Appl. Phys.* **67**, 3826-3834 (1990).

Kim S.P., Choi S.K., Park Y., and Chung I., "Effect of water-absorption on the residual stress in fluorinated silicon-oxide thin films fabricated by electron-cyclotron-resonance plasma-enhance chemical-vapor deposition", *Appl. Phys. Lett.* **79** (2), 185-187 (2001).

Kisi E.H. and Howard C.J., "Crystal structure of zirconia phases and there inter-relation", *Key Eng. Mater.*, **153-154**, 1-36 (1998).

Knoll R.W. and Bradley E.R., "Correlation between the stress and microstructure in bias-sputtered $\text{ZrO}_2\text{-Y}_2\text{O}_3$ films", *Thin Solid Films*, **117**, 201-210 (1984).

Knoll R.W. and Bradley E.R., "Microstructure and phase composition of sputter-deposited zirconia-yttria films", *Mat. Res. Soc. Symp. Proc.*, **30**, 235-243 (1984).

Koch R., "The intrinsic stress of polycrystalline and epitaxial thin metal films", *J. Phys.: Condens. Mater.*, **6**, 9519-9550 (1994).

Koh Y-H, Kong Y-M, Kim S., and Kim H-E, "Improved low-temperature environmental degradation of yttria-stabilized tetragonal zirconia polycrystals by surface encapsulation", *J. Am. Ceram. Soc.* **82**, 1456-1458 (1999).

Liaw B.Y., Rocheleau R.E., and Gao Q., "Thin Film Yttria-Stabilized Tetragonal Zirconia", *Solid State Ionics* **92**, 85-89 (1996).

Ljungcrantz H., Hultman L., Sundgren J.E., Johansson S., Kristensen N., Schweitz J.A., and Shute C.J., "Residual stresses and fracture properties of magnetron sputtered Ti films on Si microelements", *J. Vac. Sci. Technol. A* **11** (3), 543-553 (1993).

McMeeking R.M. and Evans A.G., "Mechanics of transformation-toughening in brittle materials", *J. Am. Ceram. Soc.*, **65**[5], 242-246 (1981).

McKenzie D.R., Cockayne D.J. and Netterfield R.P., "Microstructure of zirconia films deposited with ion assistance", *J. Mater. Sci.* **22**, 3725-3731 (1987).

Michalski T. A. and Frieman S.W., "A molecular mechanism for stress corrosion in vitreous silica", *J. Am. Ceram. Soc.* **66** [4], 284 (1983).

Misra A. and Nastasi M., "Limits of residual stress in Cr films sputter deposited on biased substrates", *Appl. Phys. Lett.*, **75** (20), 3123-3125 (1999).

Moseley P.T, Norris J., and Williams D.E., *Techniques and Mechanisms in Gas Sensing*, (Bristol, UK, 1991).

Muddle B.C. and Hannink R.H.J., "Crystallography of the tetragonal to monoclinic transformation in Mg-partially-stabilized Zirconia", *J. Am. Ceram. Soc.*, **69**(7), 547-555 (1986).

- Muller K-H, "Stress and microstructure of sputtered-deposited thin films: Molecular dynamics investigations", *J. Appl. Phys.*, **62**(5), 1796-1799 (1987).
- Ohring M., *The Materials Science of Thin Films*, (Academic Press, London, 1992).
- Park Y., Lee J.K., Jung I., Heo S-B, and Lee J-Y, "Evolution of residual stress in plasma-enhanced chemical-vapor-deposited silicon dioxide film exposed to room air", *Appl. Phys. Lett.* **75** (24), 3811-3813 (1999).
- Petrov I., Barna P.B., Hultman L., and Greene J.E., "Microstructural evolution during film growth", *J. Vac. Sci. Technol. A*, **21**(5), S117-S128 (2003).
- Piconi C. and Maccauro G., "Zirconia as a ceramic biomaterial", *Biomaterials*, **20**, 1-25 (1999).
- Plücker J., *Annalen der Physik und Chemie*, **59**, 67-86 (1858).
- Powell R.A. and Rossnagel S.M., "*PVD for microelectronics: Sputter deposition applied to semiconductor manufacturing*", (Academic Press, CA, 1994).
- R. Fillit, P. Homerin, J. Schafer, H. Bruyas, and F. Thevenot, "Quantative XRD analysis of zirconia-toughened alumina ceramics", *J. Mat. Sci.* **22**, 3566-3570 (1987).
- Rasband, W.S., ImageJ, U. S. National Institutes of Health, Bethesda, Maryland, USA, <http://rsb.info.nih.gov/ij/>, 1997-2006.
- Rivière J.P., Harel S., Guerin P., and Straboni A., "Structure of ZrO₂ optical thin films prepared by dual beam reactive sputter deposition", *Surf. Coat. Technol.* **84**, 470-475 (1996).
- Ruddell D.E., Stoner B.R., and Thompson J.Y., "The effect of deposition parameters on the properties of yttria-stabilized zirconia thin films", *Thin Solid Films*, **445**, 14-19 (2003).
- Ruddell D.E., Thompson J.Y., and Stoner B.R., "Mechanical properties of dental ceramic coated by RF magnetron sputtering", *J. Biomed. Mater. Res.*, **51**, 316-320 (1999).
- Sankur H. and Gunning W., "Sorbed water and intrinsic stress in composite TiO₂-SiO₂ films", *J. Appl. Phys.* **66** (2), 807-812 (1989).
- Scanlan C.M., Gajdardziska-Josifovska M., and Aita C.R., "Tetragonal zirconia growth by nanolaminates formation", *Appl. Phys. Lett.*, **64**(26), 3548-3550 (1994).
- Scardi P, Lutterotti L, "Microstructural characterization of plasma-sprayed zirconia thermal barrier coatings by X-Ray-diffraction full pattern-analysis", *Surface and Coatings Technology* **61**, 52-59 (1993).

- Schofield M.A., Aita C.R., Rice P.M., and Gajdardziska-Josifovska M., "Transmission electron microscopy study of zirconia-alumina nanolaminates grown by reactive sputter deposition. Part I: zirconia nanocrystallite growth morphology", *Thin Solid Films*, **326**, 106-116 (1998).
- Smith G.E., "J.J. Thomson and the electron: 1897-1899 An Introduction", *Chem. Educ.*, **2**(6), 1-47 (1997).
- Stamper A.K., Greve D.W., and Schlesinger T.E., "Deposition of textured yttria-stabilized ZrO₂ film on oxidized silicon", *J. Appl. Phys.* **70**, 2046-2051 (1991).
- Stoney G.G., "The tension of metallic films deposited by electrolysis", *Proc. R. Soc.* **9**, 172-179 (1909).
- Teixeira E.C.N, Piascik J.R., Stoner B.R., and Thompson J.Y., "Effect of YSZ thin film coating thickness on the strength of a ceramic substrate", *J. Mat. Sci. in Med.*, *in press* (2006).
- Thamaraiselvi T.V. and Rajeswari S., "Biological evaluation of bioceramic materials-A review", *Trends Biomater. Artif. Organs*, **18**(1), 9-17 (2004).
- Thomson J.J., "A theory of the connexion between cathode and Rontgen rays" *Philosophical Magazine*, **46**, 528 (1898).
- Thornton J.A. and Hoffman R.W., "The influence of discharge current on the intrinsic stress in Mo films deposited using cylindrical and planar magnetron sputtering sources", *J. Vac. Sci. Technol. A*, **3**(3), 576-579 (1985).
- Thornton J.A. and Hoffman D.W., "Stress-related effects in thin films", *Thin Solid Films*, **171**, 5-31 (1989).
- Thornton J.A., "Influence of apparatus geometry and deposition conditions on the structure and topography of thick sputtered coatings", *J. Vac. Sci. Technol.*, **11**(4), 666-670 (1974).
- Tomaszewski H., Haemers J., De Roo N., Denul J., and De Gryse R., "Yttria-stabilized zirconia thin films grown by r.f. magnetron sputtering from an oxide target" *Thin Solid Films* **293**, 67-74 (1997).
- Tomaszewski H., Haemers J., Denul J., De Roo N., and De Gryse R., "Yttria-stabilized zirconia thin films grown by reactive r.f. magnetron sputtering", *Thin Solid Films* **287**, 104-109 (1996).

Tomaszewski H., Haemers J., Denul J., De Roo N., and De Gryse R., “ Yttria-stabilized zirconia thin films grown by reactive r.f. magnetron sputtering”, *Thin Solid Films* **287**, 104-109 (1996).

Vossen J.L., “Control of film properties by rf-sputtering techniques”, *J. Vac. Sci. Technol.*, **8**(5), S12-S30 (1971).

Wang Y.H. and Li X.P., “Phase structure characteristics of r.f. reactively sputtered zirconia thin film”, *Thin Solid Films* **250**, 132-134 (1994).

Wehner G.K. and Anderson G.S., *Handbook of Thin Film Technology*, edited by L.I. Maissel and R. Glang (McGraw-Hill, NY, 1970).

Windischmann H., “Intrinsic stress in sputtered thin films”, *J. Vac. Sci. Technol. A*, **9**(4), 2431-2436 (1991).

Wright D., *Amer. J. of Sci. & Arts*, **12**, 49-62 (1887).

Yoshimura M., “Phase stability of zirconia”, *Bull. Am. Ceram. Soc.*, **67**[12], 1950-1955 (1988).